Toward novel hybrid materials based on epitaxial graphene: Controlling the formation of defects and using them for intercalation

Amina Kimouche

UNIVERSITÉ DE GRENOBLE

THÈSE

Pour obtenir le grade de

DOCTEUR DE L'UNIVERSITÉ DE GRENOBLE

Spécialité : **Physique des Matériaux**

Arrêté ministériel : 7 août 2006

Présentée par

Amina KIMOUCHE

Thèse dirigée par **Johann CORAUX** et
codirigée par **Laurence MAGAUD**

préparée au sein du **Département Nanosciences de l'Institut Néel**
dans **l'École Doctorale « Physique» (εΔφγ)**

Vers de nouveaux matériaux hybrides à base de graphene épitaxié: contrôle de la formation de défauts et leur rôle dans l'intercalation

Thèse soutenue publiquement le **20/11/2013**
devant le jury composé de :

Dr. Francesco BONACCORSO
Chercheur à Cambridge Graphene Centre, Cambridge, Rapporteur.
Dr. Erik DUJARDIN
Directeur de recherche à CEMES, Toulouse, Rapporteur.
Dr. Fausto SIROTTI
Directeur de recherche à SOLEIL synchrotron, Examinateur.
Dr. Jérôme LAGOUTE
Chargé de recherche à MPQ, CNRS, Université Paris Diderot-Paris7, Examinateur.
Dr. Jean-Yves VEUILLEN
Directeur de recherche à l'Institut Néel/CNRS&UJF, Grenoble, Examinateur.
Dr. Laurence MAGAUD
Directrice de recherche à l'Institut Néel/CNRS&UJF, Grenoble, Examinatrice.

TOWARD NOVEL HYBRID MATERIALS BASED ON EPITAXIAL GRAPHENE: CONTROLLING THE FORMATION OF DEFECTS AND USING THEM FOR INTERCALATION

AMINA KIMOUCHE

Amina KIMOUCHE: *Toward novel hybrid materials based on epitaxial graphene: controlling the formation of defects and using them for intercalation,*
Cover image: , © 2013.

Advances in science are seldom made by individuals alone.
They result from the progress of the scientific community,
asking questions, sharing results and ideas with others.
To have rapid progress, one must encourage
scientists to interact with one another.

Douglas D. Osheroff

ACKNOWLEDGMENTS

This thesis is the result of three years of work whereby I have been accompanied and supported by many people. I am indebted to everyone who had discussed the particularities of this research with me and offered their invaluable insights into the matter.

My thesis was carried out at the Institut Néel (CNRS), in the Department Nanosciences, the team "hybrid". I want to thank Alain Fontaine and Alain Schuhl, successive directors of the Néel Institute and Joel Cibert and Hervé Courtois, directors of Nanosciences department for hosting me in their establishment, where I could enjoy a work environment quite exceptional.

I am very grateful to Erik Dujardin and Francesco Bonaccorso for accepting to be the reviewers of this thesis as well as Fausto Sirotti, Jean-Yves Veuillen and Jérôme Lagoute for their willingness to read my thesis, the valuable suggestions and for their interest in my work. Without forget the day of my defense, to find all gathered around a common adventure! Unforgettable!

It is with a feeling of profound gratitude and regards that I acknowledge the invaluable guidance, and unfailing support rendered to me by my supervisor Johann. Without the meticulous care and attention with which he supervised me and constantly gave many precious suggestions and advice when I found myself stuck in the writing of my thesis. Whenever I needed help you were there for me leading me, with your valuable knowledge. Hoping that our paths meet again in the future.

I am deeply grateful to my co-supervisor Laurence for her detailed and constructive comments, and for her important support throughout this work. Laurence, it was a great pleasure for me working next to you.

My sincere thanks go to Valérie and Philippe without whose contribution no experiments would ever have been possible, especially their valuable support during the setting-up of the UHV experiments with a great sense of humour and always willing to help.

I owe my sincere gratitude to Nicolas Rougemaille for his valuable advice and friendly help. His extensive discussions around my work and interesting explorations in operations (especially LEEM experiments) have been very helpful for this study, it was a most enjoyable visit at Elettra synchrotron with “Pizza piccola”, the memory of which I shall always cherish.

I am also thankful to Olivier Fruchart, I gained fruitful experiences by discussing with him.

I warmly thank all the lab mates for their help, support and friendship during my time in the MNM group in particular Laurent Cagnon for chemical etching of metals and Hybrid systems at low dimension with Vincent Bouchiat, Nedjma Bendiab and Laetitia marty for their creative input and valuable support during this work. I greatly enjoyed my time as a member of the group.

It was an honor for me to collaborate with such a great scientist, whose effort improved my work and understanding. For the work in this thesis, I must give special thanks to: Claude Chapelier and Charlène Tonnoir from CEA-INAC for all discussions we had and for their constant interest on my works and their contributions in chapter 5. I am also indebted to Andrea Locatelli and Onur Mentes from ELETTRA synchrotron for help during the winter of 2012 and 2013 when most of the work of Chapters 4 and 5 was completed. The work in chapter 3 couldn't have been done without the help of Clemens Winkelmann, Sayanti Samaddar and Hervé Courtois for STM/STS measurement in Nano department at Néel Institute, and Olivier Renault for XPEEM measurements at CEA-LETI.

It was a privilege to have the opportunity to work with Fausto Sirotti and Azzedine Bendounan from Sun Synchrotron who made several critical contributions. Bruno Gilles and Benjamin Delsol from SIMAP lab, kindly provided Re thin film samples.

I am indebted to my colleagues for providing a stimulating and fun environment for all the support, camaraderie, and entertainment. Vitto and Sergio, I appreciate all the help I receive from you whenever I need it in the lab, wishing you the best for the future. Thanks a lot to Hadi for helping me through the difficult times (Courage! it is your turn soon!), John for his good mood every day, Fabien, Cornelia, Dipankar, Yani and Alex, I have not forgotten who helped navigate the challenges of student life, I cherish the time we have spent together in lab. Special thanks to Zahid, Zoukaa, Chi, Mika, Geta, Sayanti, Sandrine, Louiz, Ales and Laura for their friendship and supporting each other.

I would like to express my recognition to Véronique Fauvel, Sabine Gadal, Marielle Lardato and Caroline Bartoli for all the administrative help. I'm very grateful to Valérie Reita, Sébastien Pairis, David Jeguso and Simon Le-Denmat for their technical help.

Many thanks to all people with whom I shared good times in lab, in particular Virginie, Sophie, Pierre, Jan and Benjamin.

A special thanks goes out to Fayçal and Olivier, who helped me not only to retrieve documents and articles, but also for a very enjoyable and generous environment.

This work could not have been performed without the financial support provided by EU-NMP3-SL-2010-246073 GRENADA Project.

No list would be complete without thanks to the most important people in my life and to whom I dedicate this thesis. My parents, my brothers and my sister can never be thanked enough for the unconditional love, without forget my little Feryel.

Finally, I pray to Lord to bestow me with the power to dream and ability to achieve for making this task reach to its completion.

Résumé

Le graphène épitaxié sur des substrats métalliques est un modèle prometteur pour le développement de nouveaux systèmes hybrides, dans lesquelles les effets d'interface peuvent être exploités pour concevoir de nouvelles propriétés. L'insertion d'espèces entre le graphène et son substrat, une opération connues sous le nom d'-«intercalation», est une approche très puissante à cet égard.

Avec l'aide des outils de la physique des surfaces, nous avons étudié trois systèmes
graphène/métal, dont deux sont des systèmes hybrides intercalés, et l'autre est un candidat pour un tel système : (i) le graphène/Ir(111) intercalé avec un oxyde ultra-mince, (ii) graphène/Ir(111) intercalé avec des couches sub-atomiques du cobalt et (iii) de graphène sur Re(0001). Nous avons montré que certains défauts, en particulier les ridules (délamination du graphène de son substrat) et d'autres régions courbées du graphène, jouent un rôle crucial, non anticipé, dans le processus d'intercalation. Nous avons également observé que l'intercalation se déroule d'une manière nettement différente sous ultravide et à pression atmosphérique.

Dans le premier système, des espèces contenant de l'oxygène entrent à l'extrémité ouverte des ridules et diffusent au long de ces ridules pour former des nano-rubans d'oxyde. Ces rubans modifient le dopage électronique du graphène, ce qui se traduit également par des changements substantiels dans la réponse optique inélastique (Raman) du graphène. Dans le second système, l'efficacité de l'intercalation est apparue dépendante de l'interaction
graphène-métal, laquelle varie entre les domaines de graphène orientés différemment sur_(111). Dans ce système, les sites d'entrée pour les espèces intercalées, des régions courbées dans le graphène, ont pu être identifiés grâce à l'observation in_operando (en cours de croissance) du processus. Enfin, la croissance de graphène dans un troisième système (graphène/Re(0001)), a été étudiée afin de permettre le développement de futurs systèmes
graphène/Re hybrides supraconducteurs. Dans ce système, nous avons proposé deux voies de croissance, l'une étant basé sur un processus de croissance en surface d'un monocristal massif de Re(0001), l'autre reposant sur la ségrégation en surface, activée thermiquement, du carbone dissout à haute température dans des films minces de Re sur saphir.

Abstract

Epitaxial graphene grown on metal substrates is a promising platform for developing new hybrid systems, in which interface effects can be exploited to engineer novel properties. The insertion of foreign species between graphene and its substrate, referred to as “intercalation”, was shown very powerful in this respect.

With the help of surface science tools, we have studied three graphene/metal systems, two of which are intercalated hybrid systems, and the other is a candidate for such a system: (i) graphene/Ir(111) intercalated with an ultrathin oxide, (ii) graphene/Ir(111) intercalated with cobalt (sub) atomic layers, and (iii) graphene on Re(0001). We found that some defects, especially wrinkles (linear delamination of graphene from its substrate) and other curve graphene regions play a crucial, yet unanticipated role in the intercalation process. We also found that the intercalation proceeds in a markedly different fashion under ultra-high vacuum and under atmospheric pressure.

In the first system, oxygen-containing species were found to intercalate via the open end of wrinkles; to diffuse along then, and to form oxide nanoribbons along wrinkles accordingly. These ribbons modify the charge density of graphene, which also translates into substantial changes in the inelastic (Raman) optical response of graphene. In the second system, the efficiency of intercalation proved to be dependent on the graphene-metal interaction, which varies between differently oriented graphene domains on Ir(111). In this system, the entry sites for intercalated species could be identified, thanks to in operand observation of the process, as curved regions in graphene. Finally, graphene growth in a third system, graphene on Re(0001), was addressed in order to enable the future development of graphene/Re superconducting hybrids. In this system, we proposed two growth routes, one being a surface-confined process, on bulk single-crystal Re(0001), and the other being a temperature-induced segregation of carbon dissolved at high temperature in thin Re(0001) films on sapphire.

Amina KIMOUCHE: *Toward novel hybrid materials based on epitaxial graphene: controlling the formation of defects and using them for intercalation,*
Cover image: , © 2013.

CONTENTS

INTRODUCTION

0.1 GRAPHENE AS A BUILDING BLOCK IN HYBRID SYSTEMS

Owing to the various possible hybridizations of its outer atomic orbitals, carbon, one of the most common elements, plays a unique role in nature. It forms many allotropes. This material keeps on surprising scientists with its rich physics and possible myriad applications. Being a truly two-dimensional arrangement of carbon atoms, disposed in a honey-comb lattice, graphene fostered considerable interest in various scientific communities, from physics, to chemistry, materials science and biology.

Numerous studies of graphene have been stimulated by its exceptional properties, to name only a few, the high current density it can sustain, its unprecedented thermal conductivity, its quantized optical transmittance and the linear dispersion of the electronic bands which governs electronic transport through it. Many applications have been envisaged for graphene, which has been proposed as a candidate for transparent conductive electrodes [1], field effect transistors [2], nano-electromechanical systems [3] or anodes in Li-ion batteries [4].

In parallel to the exploration of the unique properties of isolated graphene, the development of more advanced architectures, called graphene-based hybrid systems, combining graphene with other materials, has stimulated intense efforts recently. The motivation is to combine multiple functionalities and, in some cases, to achieve new ones. Interfaces play a prominent role in these hybrid systems. A relevant approach, on the way to the detailed understanding of this role, is the study of systems with well-defined interfaces, such as in high quality graphene in contact with high quality metallic surfaces. A number of transition metals with interesting properties (e.g. magnetism, superconductivity) may serve as both supports and catalysts for the growth of graphene. They offer an opportunity for preparing functional graphene/metal systems, in which the graphene has a well-defined epitaxial relationship with its substrate, and which are referred to as epitaxial graphene [5].

A large variety of graphene-based hybrid systems can be achieved from epitaxial graphene systems. Materials can be either deposited on top of graphene, as was shown for metallic nanoclusters [6] or semiconducting nanowires [7], or intercalated in between graphene and its substrate [8]. Such approaches were found powerful, for modifying the properties of graphene, e.g. inducing a bandgap [9], magnetic moments [10], or a Rashba effect [11] in graphene, or modifying those of the materials contacted to graphene, e.g. the magnetic properties of small size clusters [12] and of ultrathin films [13].

0.2 INTERCALATION PATHWAYS FOR TUNING THE GRAPHENE PROPERTIES

The guideline for our work is the development of novel graphene-metal hybrid systems with the help of intercalation strategies and the study of their properties. The first step in this route is the growth of graphene on its metallic substrate. While on some metals, such as iridium, growth of graphene is well-established and relatively straightforward,

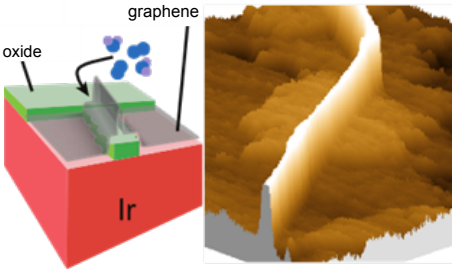

Figure 1: Cartoon showing oxygen species entering the wrinkles with a selective oxidation of iridium substrate. Three-dimensional atomic force microscopy image of an oxide ribbon formed around a wrinkle.

on some others, like rhenium as we will see, it is a complex processes which is not yet fully understood. Since the choice of the metal used as a support for graphene is not only governed by its convenience with respect to growth, but also with respect to the new functions it may give to graphene, there is strong motivation for achieving further understanding in the growth of graphene on metals.

The second step in the preparation of intercalated graphene-based hybrid systems is actually the intercalation process itself. Though a large amount of works have been devoted to intercalation in graphene systems, surprisingly, there is only partial knowledge about how intercalation actually works. The intercalation pathways are largely unknown, which is obviously disappointing, as one expects better-controlled and more advanced structures to become within reach once these pathways will be known.

Finally, the third step is the study of the new properties deriving from the intercalation.

As we will see in this thesis through the study of three different systems, we could not systematically reach the second and third steps, and once the third step was actually undertook, it appeared obvious that multiple characterization bringing complementary information were required in order to understand the observations.

0.3 DESCRIPTION OF THE MANUSCRIPT

We will first address a system in which graphene growth is well-established, graphene on Ir(111) [14, 15], and focus on the intercalation of oxygen species between graphene and Ir(111), and on the effects this intercalation has on the properties of graphene. We will show that in this prototypical example of a weak graphene-metal interaction system, a well-know defects of graphene sheets, wrinkles, play a key role in the intercalation: oxygen species enter at wrinkles easily and diffuse below graphene (Figure 1). Spontaneous intercalation is indeed found in atmospheric conditions to yield oxide nanoribbons intercalated along between graphene and Ir(111). These ribbons are found to modify the charge density in graphene.

We will continue with the same system, graphene on Ir(111), but studied in ultra-high vacuum, in the view of the intercalation of cobalt. Cobalt is chosen here as it has been found in our group that novel graphene-cobalt hybrid systems can be prepared by intercalation, in which the magnetization of Co ultrathin films can be controlled by the graphene-cobalt interface. We will show that the intercalation depends on the epitaxial relationship between graphene and Ir(111), and that preferential nucleation occurs at curved graphene regions, on the walls of the wrinkles and on top of substrate step edges (Figure 2).

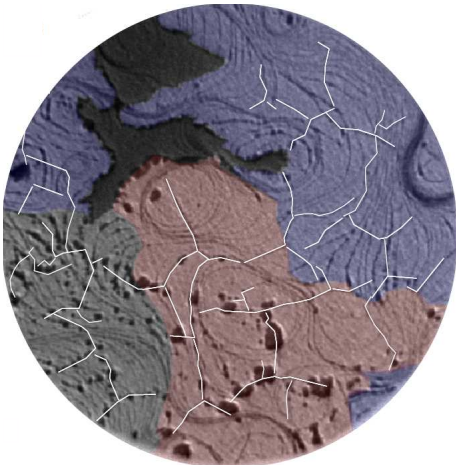

Figure 2: Low-energy electron microscopy (15 µm field of view) image of different rotational domains of graphene flake have been coloured for clarity. Wrinkles are highlighted by white lines.

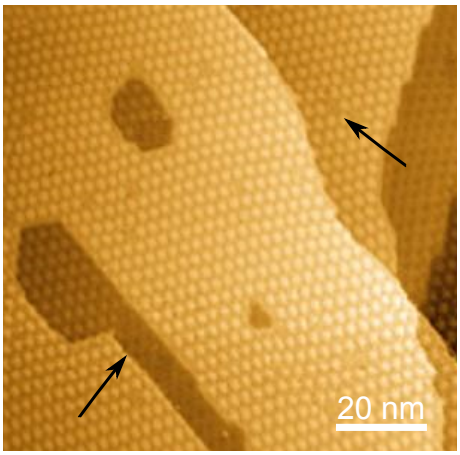

Figure 3: Scanning tunnelling microscopy of graphene/Re showing the moiré pattern due to the lattice mismatch of graphene and Re, and with various of defects indicated by black arrows.

We will finally address a third systems, which unlike graphene/Ir(111), is characterized by a strong interaction between graphene and its substrate: graphene/Re(0001) (Figure 3). While the strong graphene-Re coupling is desirable in order to achieve transparent graphene-metal contacts, a prerequisite for proximity-induced superconductivity in graphene (graphene, alone, is not superconducting, but rhenium is), it is a priori detrimental to the unique electronic properties of graphene, which should be destroyed. Therefore we foresee that local intercalation between graphene and Re will be a way to reconcile efficient induction of superconductivity in graphene and preservation of the unique properties of graphene. The complexity of the growth of graphene on Re(0001), however, focused most of our attention thus far, and for this reason we will only address this aspect in the present manuscript. We will unveil to distinctive growth mechanism for graphene on Re(0001), a surface-confined one onto bulk single-crystals, and one based on the temperature induced surface segregation of carbon enriched in thin Re thin films. We will also describe the results of first principle calculations and Raman spectroscopy showing that the interaction between graphene and Re(0001) is, as expected, strong.

The manuscript is organized as follows. Chapter one is an overview of graphene oriented towards epitaxial graphene on metals. In this chapter basic properties of graphene, its structure (superstructures, defects), growth, and properties when deposited on metals will be shortly reviewed.

Chapter 2 gives details on the experimental methods which we have employed. *In situ* characterization techniques, electron microscopy-diffraction and scanning tunnelling microscopy, as well as *ex situ* ones. Raman spectroscopy and atomic force microscopy will be described. Details on the measurement setup used in this work will also be presented. I also will describe the preparation of samples which we will address in the next chapters, thin rhenium films on sapphire, and graphene on thin iridium films on sapphire.

The next three chapters will be devoted to the three systems described above: graphene on Ir(111) intercalated at ambient pressure with oxide ribbons (chapter 3), graphene on Ir(111) intercalated by cobalt (chapter 4), and graphene on Re(0001) (chapter 5).

0.4 QUESTIONS ADDRESSED IN THIS MANUSCRIPT

The study of the three systems mentioned above raises a number of questions, some of which are common to the three systems, some not, which I summarize here:

- Where does intercalation start in epitaxial graphene systems? What is the role of defects? Are there some different processes depending on pressure? Is intercalation localized, or is it extended?

- What is the influence of the graphene-metal interaction? What is the importance of the graphene-metal epitaxial relationship? Can intercalation differ from on graphene-metal system to the other?

- How does graphene grow on metals? How do surface carbide, dissolution in bulk, and graphene growth compete depending on temperature?

1

EPITAXIAL GRAPHENE ON METALS

Carbon exhibits a variety of interesting structural and electronic properties because of its tendency to form both sp^2 and sp^3 bonds [16]. This gives rise to a range of interesting physical properties. The term, graphene, was first coined to describe a single sheet of carbon by Boehm in 1964 [17] . This two-dimensional (2D) counterpart of graphite had been obtained decades ago by growth on substrate, but it is only from 2004, with the progress of nanofabrication, that its unique electronic properties became accessible to experimentalists. Graphene can be seen a basic building block for graphitic materials of all dimensionalities. It can be wrapped up to form a zero-dimensional object, a fullerene, or a one-dimensional one, a nanotube, or stacked into a three-dimensional object, graphite [18] as shown in Figure 4. The infatuation for graphene owes a lot to the surprising finding from 2010 Physics Nobel Prize winners A. Geim and K. Novoselov, that graphene can be isolated onto a dielectric support, SiO_2, by simple repeated peeling off of graphite crystallites with the help of adhesive tape [19], a method known since then as the "scotch tape method".

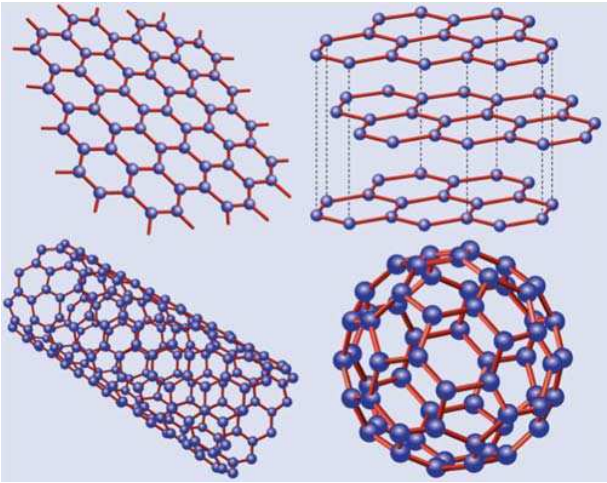

Figure 4: Representation of the atomic structure of carbon allotropes, issued from [20].

Thanks to its unconventional properties, since 2004 graphene has become a material of an intense interest [19]. Especially, graphene became the first material hosting exclusively charge carriers at the Fermi level which behave like relativistic particles utterly coupled to their antiparticle (electron or hole) [21, 22]. As those carriers are those relevant for electronic transport in devices, these opened broad perspectives for both fundamental Physics exploring quantum phenomena usually restricted to high energy physics, and potential applications with new functionalities and/or improved performances in microelectronics. In this chapter, I will introduce various concepts which will be employed to understand the properties of graphene grown in epitaxy on a metal, hereafter referred to as epitaxial graphene. Here I note that the term "epitaxy" is employed in its broad meaning. It may refer to a mere prolongation of the atomic

rows from the substrate by carbon atoms through covalent bonds, but also to situations in which only a well-defined or preferential orientation of graphene's zigzag rows with the substrate atomic rows occur. In this sense this includes the notion of van der Waals epitaxy [23], which describes the situation in which the epitaxial relationship is guided by van der Waals bonding. First, I will present the structure of graphene on metals including the defects. Then, I will focus on the growth of graphene, specially emphasising on the parameters that influence the metal-graphene interaction during growth. Special attention will be paid to the electronic properties of graphene on different metals in connection with their interaction with graphene.

1.1 STRUCTURE AND ELECTRONIC PROPERTIES OF FREE-STANDING GRAPHENE

1.1.1 *Structure in real and reciprocal spaces*

Graphene is a planar sheet of carbon atoms arranged in a honeycomb lattice with a strong covalent σ bonds between the carbon atoms. The graphene lattice consists in two identical triangular sublattices which are shifted on with respect to another by a_c= 1.42 Å(the C-C bond length in graphene) along one median of a triangle in one sublattice, [24] as shown in Figure 5. The lattice vectors are defined as follow:

$$a_1 = \frac{a}{2}(3, \sqrt{3}) \qquad a_2 = \frac{a}{2}(3, -\sqrt{3}) \tag{1}$$

The high degree of structural symmetry gives rise to two inequivalent points, K and K′ at the corners of the Brillouin zone. Their coordinates in reciprocal space are:

$$K = \left(\frac{2\pi}{3a}, \frac{2\pi}{3\sqrt{3}a}\right) \qquad K' = \left(\frac{2\pi}{3a}, -\frac{2\pi}{3\sqrt{3}a}\right) \tag{2}$$

Further, the reciprocal lattice vectors are given by:

$$b_1 = \frac{2\pi}{3a}(1, \sqrt{3}) \qquad b_2 = \frac{2\pi}{3a}(1, -\sqrt{3}) \tag{3}$$

These vectors determine the first Brillouin zone (FBZ) Figure 5, in which the symmetry point Γ can be defined as the centre and K and $K^{'}$ for the two groups of three equivalent points at the six corners of the hexagonal Brillouin zone. These two high symmetry points K and $K^{'}$, which are called Dirac points, have particular importance as detailed in the following section.

1.1.2 *Band structure*

In graphene, sp^2 hybridised orbitals are formed, they give a strong σ bonds that ensure the cohesion of the honeycomb lattice [25], while the other $2p_z$ orbital, which is perpendicular to the graphene plane, forms π covalent bonds. Those electrons involved in π bonds give to graphene most of its remarkable electronic properties. The band structure of graphene was first studied by Wallace who used tight binding model

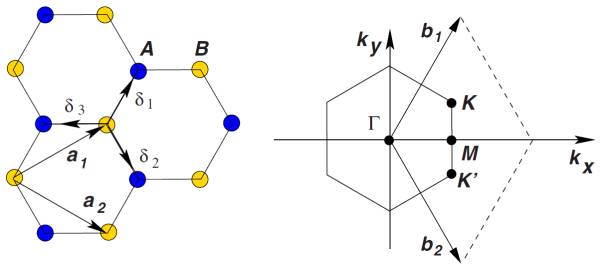

Figure 5: Geometry of graphene in real and reciprocal space. (a) Hexagonal honeycomb lattice in real space, the vectors $\vec{a_1}$ and $\vec{a_2}$ and the atoms A and B define the Bravais network (b) Corresponding Brillouin zone where Γ is the centre of the FBZ and K and K′ its corners; M is located on a side of the FBZ between K and K′ point [20]

[26], he considered electron hopping from p_z orbitals between nearest and next-nearest neighbours while neglecting the overlap of electron wave-functions centred on different atoms. This method was reproduced later by references [27, 28, 29]. The tight binding Hamiltonian used to derive the band structure of graphene writes, in this model:

$$H = -t \sum_{<i,j>,\sigma} \left(a^*_{\sigma,i} b_{\sigma,j} + c.c\right) - t' \sum_{<<i,j>>,\sigma} \left(a^*_{\sigma,i} a_{\sigma,j} + b^*_{\sigma,i} b_{\sigma,j} + c.c\right) \tag{4}$$

where the $\sum_{\langle i,j\rangle}$ runs over the different i,j atomic sites of the lattice, t and t′ are the nearest (between sublattices A and B) and next-nearest (within the same sublattice) hopping energies (t = 2.8 eV from density functional theory calculations and t′ is about 0.1 eV), a (b) and a* (b*) are the creation and annihilation operators for electrons living on sublattice A (B), and σ is the spin of electrons [20]. The electronic dispersion (energy vs wavevector length $k = \left|\overrightarrow{k}\right|$, $k = (k_x, k_y, k_z)$) of the π bands which is derived from this model can be written:

$$E_{\pm} = \pm t\sqrt{3 + f(k)} - t' f(k) \tag{5}$$

Where

$$f(k) = 2\cos(\sqrt{3} k_y a) + 4\cos\left(\frac{\sqrt{3}}{2} k_y a\right)\cos\left(\frac{3}{2} k_x a\right) \tag{6}$$

This yields two electronic bands, the valence π and the conduction π* bands, which meet only at the six corners of the FBZ. Given the number of electrons per carbon atoms, the valence band is filled while the conduction band is empty, i.e. the Fermi level lies exactly at the intersection of the two bands. Noteworthy, in a very good approximation in an energy window of ± 2 eV about Fermi level, the electronic bands have linear dispersion, forming six cones at K and K′ points. The electronic dispersion is usually written in the form:

$$E(\overrightarrow{k}) = \pm \hbar v_f \mid \overrightarrow{k} \mid \tag{7}$$

Here, $v_f = \frac{3\,t\,a}{\hbar} \sim 10^6\,\mathrm{m.s^{-1}}$ is the Fermi velocity. This linear dispersion implies that whatever their energy, charge carriers have the same velocity, i.e. they behave like massless particles. For this reason they are usually referred to as relativistic particles, whose velocity is v_F, which is about 300 times smaller than the speed of light. This property, though often highlighted, does not account for many of the unique behaviours of charge carriers in graphene. The Hamiltonian written above may be rewritten in an expression involving Pauli matrices, which introduce a new quantum number for describing electronic states, the sublattice pseudo-spin, which is independent of the spin of the electrons. An up pseudo-spin refers to the component on one sublattice and a down pseudo-spin refers to the component on the other sublattice. Considering charge carriers in graphene as massless pseudoparticles having a pseudospin allows one to make a formal analogy with massless chiral Dirac fermions, which are better described by the Dirac-Weil equation than by the Schrödinger one. This analogy can be used to understand the unusual sequence of Landau levels, corresponding to a discretization of the density of states of a 2D electron gas in the presence of a perpendicular magnetic field (integer quantum Hall effect), which was unveiled in 2005 [22]. Not only the spacing between Landau levels is markedly different from that of a 2D electron gas for which electrons live in parabolic electronic bands, but also the presence of a Landau level at the Fermi level is unique and can be traced back to the presence of two pseudo-spins. The unique behaviour of charge carriers in graphene gives access to a wealth of phenomena usually explored in high energy physics, such as Klein tunnelling, the total transparency of a potential barrier, whatever its height, to massless chiral Dirac fermions impinging it perpendicularly [21].

Graphene has initiated the study of the properties of purely 2D materials, which extends since a few years to other systems, e.g. hexagonal boron nitride or transition metal dichalcogenides like MoS_2 or WS_2. BN was found to be a close-to-ideal smooth support for graphene sheets [30], while MoS_2 and WS_2 showed unique optical properties which strongly vary with the number of layers [31].

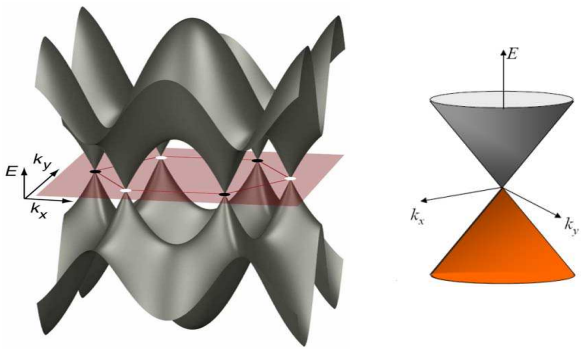

Figure 6: Electronic dispersion of graphene throughout the Brillouin zone, the zoom depicts the structure on Dirac cone near the Fermi level, issued from [32].

1.2 STRUCTURE OF EPITAXIAL GRAPHENE ON METALS

The ideal structure described in the previous section is considerably simpler than in any practical situation. Even suspended, graphene is a rippled membrane rather than a

flat one. Onto its most commonly used support, SiO_2, it is also rippled, due to the only local contact with it. In the case of graphene resting on its growth substrate, e.g. silicon carbide or a metal, the structure is better defined, but can be rather complex, mostly as a result of a complex trade-off between strain, rippling, and bonding energies.

1.2.1 *Epitaxy between graphene and metals*

The carbon-carbon bond in graphene is smaller than the metal-metal ones at all transition metal surfaces, by at least about 1% (graphene and Ni(111)). Given that graphene has huge Young's modulus, related to the strength of the C-C bond, the compression of the graphene lattice which would give a pseudomorphic graphene onto the metal surface is most often prohibitively costly. Only for low lattice mismatches can graphene conform to its metallic substrate, as it is the case on Ni(111) and Co(0001). On these metals, density functional theory (DFT) suggests that the most stable configuration corresponds to one C sublattice sitting directly on top of Ni/Co atoms [33, 34], and the second sublattice on top of the Ni/Co atoms in the third layer. A difference of height between the two sublattices, resulting from this configuration which breaks the equivalence of the two-sublattices, was predicted. Experiments seem in qualitative agreement with these predictions [35].

On all other metals graphene does only partly accommodate its lattice. The mismatch between the metal and graphene atomic lattices yields a periodic pattern of local partial coincidences between the two lattices. The formation of such a pattern is similar to a well-known optical phenomenon, the moiré effect. It may be regarded as an interference between two mismatched lattices. Interestingly, other kinds of moirés were observed long ago in another sp^2 hybridized carbon system, graphite: these moirés do not result from a lattice mismatch, but rather from an orientation mismatch between two identical lattices (two stacked and rotated graphene sheets) [36].

The moiré patterns between graphene and metals may have different symmetries depending on the symmetry of the metal surface: triangular and linear moirés are formed on fcc(111) [37] or hcp(0001) [38], and bcc(110) [39] metal surfaces respectively.

In the case of hcp(0001) and fcc(111) metal surfaces, if the carbon zigzag rows align along the dense packed metal rows, the period of the moiré $d_{moiré}$ is given by:

$$d_{moiré} = \frac{1}{\frac{1}{a_C} - \frac{1}{a_m}} \tag{8}$$

with a_C and a_m the graphene and metal surface lattice parameters respectively. This value decreases as the angle between carbon zigzag rows and metal dense packed rows increases from 0 to 60° [40]. For graphene/Ir(111) [40], the moiré period is typically 2.5 nm, while it is about 6.6 nm for graphene/Cu(111) [41].

The local environment of carbon atoms, the carbon-metal interaction, vary as a function of the position in a moiré unit cell. As a result moirés are associated with a rippling of graphene, which can reach as much as about 2 Å, if the graphene/metal interaction strongly varies (case of graphene/Ru(0001) [42]), or be much smaller, for instance 0.5 Åfor graphene/Ir(111) [43].

1.2.2 *Defects in epitaxial graphene on a metal*

The achievement of large scale graphene in reproducible way with controlled quality remains a challenge for potential applications. Different defects appear during epitaxial growth on metals and their relevance has been taken into account for tuning the graphene's physical properties Figure 7 [44, 45, 46, 47]. These defects are of different kinds: topological defects such as vacancies [48, 49, 50, 51], heptagon-pentagon pairs [52], and extrinsic ones, e.g. the local bending of graphene at step edges or local linear delaminations of graphene from its substrate, so call-wrinkles.

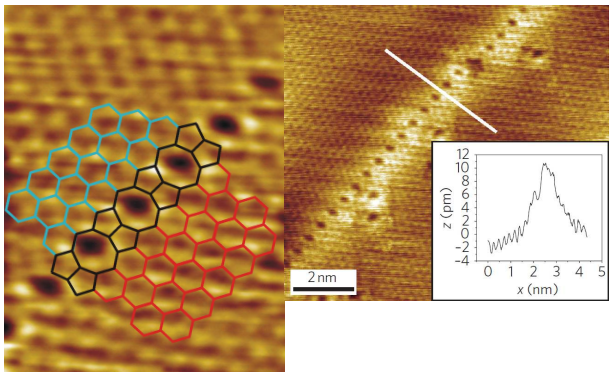

Figure 7: Left scanning tunnelling microscopy image: defect structure and superimposed defect model. Right image: line defect with image profile in the direction perpendicular to the wire (inset). The brighter area surrounding the defect originates from the states with wave functions localized at the defect [46].

The crystallographic orientation between graphene and a metal is best defined at high temperature. However, even using high temperature growth, graphene might develop domains with distinct (well-defined) epitaxial relationships. Overall, small- (Figure 8 [14]) and large-angle [53] twinned domains are often encountered in graphene samples, to a larger extent in case of metals with which graphene weakly interacts. At the boundary between twinned domains, edge dislocations, which are heptagon-pentagon pairs in graphene, are found with a density increasing with the misorientation angle between the domains [14].

Another kind of intrinsic defects which are formed in graphene during growth are carbon vacancies of various sizes [54], which can be trapped at the edge of the growing graphene islands. The density of these defects decreases with growth temperature. This is first due to an increased edge mobility, promoting recombination and annihilation of defects. This is also due to their increased mobility inside the graphene lattice, which governs their migration towards the graphene islands where again they might recombine with others and possibly annihilate.

A very common kind of extrinsic defect observed in graphene on metals (and SiC) after its preparation is local delamination, in the form of a pattern of extended lines, of graphene from the substrate. This defect is usually referred to as a wrinkle. It forms due to the mismatch in thermal expansion coefficient between graphene and its substrate [55] in systems for which the graphene-substrate interaction is sufficiently weak that the epitaxial stress, exerted on graphene by the substrate during cool down following growth, can be relieved by delaminating and bending graphene. Wrinkles

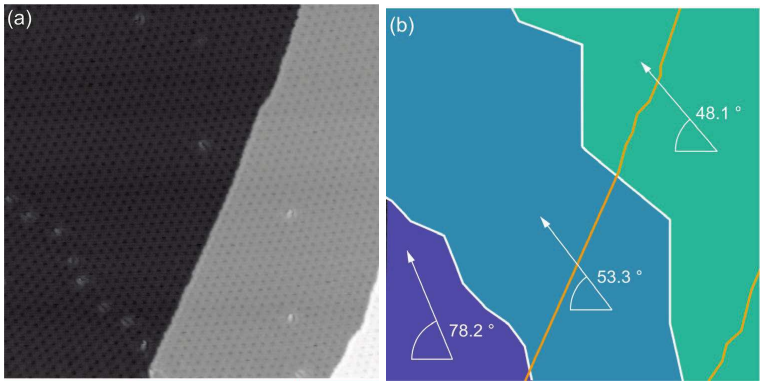

Figure 8: STM topograph (108×108 nm^2) showing three domains with a different orientation of graphene on Ir(111) [14].

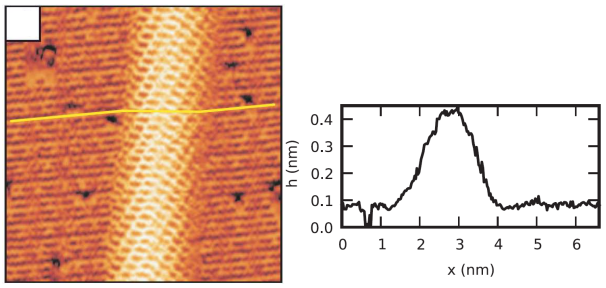

Figure 9: STM topograph (7 × 7 nm^2) of a wrinkle of low height in graphene on Pt(111) in atomic resolution. The bright line corresponds to the profile shown on right, from [57].

are found for instance in graphene on Ir(111), Pt(111), Cu, but not in graphene on Ru(0001) or Ni(111). The distance between wrinkles is usually of the order of a micron, their width and hight in the range of a few 1 nm to a few 10 nm Figure 9. Avoiding the formation of this defects, which was found to influence electronic transport [56], is highly desirable but could not be demonstrated yet.

1.3 GROWTH ON METALS

Currently, several alternatives are being intensively studied with the main aim of achieving a method of producing high-quality graphene films with controllable thickness in order to allow its implementation in future devices.

The choice of the growth method is usually governed by the kind of device envisaged. The "scotch tape" method is acknowledged as the best suited for the preparation of very high quality devices for use in the optical and electronic investigation of the fundamental properties of graphene. Chemical routes (oxidation of graphite followed by reduction of graphene oxide) [58] are on the contrary suited for low-cost and high-yield production of defected graphene, which is well adapted for the build up of hybrid graphene-based architectures (combining, e.g. graphene with nanoparticles or chemical compounds), for instance in the view of energy storage [59]. Growth on substrates has potential for the production of high quality and large area graphene. Using silicon carbide as a substrate [60] yields graphene directly onto a dielectric substrate, i.e. in principle which can serve as a back-gate electrode for microelectronics applications. Noteworthy however, the cost of insulating SiC wafers and the temperatures needed for high quality graphene preparation remain a serious hurdle to the develop-

ment of a graphene/SiC technology. Another route to graphene preparation is growth onto a metallic substrates using the thermally activated catalytic decomposition of carbon species onto the metal. Considerable amount of work has been devoted to this route. First in surface science, studies have been performed under ultra-high vacuum (UHV) using single-crystal metal surfaces, in the view of understanding elementary growth processes and preparing ultra-high quality graphene. Second towards the development of cost effective processes, much closer to atmospheric pressure, and using low-cost (polycrystalline) [61, 62, 63]. Graphene preparation on metals, when aimed at applications, for instance for electronics, is usually followed by a process allowing to transfer graphene onto an arbitrary (usually dielectric) support [61, 62].

The temperature for growth of graphene on metals is usually chosen sufficiently high to obtain significant catalytic activity from the metal and high carbon adatom mobility at the surface, which is a prerequisite for the formation of high quality graphene. At such a temperature, typically close to 1000°C, the carbon can either remain on the surface of the metal in case of a low carbon solubility metals like Ir, Cu, Pt and Au (Figure 10), or dissolve inside the metal bulk in high carbon solubility metals like Ru, Co, Ni (Figure 10), or even form carbide (inside the bulk or on the surface). In the following we will describe these three cases, which lead to different growth mechanisms, chemical vapour deposition (CVD), surface segregation, and transformation of a carbide to graphene, respectively.

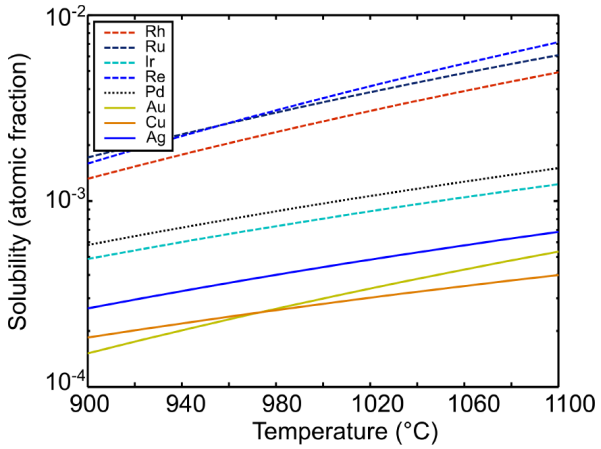

Figure 10: C solubility on different metals, issued from [64]

1.3.1 *Chemical vapour deposition*

Chemical vapour deposition consists in the surface reaction of molecules, leading to the growth of thin films. In the CVD of graphene, hydrocarbons are usually employed as a carbon precursor. Their catalytic decomposition onto the metallic surface consists in a de-hydrogenation leading to the formation of a 2D gas of carbon adatoms, which form 2D clusters with a honeycomb network, eventually resulting in the formation of graphene. The hydrocarbons employed thus far do not stick onto graphene at growth temperatures, and are only decomposed onto the graphene-free surface. In practice, this effect self-limits the growth to a single layer of graphene (see below), which is

one main interest for this technique. CVD of graphene on metals has been used since decades, with first reports dating back to 1960's [65], but it is only during the 2000's that the growth became understood.

Graphene nucleation at step edges

Experimental observations [66, 67, 54] and theoretical studies [68, 69, 70, 71] show that the nucleation of graphene is preferred near step edges of the metallic substrate at low C concentration, while at high C concentration, the nucleation tends to occurs both on a terrace or near step edge [66].

The density of graphene islands depends on the temperature, as a direct consequence of the increased carbon mobility at higher temperature. The nucleation starts at the lower terrace of the metal step edge, as it was shown on Ir(111) [54]. Growth then proceeds on the same terrace and after some delay on the upper terrace Figure 11. The nucleation on the lower terrace is accompanied by a profound reshaping of the metal step Figure 12, presumably promoted by the maximization of the number of C-metal bonds. The detachment of the graphene edge from the metal step edge, which is needed for prolonging the graphene lattice upon growth uphill the step edge, is thought to require overcoming a substantial barrier energy, which should explained the delayed growth on the upper terrace.

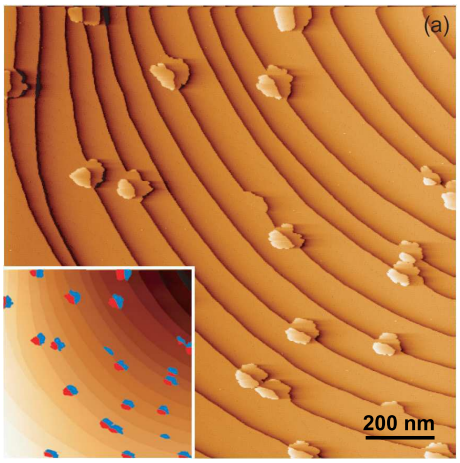

Figure 11: STM topograph of graphene islands nucleated at Ir(111) atomic step edges, grown at 1120 K with 3.10^{-6} mbar. Insert: graphene on lower (upper) terrace is marked blue (red) highlighting the regions of the surface which are covered with graphene [54].

From nanoislands to full coverage

The observation of an unchanged density and area of graphene islands as a function of substrate step edge density revealed that the carbon adatom concentration during growth between 850 and 1200 °C is rather uniform across the sample surface. This uniform concentration is the evidence for the efficient long range (microns at least) mobility of carbon atoms. All graphene islands actually grow with the same rate. In a study of the graphene coverage on Ir(111) as a function of the ethylene dose, it was

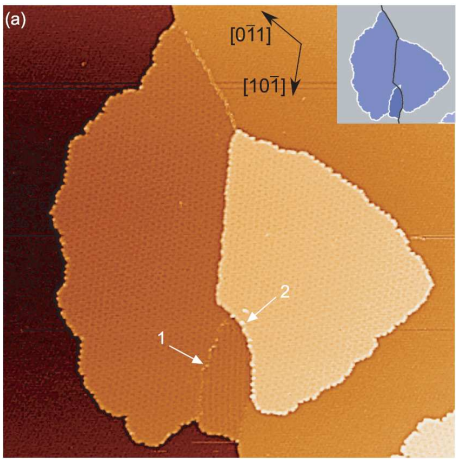

Figure 12: STM topograph (171×171 nm) of graphene grown by CVD on Ir(111) surface at 1120 K, ethylene partial pressure 6.10^{-6} mbar, issued from [54].

found that this growth rate in fact decreases as the dose increases, vanishing asymptotically Figure 13. The quantitative analysis of this behaviour was interpreted as the evidence that no carbon dissolves into the bulk of the substrate, that impinging carbon precursor molecules (here ethylene) do not stick on graphene covered regions, and that if they land on graphene-free regions, the carbon molecules have zero probability for desorption and are systematically decomposed in carbon adatoms [54].

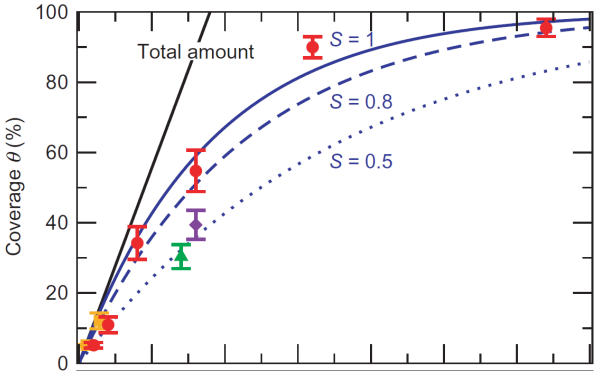

Figure 13: Graphene coverage as a function of the ethylene dose during CVD growth of graphene on Ir(111), as estimated from STM topograph, adapted from [54].

Elementary process during growth

The most straightforward picture of graphene CVD at atomic scale is that carbon precursors decompose into carbon adatoms, and that these adatoms attach one-by-one at the edges of existing graphene islands. Nevertheless, both DFT calculations and *in-situ* low-energy electron microscopy (LEEM) proved that this is not true [53]. LEEM revealed that the carbon adatom concentration increases until a critical value, before which no graphene island nucleates. This critical concentration is typically 0.013 monolayers (ML, 1ML being the carbon density of graphene on Ir(111)) Figure 14. Surprisingly, it was found that beyond this critical concentration, graphene islands do not grow with a rate which is proportional with the carbon adatom concentration, as one would expect from a simple model in which this growth rate is the difference between

the detachment and attachment rates, the former being usually independent of the adatom concentration, while the latter is usually proportional to this concentration. This surprising behaviour was interpreted as the manifestation that carbon monomers (adatoms), alone, cannot attach to graphene. Assuming an Arhenius law for the carbon multimer concentration, with, as an activation energy, the difference in energy between n isolated carbon adatoms and a carbon multimer E, with n atoms, and assuming that the energy of an individual adatom corresponds to the case of an ideal 2D gas, one obtains [66]:

$$v \propto c - c_{eq} = \exp\left(\frac{-E}{kT}\right) \times \left[\left(\frac{c}{c_{eq}}\right)^{n} - 1\right] \tag{9}$$

where v is the growth velocity, c is the carbon adatom concentration and c_{eq} is the C adatom concentration in equilibrium with graphene sheets.

Fitting the data with this expression by refining the value of n yields $n \sim 5$. As a consequence, carbon pentamers need to be formed before carbon can add up to the existing graphene islands. DFT calculations confirmed this view, by showing that the energy barrier for a carbon multimer to add up to a graphene edge decreases with the number of carbon atoms in the multimer [66].

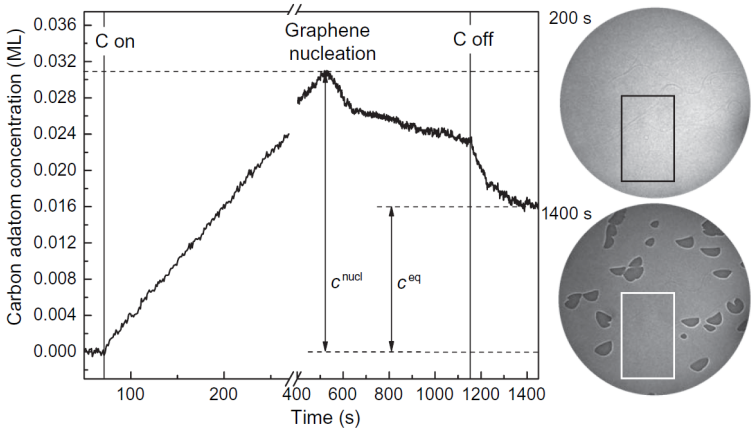

Figure 14: The C adatom concentration in equilibrium with graphene measured from electron reflectivity at 940 K (left panel). LEEM images (46 µm field of view) taken at 200 s and 1400 s (right panel). Boxes mark the graphene-free region where the C monomer concentration was determined, reproduced from [66].

Rotational domains

It was found that the twinned domains (i.e., whose carbon zigzag rows do not align with the dense-packed rows of the metal surface) only grow at the edges of the untwinned domains. For interpreting the observation that once nucleated, the twinned domains grow faster that the untwinned ones, it was invoked that they grow further away from equilibrium or that the attachment of carbon multimers to graphene edges is more difficult on twinned domains [53]. The reason for their nucleation at the edges of the untwinned domains was argued to be the result of the occasional formation of edge defects on the border of untwinned domains.

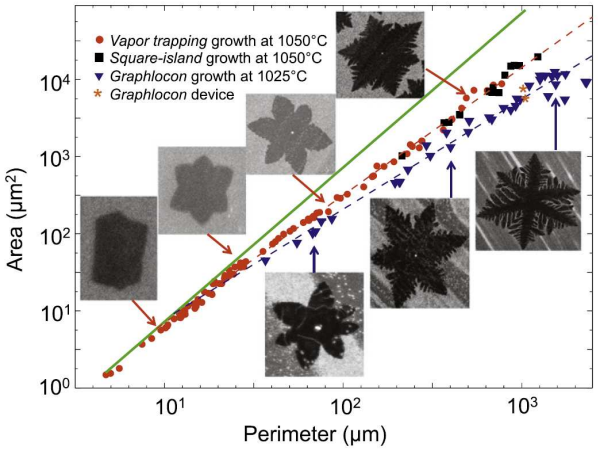

Figure 15: Shape evolution of graphlocons (monolayer dendritic graphene single crystals). Plots of log (island area) as a function log (island perimeter) for various growth conditions and techniques. Each data point represents an individual island and scanning electron microscopy images are shown for some of them. The dotted lines are linear fits of data points with perimeter $> 10\mu$ m and the solid line corresponds to the behaviour expected for perfect hexagonal (i.e. non-dendritic) islands, reproduced from [73].

The formation of twins was investigated on metal surfaces not having triangular symmetry, especially Cu(001) grains, which are often found in polycrystalline Cu foils used for low-cost production of graphene in a CVD reactor. Anisotropic growth velocities were observed, which were tentatively ascribed to the difficult attachment of carbon at graphene edges with some orientations with respect to the substrate crystallographic direction [72]. This anisotropy leads to the formation of lobe-shaped graphene islands.

Growth of dendritic/compact graphene islands

In the CVD on copper, low growth rates are achieved even close to atmospheric pressure conditions. This is presumable the result of the low catalytic activity of Cu, which only convert a small fraction of the impinging carbon precursor into a 2D gas of carbon adatoms. These small adatom concentration, combined with large mobility of adatoms, presumably are the reasons for the low graphene nucleation density. Islands centres are typically separated by 100 μm. Tuning the growth temperature, it was shown that the shape of the graphene islands can be tuned from dendritic to compact Figure 15, which is an evidence that the growth can be made diffusion-limited (dendritic islands) [73].

Role of substrate defects in CVD

I finish the discussion of CVD of graphene by discussing the role of defects in the formation of multilayer graphene patches on a polycrystalline substrate (Cu). Cu actually became a popular substrate for graphene growth because it is, just like Ir, a low carbon solubility metal for which one thus expects that growth is self-limited to a single layer of graphene. However, already in the first reports [63] and since then in almost all other reports, few layer graphene regions, representing from a few 1% to more that 10 % of the surface, form on Cu. By interrupting growth before the completion of a

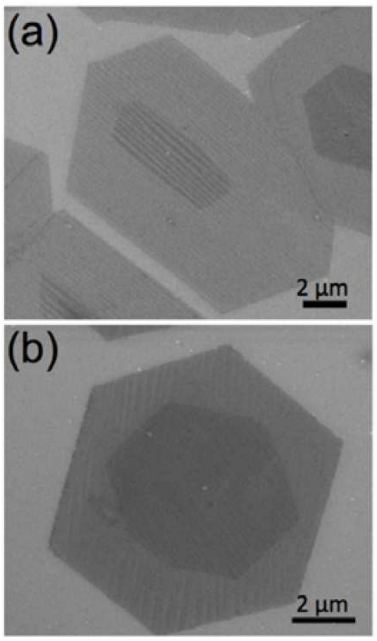

Figure 16: Scanning electron microscopy images of graphene on Cu. The medium-gray regions are faceted single-layer sheets, the darker regions, which are also faceted, have two graphene layer, reproduced from [74].

full graphene layer, we found that two kinds of graphene islands form: large ones, which may have shapes from dendritic to compact, and small ones, all compact, some below the larger islands, some not Figure 16. This observation is the evidence that two different growth processes are at play. We argued that the first one is a surface growth one (leading to the formation of the large islands), and that the second one is due to surface segregation upon cool down (see next section) of carbon atoms stored inside grain boundaries. This scenario is an alternative to the one invoking intercalation of carbon atoms beneath preformed graphene islands [74], which cannot account for the occurrence of small islands which are not below larger ones.

Developing a pulsed CVD process, consisting in pulsed injection of methane followed by idle time under H_2/Ar atmosphere, during which the Cu defects are depleted from carbon, we showed that purely single layer graphene can be achieved Figure 17.

1.3.2 *Carbon surface segregation*

In metals like Ni and Ru, the solubility of carbon around 1000 °C is sufficient for carbon to be preferably dissolved into the bulk of the metal. Decreasing the metal temperature also decreases the carbon solubility. It was found that on Ni(111), a single layer of graphene can be formed accordingly in a small temperature window around 900 °C, while at lower temperature several layers form on the Ni(111) surface (Figure 18, [76]).

As for CVD, LEEM was employed to unveil the elementary processes governing growth by segregation. A linear increase with the square root of time of the area of growing graphene islands was found on Ru(0001) (Figure 19). This observation was accounted for in a model assuming a constant carbon surface adatom concentration c_0 in equilibrium with the carbon bulk concentration, and a uniform bulk concentration

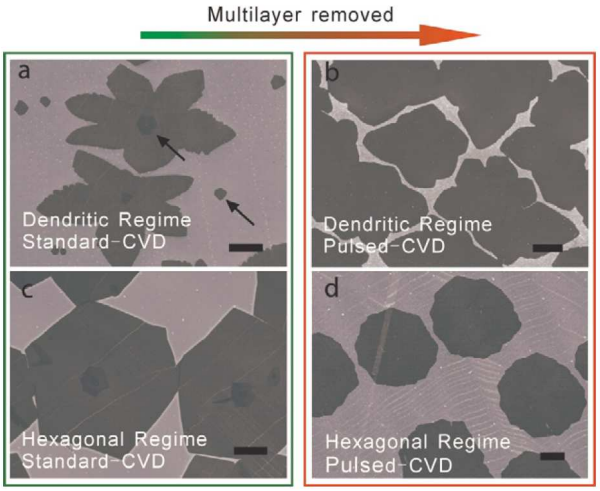

Figure 17: Scanning Electron microscopy of raw graphene samples on Cu for which growth was interrupted before reaching full surface coverage, showing for comparison graphene grain morphology for standard-CVD growth (left column) and pulsed-CVD growth (right column). a) Dendritic growth with partial pressure 2.8 µbar CH_4, 0.1 mbar H_2, and c) hexagonal flakes morphology with partial pressure 50 µbar CH_4, 25 mbar H_2. Temperature was always kept at 1000°C. Duration for a) and c) are 20 min and 5 min, respectively. For the right column, same parameters are used except for the pulsed-injection of CH_4 gas. Arrows in a) indicate the different shape in the small multilayers. Scale bars are 10 µm [75].

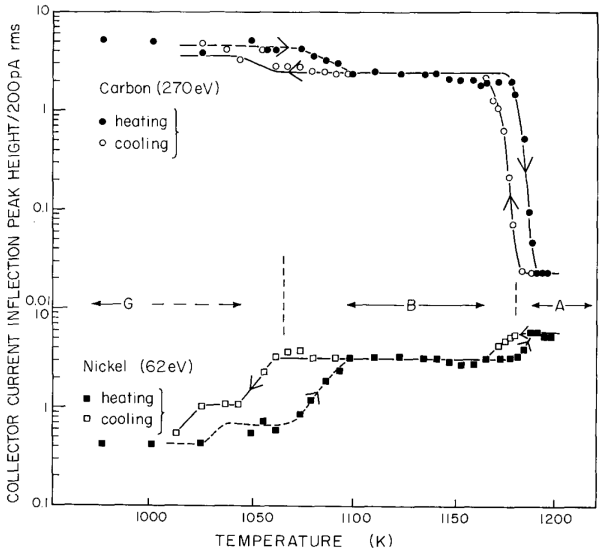

Figure 18: Segregation of impurity C from Ni(111) condensed monolayer graphene, and multilayer graphene. Temperature dependence of the 270 eV carbon and 62 eV Nickel Auger peaks. Three states (A, B and G) of different carbon coverages are identified, reproduced from [76].

c_1 before segregation starts [77]. The diffusion equation solved in these conditions yields an error function solution for the bulk concentration:

$$c_b(z,t) - c_0 = (c_1 - c_0) \times \mathrm{erf}\left(\frac{z}{2\sqrt{D_b t}}\right) \tag{10}$$

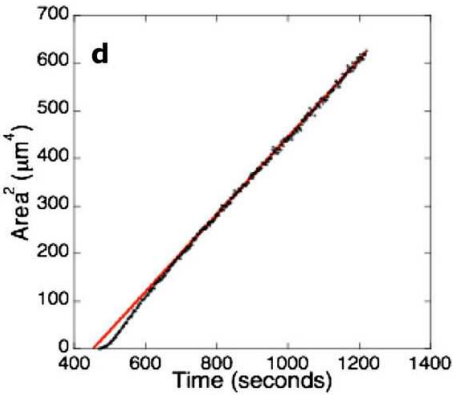

Figure 19: Characterizing the growth rate of graphene island. Square of island area vs. time. The red line is a linear fit to data for time > 700 s, reproduced from [77].

where c_b is the carbon concentration in the Ru(0001) in the direction z perpendicular to the surface ($z > 0$ in the bulk) and D the bulk carbon diffusion coefficient.

The time integral of the divergence of the concentration at the surface gives the area of the islands:

$$A(t) \propto (c_1 - c_0) \times \sqrt{D_b t} \tag{11}$$

which is indeed observed experimentally an shows that growth is bulk-diffusion limited.

This result also reveals the trade-off between bulk diffusion efficiency at higher temperature (higher D) and larger driving force for segregation (higher $c_1 - c_0$) for a lower temperature. In practice, for growing high quality one should prefer a high diffusion and a small driving force, for the slow growth of high quality graphene islands, i.e. growth at temperatures close to the temperature at which carbon solubility rapidly drops.

1.4 ELECTRONIC PROPERTIES OF EPITAXIAL GRAPHENE ON METALS

The metal-carbon interaction not only influences growth (e.g. segregation vs CVD) and structure (e.g. the amplitude of the corrugation along moiré superstructures), but also the electronic properties of graphene. On the one hand, system with weak graphene-metal interaction provide very convenient playgrounds for probing the electronic properties of quasi free-standing graphene with very well-defined structure (as being grown under perfectly controlled conditions) thanks to surface science probes [9], and for manipulating these properties through weak graphene-metal interaction effects. On the other hand, strongly interacting graphene-metal systems are models for understanding the electronic nature of metal-graphene contacts [78], which are a key ingredient in any electronic device.

1.4.1 *Physisorption or chemisorption*

The tendency of metals to form covalent bonds with carbon may vary according to the electronic valence shell occupancy of this metal, the electronic density of the corresponding electronic orbitals Figure 20 (which depends on their filling and their extension) [79]. In view of these criteria, one expects lower interaction from left to right and

top to bottom of the periodic table of elements, which is indeed observed [80]. The occurrence of metal surface states, on the contrary , does not seem required for a strong interaction, though it might have some influence. It is believed, for instance, that there exist some degree of hybridization between the Ir(111) surface state and graphene [9], but that the interaction in this system remains weak. Surface states are also well-known on Cu(111), but the graphene-Cu(111) interaction is known to be weak [41] .

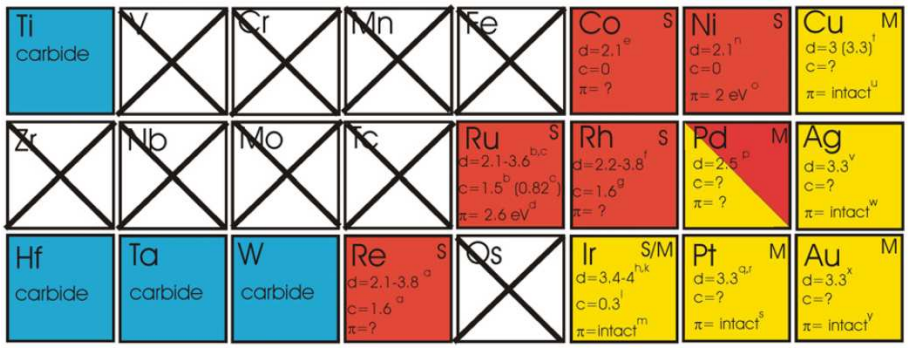

Figure 20: Summary of the interactions between transition metals and graphene. For the elements labeled in blue, graphene may grow on the bulk-carbides of these elements. Elements in red are characterized as metals that interact strongly with graphene and elements in yellow are those that interact weakly. 'S' or 'M' in the upper right corner of each element box indicates if graphene forms single or multiple rotational domains, 'd' is the reported graphene-metal separation in Å. The buckling or corrugation of the graphene sheet is given by 'c' in Å, and the amount of downward shift of the π-band is given by 'π' ('Intact', means that a linear dispersion at the Dirac point is still observed), issued from [80].

The formation of covalent-like C-metal bonds, which are short, typically 2 Å, implies a small distance between graphene and the metal surface. This trend was unveiled in DFT calculations [78] and confirmed by experimental data. In case of a pseudomorphic system, graphene/Ni(111), indeed a 2.1 Åwas found [35]. In most cases, however, the graphene/metal systems are not pseudomorphic, and characterized by moiré superstructures. Since the local C/metal stacking varies locally in the moiré. One expects a varying interaction and graphene-metal distance at the nanometer scale, which is indeed predicted by DFT calculations Figure 21 [81, 6] and observed experimentally, for instance in graphene/Ir(111) [43, 82] and graphene/Ru(0001) [83, 84, 85] Figure 22. Note that in the latter system the literature reports very different values of the graphene corrugations. A robust conclusion seems that the average metal-graphene distance is lower in strongly interacting systems, and that the moiré corrugation is larger in these systems, driven by formation of local chemical bonds on some sites of the moiré.

Properly describing the graphene-metal bonding is in principle very demanding from a computational point of view. In a weakly interacting system like graphene/Ir(111), van der Waals interaction must be taken into account. DFT calculations including this interaction reveal that there exist a global graphene-metal delocalized repulsion, due to the van der Waals interaction, and that the bonding is ensured by local C-metal bonds. They occur at sites where the centre of C rings prolong a fcc or hcp (centre of C hexagon above threefold coordinated hcp site) like stacking of the metal atoms of the substrate, which have some tendency to a covalent character (3.2 Å, i.e. lower than the

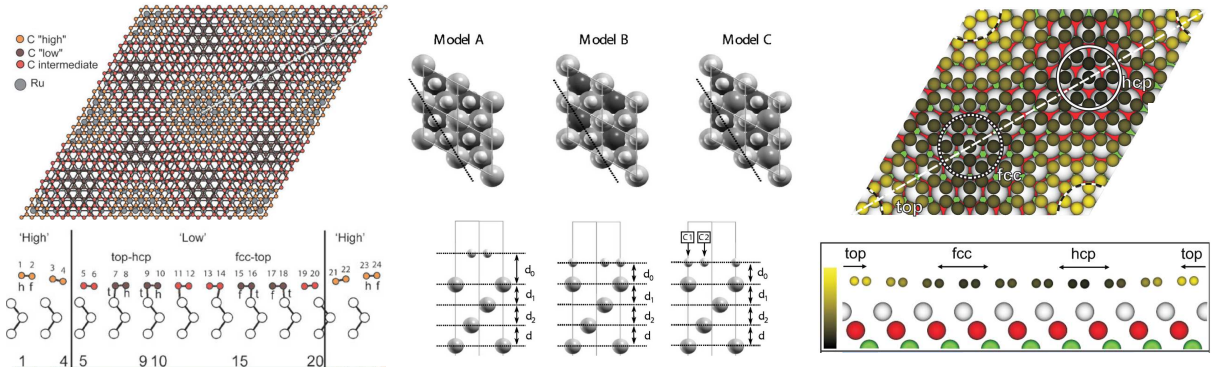

Figure 21: from left to right,top: top view of the relaxed structure of graphene/Ru(0001) [81], Ni(111) [33] and Ir(111) [43] respectively. Bottom: corresponding side view along the diagonal line (Ru and Ir) and in the plane indicated by a dotted line (Ni). In the Ni case, the three possible geometries are obtained according to the adsorption sites of carbon atoms.

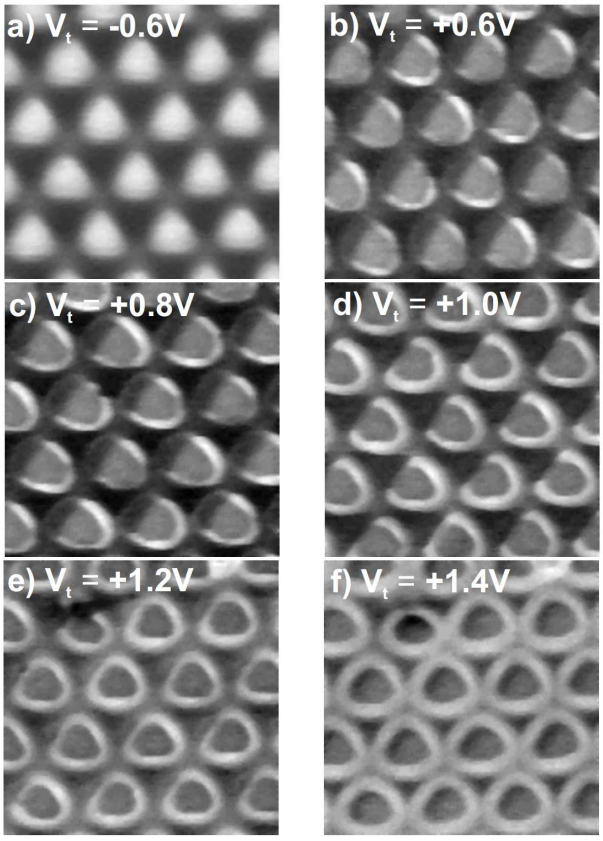

Figure 22: Voltage dependent STM images (100 Å^2) of graphene on Ru(0001) taken at the same area. The appearance of the moiré changes from a hexagonal pattern of maxima for the filled states to bright rings for the empty states, reproduced from [83].

C-C distance in graphite, but larger than an actual covalent bond) [43]. In a strongly interacting system, like graphene/Ru(0001), van der Waals interactions are needed to account for the lower bonding at some moiré sites [86].

1.4.2 *Band gap opening and charge transfers*

Covalent-like C-metal bonds, even locally on the moiré, make the two C sublattices inequivalent, which result in the formation of a strong band gap at the Dirac point (which might not be referred to as a Dirac point any more since the electronic properties in such a case have nothing similar to those of Dirac fermions). Such hybridization effects resulting in the formation of bonding and antibonding electronic states, with band gaps of the order of 1 eV, were observed on Ni(111) [87] and Ru(0001) [88] for instance, and to a much lesser extent surmised on Ir(111) [9] (Figure 23). Noteworthy in strongly interacting systems, the second layer of graphene recovers the properties of almost free-standing graphene [88], like is also the case in graphene/SiC [89].

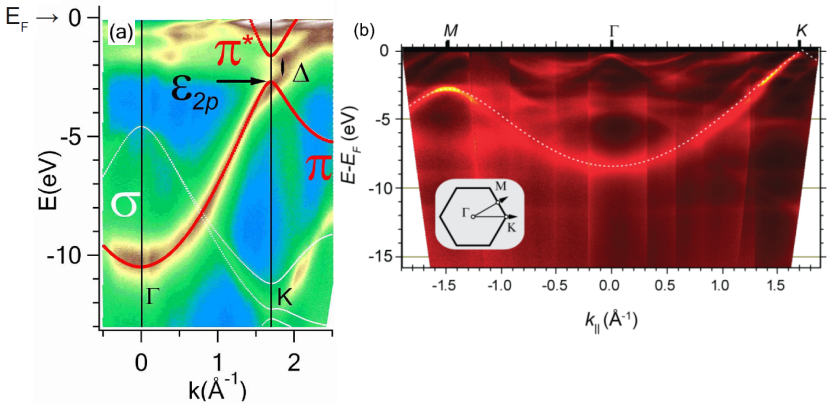

Figure 23: Electronic structure of graphene on a); Ni(111) along $\overline{\Gamma K}$, b); on Ir(111), angle resolved photoemission spectroscopy (ARPES) map showing the dispersion of the π band for the ΓK and ΓM directions. Inset indicates how the ARPES scanning was performed ($h\nu$ = 55 eV, T= 80 K), issued from [87, 9].

Besides bandgaps, charge transfers between graphene and the metals were also predicted and observed. They result in p-doped, of the order of a few 0.1 eV (from 2 to 6 $\cdot 10^{12} cm^{-2}$) graphene in the case of weakly interacting systems, and in strong n-type doping of graphene, of the order of 1 eV or more, in strongly interacting systems. This effect was related to the difference in work-function between free-standing graphene and the metal: electrons tend to accumulate in the highest work function material. This simplistic view must be corrected by the graphene-metal interaction, which can be quantified empirically from the graphene-metal distance Figure 24 [78].

1.4.3 *Superpotential effect*

The graphene-metal moiré is sensed by electrons as a superpotential. This superpotential was argued to be sufficiently strong to induce a confinement of electrons on some sites of the moiré in graphene/Ru(0001) [90]. In graphene/Ir(111) it is rather weak, but results in the opening of small band gaps (so-called minigaps) at the six corners of the small Brillouin zones associated with the moiré and centred at the K point of the graphene FBZ. Together with these minigaps is observed a replication of each Dirac cone Figure 25 [9].

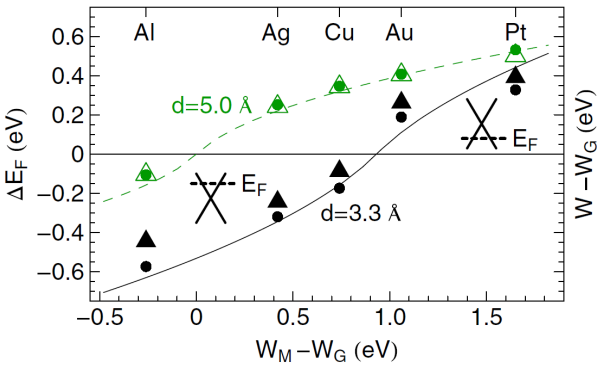

Figure 24: Calculated Fermi energy shift with respect to the conical point, ΔE_F (dots), and change in the work function $W - W_G$ (triangles) as a function of $W_M - W_G$, the difference between the clean metal and graphene work functions. The lower (black) and the upper [gray (green)] results are for the equilibrium (~ 3.3 Å) and a larger (5 Å) separation of graphene and the metal surfaces, respectively. The insets illustrate the position of the Fermi level with respect to the conical point, reproduced from [78].

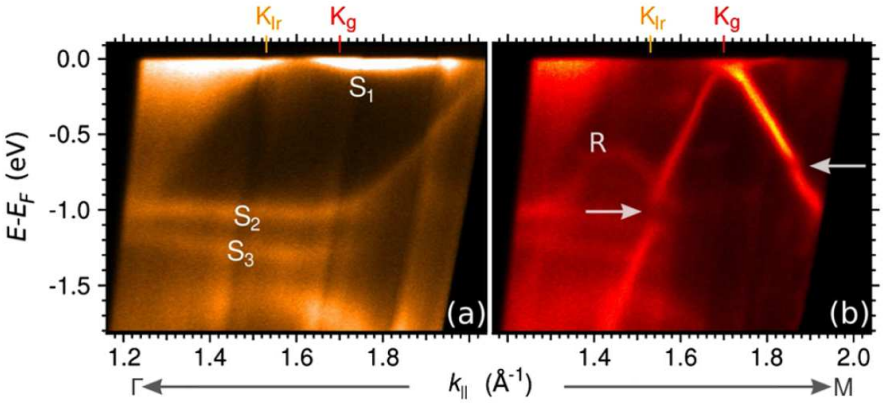

Figure 25: ARPES spectrum of (a) clean Ir (111) and (b) graphene covered. Horizontal arrows denote the minigap in the primary Dirac cone. A visible replica band is labelled as R, S1-S3 are surface states, reproduced from [9].

1.5 HYBRID SYSTEMS

Graphene-based hybrid systems combine graphene with other materials and exhibit properties which either combine the properties of both materials or novel properties stemming from the graphene-material interaction. Chemists have produced a broad range of graphene-molecules hybrids [91] which will not be reviewed here. We will rather focus on high quality systems whose preparation rely on surface science approach, which combine graphene with ultra-thin films, nanoclusters, molecules, or atoms and exploit interface effects.

1.5.1 *Exploiting the graphene-metal moiré*

The moiré between graphene and metals has been used for the preferential adsorption of various transition metals. Metal evaporation onto graphene/Ir(111) first demonstrated the importance of the moiré in the self-organization of nanoclusters onto graphene [6]. A variety of clusters, having a size of a few to several 10 atoms could be obtained according to this method, on various graphene/metal surfaces [92, 93, 94, 95]. The very high degree of order in the nanocluster assemblies, designate them for size dependent studies.

A mechanism for the bonding of the clusters onto specific sites of the moiré, was proposed based on DFT calculations. In these calculations, it was found that a rehybridization of C atom below the clusters maximizes the number of C-metal bonds, which reduces the total energy of the system [96]. Recent experimental data revealed different C-metal bonding supporting this scenario [97]

They were used to reinforce the moiré superpotential and modify accordingly the electronic band structure of graphene, through a noticeable change of the slope of the linear π bands of graphene [98]. They were also studied to explore nanomagnetism onto graphene: indications for magnetic interactions between clusters, a key ingredient for the achievement of collective magnetic states controlled by graphene's charge carriers [99], and a surprisingly weak influence of the graphene/cluster interface on the magnetic porperties, could accordingly be unveiled [12].

The moiré was also found to drive the organisation of molecular and even atomic species. In the first case, on graphene/Ru(0001), it was possible to influence the formation of supramolecular networks [100], which open a broad range of potentialities in terms of surface functionalisation. Still on graphene/Ru(0001), tetracyano-p-quinodimethane molecules were found to acquire a magnetic moment, which was traced back to the donation of electrons from graphene (strongly electron doped on Ru), which was argued to unbalance the majority and minority spin populations [101]. For dense molecule layers, a collective magnetic order state was found and interpreted as the result of intermolecular orbital hybridization. In the later case, on graphene/Ir(111), the preferential adsorption of atomic hydrogen, onto the moiré sites, was found to open a sizeable band gap of about 0.5 eV at the Dirac point [102].

1.5.2 *Graphene intercalation compounds*

Intercalation in graphite has been known for decades [103]. It consists in inserting species between successive graphene planes. In graphene on metals systems, it consists of sandwiching some species between graphene and its substrate, a process which also has been studied long ago [8]. Since a few year there is considerable effort in developing novel graphene intercalated compounds, in the view of manipulating the graphene-substrate interaction and of inducing novel properties in graphene. In two sections of this manuscript devoted to experimental results I will address these questions more into details.

Noteworthy, despite the large body of work devoted to the preparation of graphene-metal intercalated compounds, relatively little is known about the intercalation process. Defects [94, 13] and free-edges [104] were identified as pathways for intercalation, and it was found that intercalation is easier, i.e. efficient at lower temperature, in

those graphene-metal systems which are characterized by a lower interaction. For instance, intercalation occurs only several 10°C above room temperature for oxygen on graphene/Ir(111) [105], while around 500°C on graphene/Ru(0001) [104]. This indicates that the energy barrier needed for lifting up graphene from its substrate and allowing the insertion of foreign species limits the intercalation process. As we will see latter in this manuscript, other processes happen to be relevant as well during intercalation.

Intercalation was employed to quench the graphene-substrate interaction in several systems. In this view, the intercalation of a single atomic layer of Au allowed to observe Dirac cones in graphene initially grown on Ni(111) [11], and oxygen intercalation produced similar effect in graphene/Ru(0001) [104]. Dual intercalation of Si and O even allowed such an electronic decoupling between graphene and Ru(0001) that electronic transport could be studied experimentally through graphene, without noticeable shunt by the Ru substrate [106].

The intercalation of Au not only decouples graphene from a metal like Ni, but also it induces a strong effective spin-orbit interaction in graphene, actually a Rashba effect, produced by the strong charge density gradient at the graphene-Au interface (thus a strong interface electric field, and in the rest-frame of the electron, an effective magnetic Rashba field) [107]. The intercalation of few atomic layers of Co between graphene and an Ir substrate tat we have studied, was used to probe the relative importance of the graphene/metal interface in the magnetization of the Co layers. This allowed us to reveal that the graphene/Co interface is characterized by a surprisingly large interface magnetic anisotropy energy of 1.6 mJ/m^2 [108], i.e. larger than most interfaces between ferromagnets and other materials. The reason for this anisotropy presumably lies in the strong Co-C hybridization. Such systems exemplify the easy control of the magnetization direction of ferromagnetic layers thanks to a protecting topmost interface. The study of the intercalation of a single layer of Co between graphene and Ir(111) moreover revealed exciting effects originating from the presence a moiré at the interface between graphene and Co. Such a moiré was found to induce a periodic (nanometre scale) magnetic pattern, which was argued to yield a magnetic pattern in graphene (Figure 26), on the basis of DFT calculations [109]. The experimental evidence for such an effect is however still lacking.

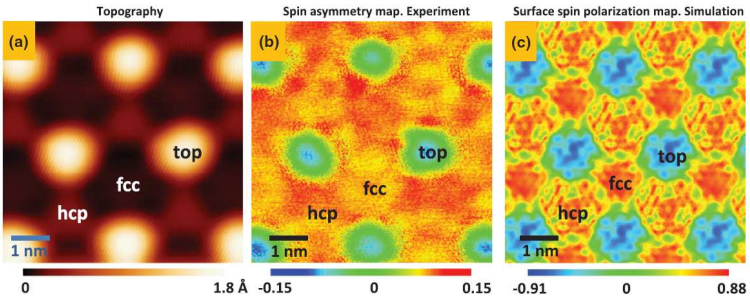

Figure 26: Local effective spin polarization of the graphene layer on Ir(111), (a) Topography of an intercalated region. (b) Spin asymmetry map of the region shown in (a) which reveals the inversion of the effective local spin polarization between the top sites and fcc/hcp sites. (c) Simulated surface spin polarization map. Panels (b) and (c) define a magnetic Moiré pattern of the graphene-Co/Ir(111) intercalation region for an applied bias voltage of -1 V. [109].

2

EXPERIMENTAL TECHNIQUE AND METHODS

In this chapter, first I briefly describe the experimental techniques which I have employed to probe the structure, vibrational, and electronic properties of graphene-based systems. A large set of *in situ* and *ex-situ* techniques were applied: scanning tunnelling microscopy (STM), atomic force microscopy (AFM), reflection high-energy electron diffraction (RHEED), low-energy electron diffraction (LEED), low-energy electron microscopy (LEEM), and Raman spectroscopy. Then, I present the ultra-high vacuum (UHV) system which I have been massively employed during this work at Néel Institute, and describe the growth methods used, ending this chapter with an illustration devoted to graphene growth on thin Ir(111) films on sapphire.

2.1 INTRODUCTION

The objective of my research is to provide a better understanding of the fundamental properties of graphene. This objective usually requires cross-characterizations with techniques addressing complementary scales and sensitivities, as we will show in the three chapters following this one, which are devoted to the results I obtained during my work. Briefly summarizing the experimental approach reported in these chapter, we have combined:

- local electronic and vibrational spectroscopy,
- real-time microscopic characterizations while the systems are grown,
- high resolution measurements providing insights into the graphene/support interface.

2.2 RAMAN SPECTROSCOPY

Raman spectroscopy is a spectroscopic technique that makes use of inelastic scattering of light with matter. When, the light beam is directed towards the sample, the energy of a small fraction of the light photons changes after interacting with the atoms of the sample or molecules: these photons are said inelastically scattered, a phenomenon known as the Raman effect. This change in energy carries the information about vibrational, rotational and other low frequency modes of the material under analysis. The inelastic scattered radiation can correspond to either an excitation of the sample's phonons (their energy has increased in this case, and this part of scattered signal is called Raman Stokes signal), or to their relaxation (the phonon's energy has decreased and the effect is called Anti-Stokes Raman scattering, noted A-S) as sketched in Figure 27 for Feynman diagram. The Rayleigh signal, corresponding to elastically (unchanged energy) photons, overwhelms the Raman one by orders of magnitude in terms of intensity. As a consequence, the inelastically scattered photons have to be carefully filtered out in an experimental setup by using several monochromators in series.

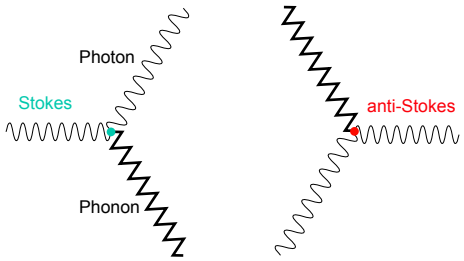

Figure 27: Feynman diagrams of Stokes and anti-Stokes scattering processes, showing energy loss and energy gain of the photon due to phonon creation and absorption.

Raman spectroscopy has been used extensively to probe structural and electronic characteristics of carbon materials, specially the sp^2 systems [110], i.e graphene. It provides information about disorder and defects [111], the stacking order between graphene layers [112], the number of graphene layers stacked in a Bernal configuration [113, 114], the effect of strain [115] and charge transfer [116]. Further information about the electronic structure and the dispersion of phonons near the Dirac point [117] can be achieved as well.

2.2.1 *Raman signature of graphene*

Graphene has a very specific signature in Raman spectroscopy, and is therefore quite effectively identified by this method. The most prominent features in the Raman spectra of graphene are characterised by the presence of two strong symmetry peaks at G ($\sim 1582 cm^{-1}$) and 2D ($\sim 2700 cm^{-1}$).

The G band phonon has a very small wave vector q. It is a first order Raman feature originating from the zone-centred, in plane optical phonon modes E_{2g} (strong electron-phonon interaction near $q = 0$). The G band is related with the in-plane TO (transverse optical) and LO (longitudinal optical) vibrations. The G band is the only band in graphene coming from a standard first order Raman scattering process: only one phonon participates in scattering (Figure 28).

The 2D band is a second order two-phonon feature. It involves a two-phonon processes with two TO phonons near the K point associated with intervalley wave vectors q and -q (Figure 28). The large intensity observed in a Raman spectrum of graphene for such a second order process as that of 2D mode is ascribed to its doubly-resonant nature.

In graphene with defects, other features are visible in a Raman spectrum. One of them corresponds to the D mode, which is associated with near K-point phonons ($\sim 1350 cm^{-1}$). Like the 2D mode, it is a second order process, and it also involves two TO phonons. It also involves an intervalley process, sketched in Figure 28, only allowed when the sp^2 symmetry is broken, as is the case for instance at a graphene edge or close to a carbon vacancy.

Other modes may be observed in graphene, especially in the presence of structural disorder. We will not describe them here as we will not encounter them in the spectrum which we will present in the next chapters. For more information about these modes, the reader is recommended to read, for instance, [117].

The influence of defects in the Raman spectrum of monolayer graphene on a SiO2/Si substrate is illustrated in Figure 29: upon increasing the density of defects in graphene, the intensity of the 2D mode decays while that of the D and D+D′ modes increases. At large defect concentrations, also shifts and broadening of the peaks occur [118].

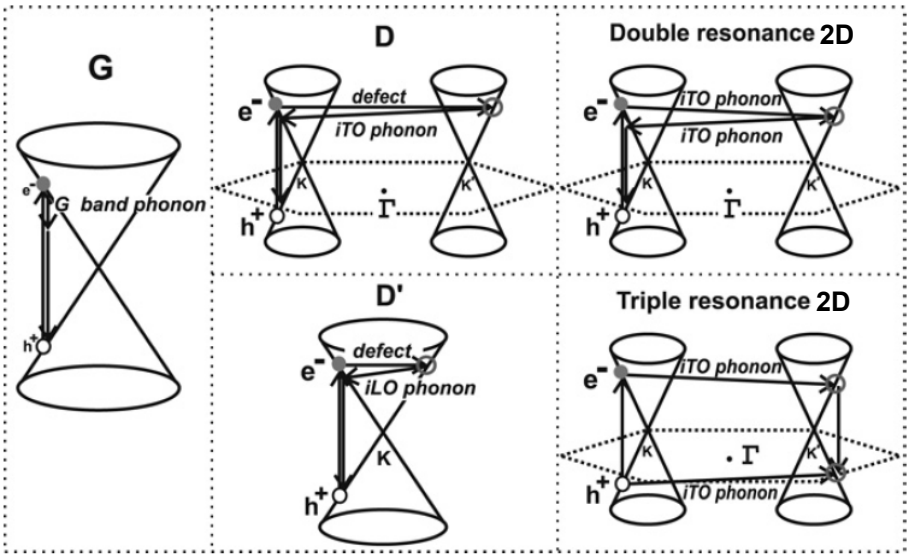

Figure 28: Double resonance intervalley D-band process (centre), first order G band process (left) and double resonance two phonons assisted intervalley 2D-band process (right) [117].

Due to electron-phonon coupling, the Raman shift associated to the vibrational modes of graphene, as well as the lifetime of these modes, change with the charge density of graphene [119, 116]. Indeed, in a simplistic picture, the creation of an electron-hole pair following the absorption of a phonon and preceding the emission of another phonon, can be partly hindered depending on the Fermi level (no states available in the valence band for forming a hole). In such a case the screening of the phonon by electrons is hindered. This translates into a softening and a broadening of the G modes, as well as a narrowing of the 2D mode, upon decreasing the charge density of graphene. The 2D mode is softened as the charge density increases from the hole- to the electron-doped regime. These effects are observed on Figure 30. It was found that the G mode softening is typically 1 cm^{-1} per $10^{12} cm^{-2}$ change of the charge carrier density [120].

Intuitively, tensile strains are expected to make vibration modes softer, while compressive ones are expected to have the opposite effect. This is actually what is observed in graphene [121], as shown in Figure 31 in the case of a uniaxial strain. It was found that the variation of the 2D mode, for instance, is - 64 cm^{-1} per percent of strain [121].

Raman spectroscopy is a noninvasive, direct, and sensitive probe of phonons in graphene layers. In the present work, Raman spectra were recorded with a Witec α 500 Micro Raman spectrometer system using two different laser beam (532 nm and 633 nm). The spectrometer is a 1800 lines/mm grating allowing spectral resolution of 0.01 cm^{-1} for 10 s acquisition time. A confocal optical microscope with a $\times 100$ objective lens was used, yielding a spot-size fixed by the diffraction limit of 300 nm and fixing the lateral resolution in Raman maps. The sample sits on a piezoelectric stage which is scanned to take a Raman spectrum at specific points along the graphene sheet. The microscope's objective serves both to focus the incoming laser light onto the surface, and to gather the outcoming light, which is then directed towards the monochromator. The Rayleigh signal, which is orders of magnitude higher than the Raman signal, has to be attenuated using a notch filter. Finally, the photodiode coupled to a monochromator

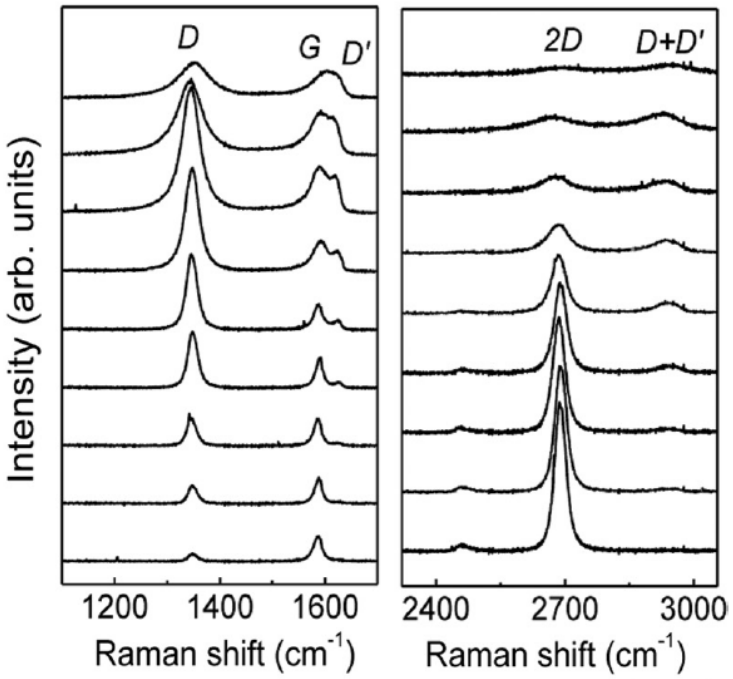

Figure 29: Raman spectra of fluorinated graphene, with increasing defect concentrations (from bottom to top). From [118].

measures the spectrum. Our setup includes a piezo-electric sample stage interfaced with the acquisition software.

2.3 ATOMIC FORCE MICROSCOPY

Atomic force microscopy is a high resolution imaging technique in which a several nanometre sized tip on the end of a cantilever is mechanically scanned across a sample. As the surface is scanned, the oscillatory amplitude of the cantilever will change as it encounters differing topography. A feedback mechanism alters the z-height of the piezo crystal and maintains constant amplitude, image of the surface topography is obtained Figure 65. The details of tip-sample force characteristics are determined by both long and short-range contributions, e.g. electrostatic, magnetic and van der Waals forces. Additionally, under ambient conditions the sample surface is covered by a thin water film leading to meniscus forces. Contribution and distinction between different forces is rather complex [122, 123, 124].

Depending on the tip-surface working distance AFM is characterized by different mechanical behaviours, which define different AFM operation modes [124]. In the static mode, no vibration is imposed to the tip, which is merely dragged across the surface during the scan. This mode relies on soft cantilevers, which can be deflected by the weak atomic forces, and on suitable eigenfrequencies lying away from the resonance frequency of the cantilever. These requirements make this apparently simple mode of operation difficult to implement in many situations; in addition, it results in both the tip and surface being damaged during the scan. Dynamic modes, in which the tip is oscillating perpendicular to the surface while scanned, are more widely employed. Making the tip oscillate with an amplitude that may change between sub-Åfor stiff cantilevers to hundreds of Å, for soft ones avoids the problem where the tip jumps

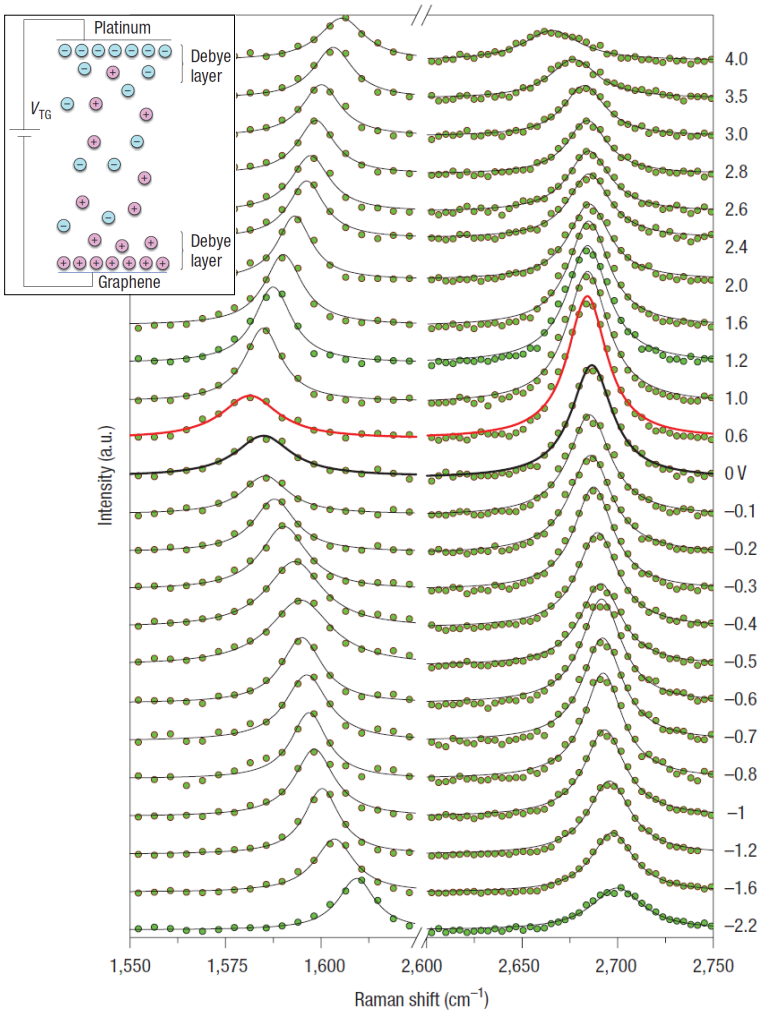

Figure 30: Raman spectra of graphene as a function of gate voltage, between -2.2 V and + 4.0 V. The dots are the experimental data, the black lines are fitted lorentzians, and the red line corresponds to the Dirac point. The G peak is on the left and the 2D peak is on the right. The inset is a schematic illustration of polymer electrolyte top gating, with Li^+ (magenta) and ClO_4 (cyan) ions and the Debye layers near each electrode [120].

into contact with the surface and hence maintains both the tip and the surface intact during the scan.

Two major scanning modes are in use: (i) in the amplitude modulation regime the oscillation frequency is kept constant and out of resonance and the oscillation amplitude and the phase are measured, while (ii) in the frequency modulation regime the oscillation frequency is maintained at resonance during the scan and the oscillation amplitude is kept constant. The latter mode, which for UHV is the most suited for achieving true atomic resolution, can be run either keeping the resonance frequency constant and measuring the corresponding vertical displacement of the sample (similar to the constant current mode of STM), or keeping the sample height unchanged and hence measuring changes in the resonance frequency (detuning). The latter mode is also called the non-contact mode (NC-AFM), when the average working tip-surface distance is around 2-4 Å, which is within the region of attractive forces; in the tapping

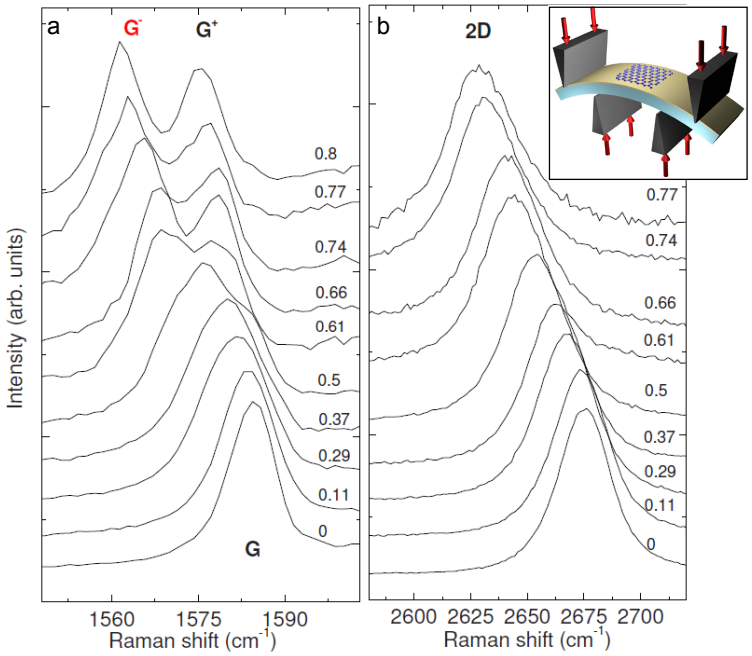

Figure 31: (a) G and (b) 2D peaks as a function of uniaxial strain. The spectra are measured with incident light polarized along the strain direction, collecting the scattered light with no analyser. Note that the doubly degenerate G peak splits in two subbands G^+ and G^-, while this does not happen for the 2D peak. The strains, ranging from 0 to 0.8%, are indicated on the right side of the spectra. experimental setup showing the four point bending of the graphene deposited on a flexible substrate [120].

mode the working distance is smaller, and mostly repulsive forces are probed. As in the majority of AFM instruments working in ambient pressure conditions, we have employed this tapping mode for all images presented in the present work.

2.3.1 *Phase contrast*

In the frequency modulation tapping mode which we have employed, we obtain a topography signal (the change in frequency of the tip excitation needed to maintain a constant amplitude for this excitation), a phase signal (the phase shift between the excitation and the actual tip oscillation), and an error signal (due to the necessarily imperfect regulation on the amplitude of the tip oscillation).

The phase signal provides information about dissipative forces acting on the tip. In the case of graphene on SiC, it was found that in air, markedly different phase signals were obtained on graphene with different number of layers [125] or between graphene and the reconstructed SiC surface [126]. These differences were ascribed to a different tendency of the corresponding surface to adsorb molecules from the environment, and, as a result, different capillarity forces between tip and sample. We will make use of this effect to identify different kinds of graphene regions in the following of the thesis.

The AFM used in this work was a VEECO D3100. We used silicon tips with a maximum radius of curvature of 10 nm at their apex, mounted on silicon cantilevers, operated close to their resonant frequency, typically 280 kHz and with oscillation amplitudes of about 10 nm.

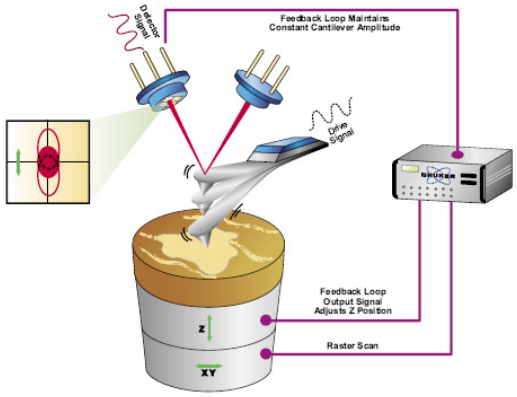

Figure 32: Schematic of tapping mode in AFM. The cantilever is driven to oscillate up and down at near its resonance frequency, typically 100 nm. Image from Bruker AFM Probes.

2.4 SCANNING TUNNELLING MICROSCOPY AND SPECTROSCOPY

Scanning tunnelling microscopy is a powerful tool for studying the structural and electronic properties of conducting surfaces. It consists of a sharp tip scanning the surface of a sample, in a regime of such tip-sample distances that electrons can tunnel to (from) the tip from (to) the sample surface. In practice this implies very short distances between the surface and the tip apex, of the order of 1-10 Å. Due to the exponential decay of the tunnelling current as a function of the tip-sample distance, STM is intrinsically well-suited to atomic resolution imaging [127]. Since the conductance (first derivative of the current with respect to the voltage) is approximately proportional to the local density of states [128], the technique is also capable of local electronic spectroscopy in a mode in which the current is measured as a function of the bias applied between tip and sample.

STM can be performed in the constant current or constant height mode. In the first mode, which we have used in the present work, an electronic feedback loop modifies the distance between tip and sample on the fly during the scan, thereby ensuring a constant current during the image acquisition (Figure 33). In this case the STM image consists of spatial variations of the sample-tip apparent distance. Note that what is measured is only the change of the tip-sample distance during the scan, not the actual absolute distance which remains unknown. Also, even the change of the distance measured during the scan may not necessarily correspond to the actual change of the surface height (e.g. when scanning over a molecule) as what is basically measured is the local density of states. Most STM studies are performed from room temperature down to low or very low temperatures. The low temperature, when operating at liquid helium or nitrogen temperatures, provides thermal stability which is beneficial to high resolution distortion-free imaging, and is also a requirement for high energy resolution spectroscopic analysis.

The present work reports STM studies with the help of three STM systems. One is operated at room temperature, under UHV, in the same environment where the samples are grown at Néel Institute. It is a OMICRON-1 STM, whose head is mounted on spring-supported cradle, and consists of tripod at the end of which the STM tip is held. The tripod piezoelectric system allows one scanning a sample surface about a horizontal line on the sample. The second STM system is a home made scanning probe microscope operating inside a dilution refrigerator reaching very low temperature (100 mK). It combine AFM/STM working at cryogenic environment (10^{-7}mbar). Samples

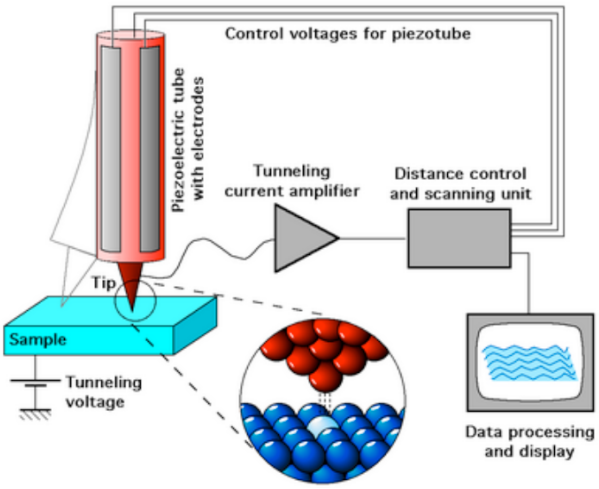

Figure 33: Schematic of operation mode in STM, from Wikipedia

studied in this STM have been exposed to air before measurements. The third STM system is also a very low temperature one, installed at CEA-INAC. Samples studied in this STM have been exposed to air.

For local measurement of the density of states, the feedback loop was opened and the spectra obtained are the average over 132 spectra, each obtained over 132 different points separated by 3.1 nm in each of the regions. STM images were acquired with 100 pA and 800 mV tunnelling current and bias respectively.

2.5 HIGH RESOLUTION SURFACE SENSITIVE ELECTRON MICROSCOPY

2.5.1 *LEEM and PEEM*

Low-energy and photoemission electron microscopies are two microscopies which rely, just like transmission electron microscopy, on an electron optics imaging column composed of electromagnetic lenses and operating using high energy (typically 20 keV) electrons. PEEM relies on the extraction of photoelectrons from the sample, which is usually achieved with an ultraviolet source (laser, lamp or X-rays). LEEM relies on secondary or reflected electrons, created by a low-energy electron beam. This beam is shaped from electrons created by an electron source, accelerated to high energy electron beam inside an electron column, and decelerated before reaching the sample surface. In both techniques the low energy (0-100 eV, typically) of the electrons used for imaging ensures extreme surface sensitivity to a few topmost layers of the sample.

Since no actual contact occurs between the electron optics elements and the sample surface, both techniques are well suited for temperature-dependent studies, and, as long as the pressure remains reasonably low (typically below 10^{-7} mbar), they can be run in operando, i.e. during the evaporation of species onto the sample surface or in the presence of gases reacting at the sample surface. Thanks to the strong interaction between low-energy electrons and matter and due to the fact that PEEM and LEEM are full-field microscopies, high measurement rates are possible, typically from 1 to 100 Hz, which allows true real time monitoring of the growth on surfaces, as anticipated early on [129]. These studies are routinely performed with lateral resolution of about

10 nm. Recent developments, using aberration-corrected electron optics inspired by TEM instrumentation, allow the attainment of lateral resolutions of a few nm [130].

In PEEM, images reveal work function contrasts. In LEEM, the electron reflectivity is imaged, which is linked to the density of states and the sample structure perpendicular to the surface. As in a standard optical or transmission electron microscope, instead of observing the image plane, one can observe the Fourier plane. In LEEM, this allows the performance of LEED experiments (see next subsection), and micro-LEED experiments by using an aperture placed before the sample in order to select one region of the sample.

Figure 34 shows a schematic drawing of a typical LEEM instrument. Two key components that define LEEM and set it apart from conventional electron microscopes are the cathode objective lens and the magnetic beam separator. The magnetic beam separator is necessary to separate incoming, illuminating electrons from the back-reflected or emitted electrons used to form an image. The beam follows an inverted Y path, travelling in both directions between separator and objective. The basic energy away from the sample is 20 keV. The electron energy at the sample, E_0, is determined by the difference of gun potential and sample bias and can be tuned during the experiment in the range of about $E_0 = 0 - 100$ eV by simply changing sample bias.

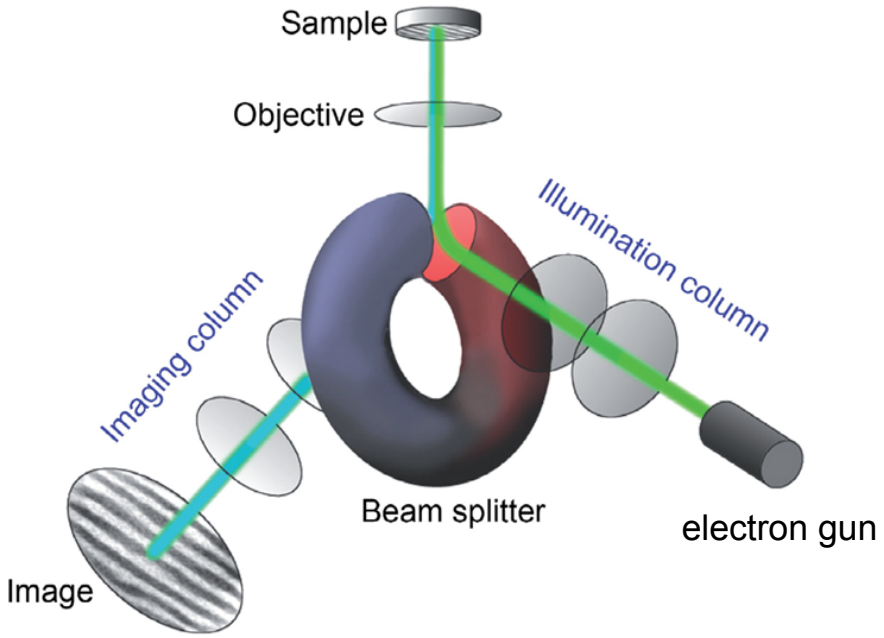

Figure 34: Schematics of a LEEM microscope. The electron beam passes through an illumination column, before being decelerated in the objective lens. Electrons finally hit the surface with normal incidence. Electrons that are backscattered elastically are collected in an imaging column and focused on a phosphorous screen, where a magnified image of the surface is obtained. The incoming and reflected electron beams are separated in a magnetic beam splitter using the Lorentz force. [131].

Low energy electron microscopy (LEEM) and micro-LEED measurements were performed at the Nanospectroscopy beamline at the ELETTRA synchrotron radiation light source in Trieste, Italy. The beamline operates spectroscopic photoemission and photoemission electron microscope (SPELEEM). This powerful instrument offers a wide range of complementary methods including low energy electron microscopy (LEEM)

providing structural, chemical and magnetic sensitivity. The lateral resolution of the microscope currently approaches few tens nm. The microscope is served by a high photon flux beamline, which can deliver elliptically polarized photons in the range 50 eV to 1000 eV. The setup also contains a UHV prechamber for preparing *in situ* the samples.

2.5.2 *Experimental setups*

The NanoESCA or X-ray PEEM has been installed on the platform Nanocharacterization CEA-LETI. We took part to a measurement campaign with Dr. Olivier Renault, who is in charge of the instrument. The microscope combines an electrostatic PEEM (OMICRON) with an aberration-corrected compensated double hemispherical analyser (Figure 35). As a source of photons, either a UV discharge lamp (Hg, 4.9 eV) or a focused X-ray source using an Al-K_α (1487 eV), can be employed. While the first source allows for work-function mapping and contrast of surfaces (4.9 eV is close to the work-function of most materials), the second source is suitable with X-ray photoemission spectroscopy, which can be made local by using an iris-aperture producing a 5 µm spots on the sample surface.

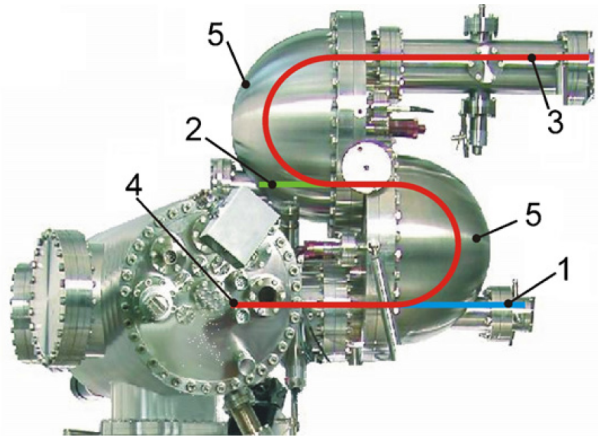

Figure 35: Photograph of the optical layout of the NanoESCA instrument. The optical path for the three working modes: direct non-energy filtered PEEM (1), small-spot spectroscopy with a channeltron detector (2) and energy filtered imaging (3) are indicated by the coloured lines. (4) sample position, (5) double hemispherical analyser. [131].

2.6 LEED AND RHEED

Low energy electron diffraction or LEED uses low-energy electrons (below 100 eV typically). Such electrons experience scattering events whereby they rapidly lose their energy, which makes the technique very sensitive to the few topmost layers of the sample. In the typical scattering geometry, LEED provides snapshots of in-plane cuts of the reciprocal space lattice of the topmost layer of the sample. Reflection high energy electron diffraction (RHEED) uses high-energy electrons (typically a few 10 keV). Such electrons penetrate matter much deeper than the low energy electrons used in LEED. In RHEED however, this extended penetration is avoided by the scattering geometry,

which corresponds to grazing incidence and exit. A RHEED image captures part of the scattering contribution which, due to the finite thickness of the sample (as seen by electrons), extends perpendicular to the surface. The aspect of the RHEED image is determined by the length-scale of the surface roughness as compared to the coherence length of the electron beam, which is typically of the order of 10 nm: electrons penetrate much deeper in samples with roughness length-scale well below this value, which yields spotty patterns, while in the opposite situation the sample is actually seen as two-dimensional which yields streaky patterns.

The analysis of electron diffraction diagrams can only be performed quantitatively in the rather complex framework of dynamical theory of diffraction explicitly taking into account multiple diffraction events. The location of the diffraction contributions in reciprocal space, which we will only address in this manuscript, are however little affected by multiple diffraction effects, which allows straightforward determination of the lattice parameter in the plane of the surface.

2.7 MULTI-PURPOSE UHV SYSTEM AT NÉEL INSTITUTE

The UHV system encompasses three chambers (Figure 36). A small chamber, reaching 10^{-7} mbar, is used as an introduction chamber for samples, STM tips, and metal targets, from or to atmosphere. Samples, STM tips, and metal targets are held on 1 inch molybdenum blocks (so-called molyblocks), which are transferred from one chamber to the other with the help of magnetic transfer rods.

One of the UHV chambers includes a large carousel for storing various molyblocks. In this chamber, an electron-beam sample heater allows to reach 1475 K (controlled with a pyrometer). The chamber is also equipped for Auger electron spectroscopy and ion bombardment (1-5 keV). It also includes a stainless tube connected to a leak valve which allows to leak in gases in front of the sample surface (see Figure 36), which is used for CVD of graphene and for high temperature O_2 cleaning of the samples.

A second UHV chamber is equipped with a radiation heated sample order with azimuthal rotation. Samples can be heated (up to 975 K typically) when exposed to molecular beams, produced in this chamber by either electron-beam evaporators or pulsed laser deposition. The latter is performed with a pulsed ((λ = 532 nm), it has a maximum energy per shot of 150 mJ) Nd:YAG laser entering the chamber through a specific view port and impinging a metal target held in one of the 8 slots of the metal target holder. The sample can be shone with a well-collimated electron beam with energy ranging from 10 to 50 keV, which allows for RHEED experiments. RHEED patterns are formed on a fluorescent screen facing the electron gun, and are collected with the help of a CCD camera.

A third chamber is equipped with a room temperature OMICRON-1 STM (see section above).

2.8 MOLECULAR BEAM EPITAXY OF RE THIN FILMS ON SAPPHIRE

The rhenium thin films (50 nm thickness) used to grow graphene (Chapter 5 of this thesis) have been prepared by Bruno Gilles and Benjamin Delsol at the SIMAP laboratory in Grenoble. They were grown by molecular beam epitaxy by evaporating Re from a

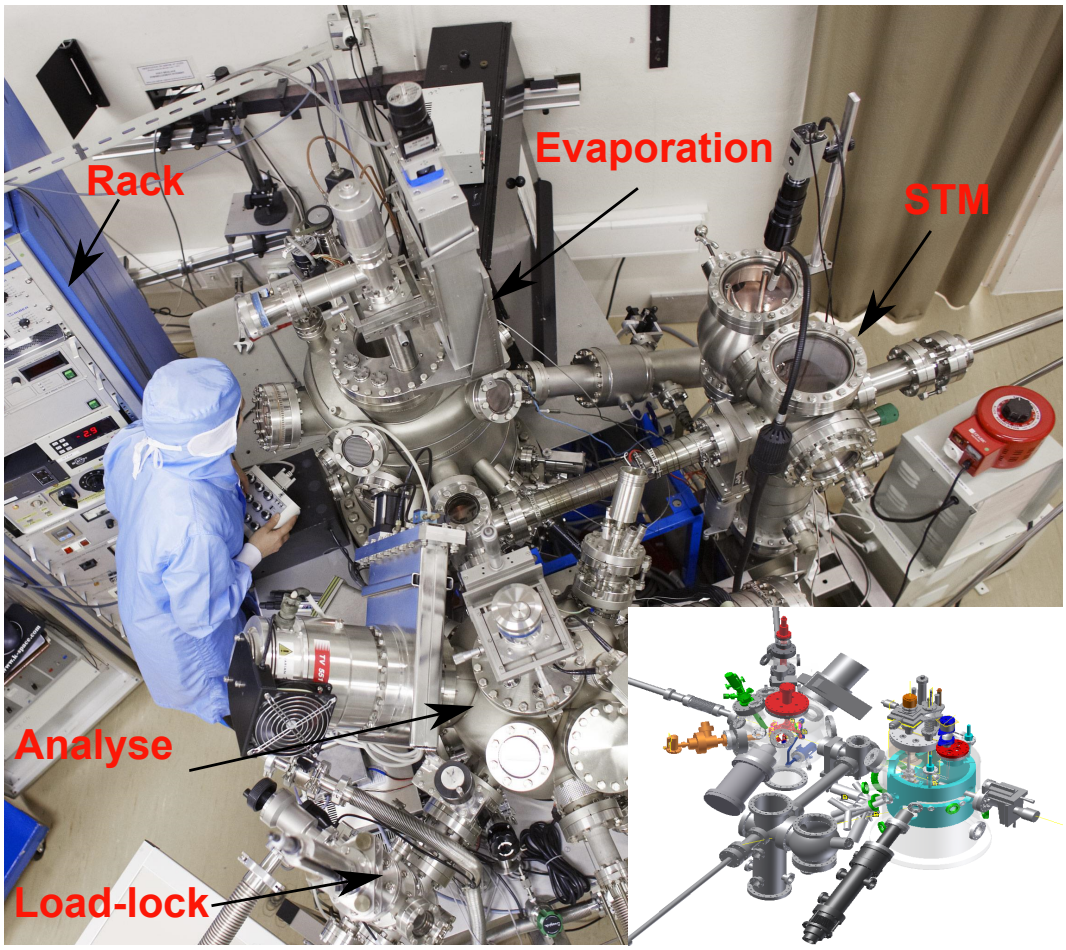

Figure 36: Experimental setup at Néel Institute with three main interconnected UHV chambers: evaporation, analyse and STM. Inset is a top-view illustration of this T-shape-like systems.

crucible heated by an electron beam, at a rate of 0.1 Å/s onto the hot surface (1040 K) of C-plane sapphire pieces of wafers.

Thanks to *in situ* RHEED, it was found that the epitaxial relationship between the rhenium and the sapphire is : $(0001)_{Al_2O_3} - (0001)_{Re}$ with $\langle 2\bar{1}\bar{1}0\rangle_{Al_2O_3} \parallel \langle 01\bar{1}0\rangle_{Re}$. In this configuration, all the metallic sites (Al and Re) coincide with a slight misfit of about - 0.47 % at room temperature.

After growth the samples taken out of UHV and rapidly put into a vacuum box in order to limit surface oxidation. They are then rapidly transported from SIMAP to Institut Néel were they are inserted in the UHV system.

2.9 PULSED LASER DEPOSITION FOR EPITAXIAL THIN IRIDIUM FILM

In this section, I describe the method which we have developed and optimized in 2009-2011 [15] for preparing high quality Ir(111) thin films. These films are then used to grow high quality graphene, which will be studied, after exposure to air, in chapter 3 of this thesis.

Iridium was grown by pulsed laser deposition at a rate of 1 Å/min on sapphire substrate $\alpha - Al_2O_3(0001)$. The surface preparation of sapphire consisted in a double outgassing at 1100 K under UHV during 50 min each one. The next step was the growth of 10 nm thickness of Ir at 800 K, followed by an annealing step at 1300 K for 30 min.

The very thin metal films do not dewet upon annealing, probably thanks to the small lattice mismatch between Ir(111) and sapphire and to the high melting temperature of Ir. The influence of the annealing step is obvious when comparing (Figure 37 a, b). For mild temperature, the film surface exhibits curved features, which are atomic step edges, as well as lines which are 120° rotated one with respect to the other. These are presumably the surface traces of grain boundaries.

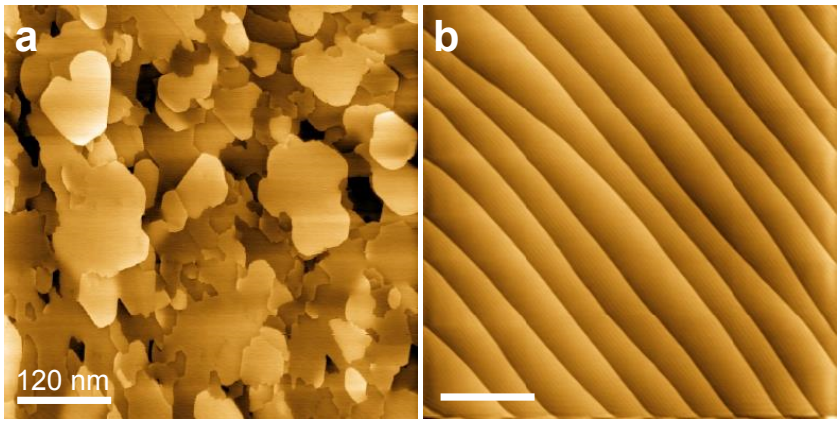

Figure 37: STM images of epitaxial Ir(111) film grown on sapphire substrate annealed at (a) 1000 K, (b) 1500 K.

The quality of the Ir(111) film was characterised by X-ray pole figures (Figure 38a). The threefold symmetry and Bragg diffraction angles proves that the Ir is (111)-textured and has a well-defined in-plane epitaxial relationship with sapphire, $\langle 11\bar{2}0\rangle_{sapphire} \parallel \langle 1\bar{2}1\rangle_{Ir}$, with a full-width at half maximum spread of 1° as derived from azimuthal angle scans. High-resolution transmission electron microscopy cross-sections of the sample, measured by Pascale Bayle-Guillemaud at CEA, confirm that a single orientation is obtained following the annealing step, and that the Ir(111) films have a single-crystalline surface (Figure 38) [15].

2.10 CHEMICAL VAPOUR DEPOSITION OF GRAPHENE ON IR(111)

The carbon precursor used for CVD graphene is ethylene (C_2H_4). Ethylene is leaked through a valve onto the sample heated to high temperatures, between 975 and 1475 K controlled by a pyrometer. In the UHV system installed at Institut Néel (see section 2.7), in which the samples studied in Chapter 3 were prepared, a dosing stainless-steel tube for ethylene, with 10 nm of diameter is placed in front of the hot sample surface Figure 39. The local pressure at the sample surface is estimated to a few 10 times more than the pressure measured with the help of the ion gauge placed away from the sample surface. CVD during 10 min and 10^{-8} mbar (measured with the ion gauge) above 1250 K ensured a graphene coverage in excess of 95 %. For experiments performed at the Nanospectroscopy beamline at ELETTRA, described in Chapter 4, no

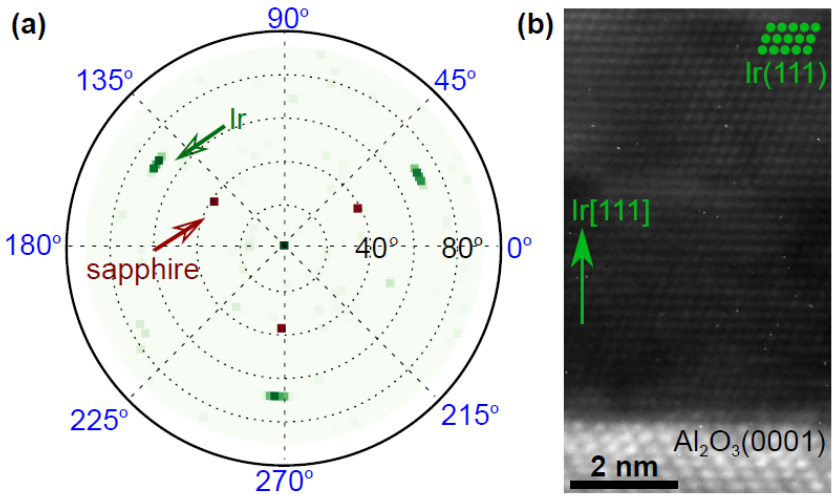

Figure 38: (a) X-ray pole figures (logarithm of the scattered intensity) for $(10\bar{1}4)$ planes of sapphire (red) and a (111) planes of Ir (10 nm thick, grown at 700 K and annealed at 1100 K, green) on the same spherical coordinate system (azimuthal and scattering angles displayed in grey and black, respectively). The Ir Bragg peaks are broader than the sapphire ones, indicative of some spread in the epitaxial relationship. (b) TEM cross sections of a 9 nm Ir film on sapphire, along the $[1\bar{1}1]$ azimuth. Green dots highlight the crystallographic structure of Ir.

dosing tube was available and ethylene was simply backfilled in the UHV chamber with a 5×10^{-8} mbar partial pressure. Compared to the case with a dosing tube, the local pressure on the sample was then lower and the growth rate accordingly smaller.

The single crystallographic orientation, corresponding to the typical graphene/Ir(111) moiré is found at 1400 K. This orientation is $\langle 1\bar{1}00\rangle_C \parallel \langle 1\bar{2}1\rangle_{Ir}$, as shown by RHEED (Figure 67). Graphene rods are only found along the $[1\bar{1}0]$ azimuth of Ir(111). In this orientation, also superstructure rods from the moiré are observed. The distances from the Ir, graphene, and moiré streaks to the central one give an estimate for the in-plane lattice parameters of graphene and the moiré, 0.246 ± 0.001 nm and 2.634 ± 0.014 nm, respectively.

The uniform layer of graphene of high quality replicates the atomic smoothness of Ir(111) buffer layer by extending coherently across its atomic steps (Figure 41). STM topographs display the typical wrinkles and Ir step edge reshaping.

The moiré pattern is obtained with different tunnelling parameters. Figure 42(a) was imaged with a positive tunnelling voltage (0.93 V) while a negative voltage (-0.08 V) was chosen for Figure 42(b). The moiré structure is highly ordered meaning that also the graphene layer must be highly ordered (defects would strongly modify the aspect of the moiré structure [14]). The moiré is imaged in two different ways, in part (a), the atop regions appear as dark depressions in a bright surrounding. In part (b), the moiré contrast is inverted. Now the atop regions are imaged as bright protrusions in a dark surrounding. Such a contrast inversion is reversible without any sign of a tip change and has been reported as well in graphene grown on bulk Ir(111) single-crystals [40].

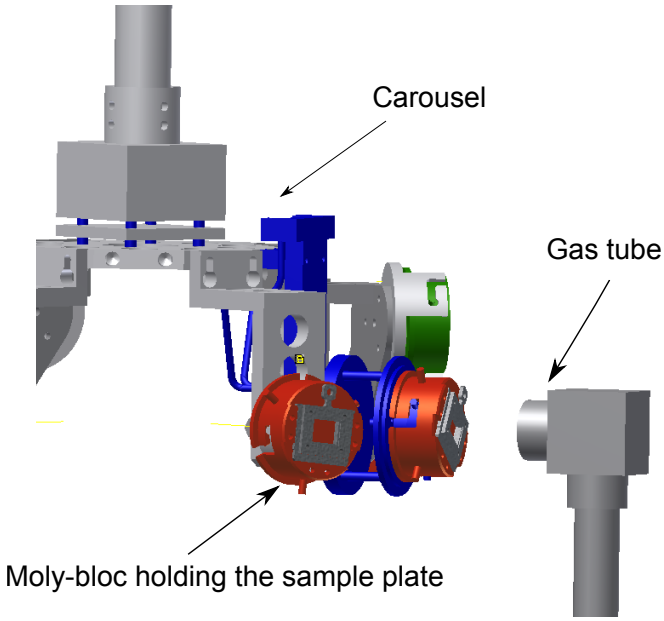

Figure 39: The position of the gas tube and the sample mounted on the oven during CVD process, the position of sample and oven can be changed.

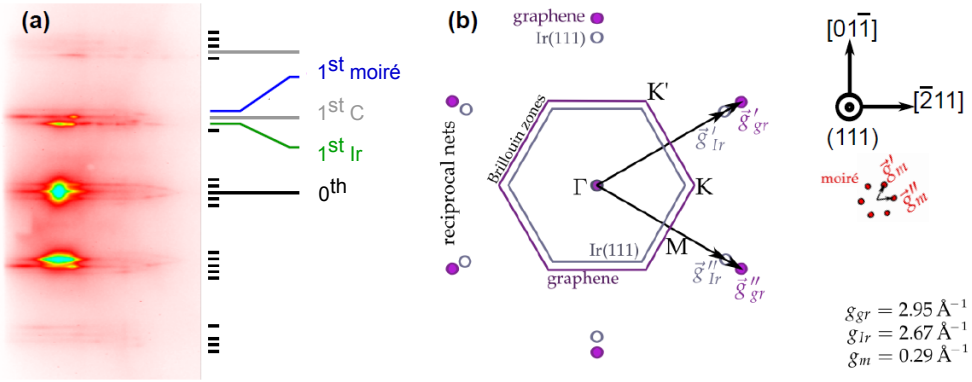

Figure 40: Single graphene layer on the Ir (111) film in epitaxial relationship $\langle 11\bar{2}0\rangle_C \parallel \langle 1\bar{2}1\rangle_{Ir}$ In reciprocal space. (a) RHEED pattern of graphene/Ir(111) (10keV, $\langle 1\bar{1}0\rangle$). First order Ir, graphene, moiré streaks are highlighted as well as the zeroth order streak and one second order moiré streak. (b) Brillouin zones of Ir(111) and graphene together with the moiré superstructure.

2.11 SURFACE PREPARATION OF BULK SINGLE CRYSLALS

Samples were grown *in situ* in ultra-high vacuum conditions (base pressure 5×10^{-11} mbar). An Ir(111) single crystal was used as a substrate and cleaned with repeated cycles of Ar ion sputtering and high temperature (1200 °C) flashes under oxygen (10^{-8} mbar). A last temperature flash (1200 °C) is finally done under UHV conditions to remove the oxide layer. High-quality graphene was grown by exposing the Ir(111) surface to 5×10^{-8} mbar of C_2H_4 at 1000°C. The Re single crystal has been prepared in the same way as Ir one. While the growth of graphene is described in chapter 6.

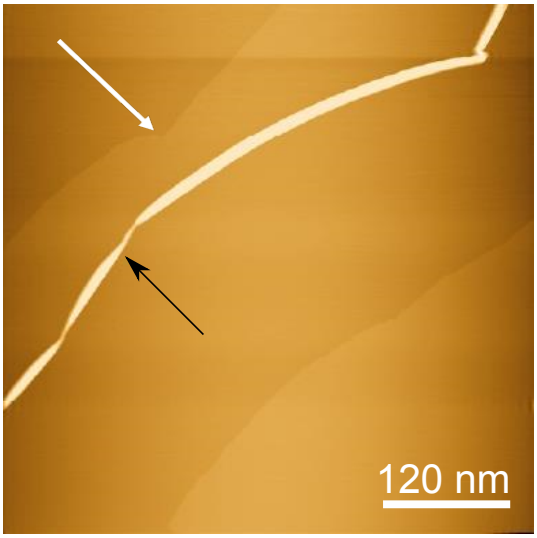

Figure 41: STM topographs showing graphene wrinkles (black arrow) as well as reshaping of underneath Ir step edges of graphene/Ir(111) (white arrow) (grown at 1400 K).

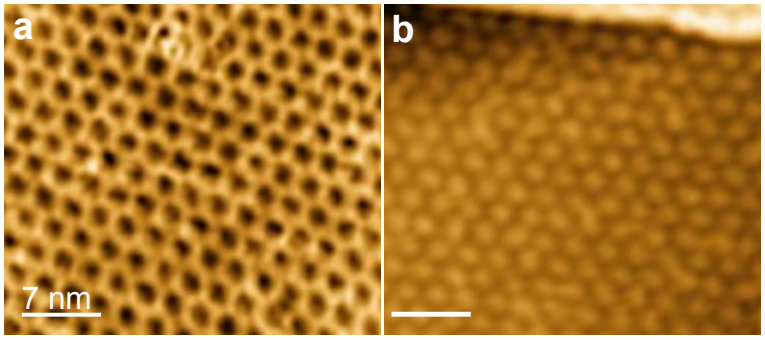

Figure 42: STM topographs of the moiré (a) V_t = 0.93 V, I= 1.08 nA, (b) V_t = - 0.08 V, I = 0.6 nA. A contrast inversion occurs, depending on the tunnelling parameters. On the left, the atop regions appear as dark features in a bright milieu, on the right, they appear bright in a dark milieu.

3

SPONTANEOUS ATMOSPHERIC PRESSURE INTERCALATION OF AN OXIDE IN A WEAKLY BONDED SYSTEM, GRAPHENE ON IR(111)

In this chapter, I will present the formation, the structure, and the electronic and vibrational properties of graphene decoupled from an Ir(111) substrate by ultrathin iridium oxide ribbons. This study was initiated by the observation of markedly different surface morphologies of samples characterized by STM under UHV, *in situ*, in the same environment where the samples were grown, and *ex situ*, by AFM and STM after exposure to air. In this study we combined complementary *ex situ* probes, AFM, STM, STS, μ-Raman spectroscopy, X-ray photoemission microscopy and X-ray photoelectron spectroscopy, to achieve a comprehensive characterization of the system.

We found that interaction of oxygen with epitaxial graphene on iridium leads to the formation of an ultrathin oxide layer upon air exposure, extending between graphene and the metallic substrate via the graphene wrinkles, which act as efficient diffusion channels for oxygen. Graphene on Ir(111) was chosen as a platform for this study for two reasons: (i) it is a high quality system, in which the density of defects such as grain boundaries can be lowered to such a point that their role in intercalation can be ruled out; (ii) it is a weakly bonded system, for which intercalation is thus easier expected than in strongly bonded systems like graphene/Ru(0001), and for which wrinkles, whose role in intercalation has not been addressed so far, form.

Our findings open the way to the transfer-free preparation of graphene decoupled from its metallic substrate, and to the modulation of graphene's properties with the help of localized intercalation.

3.1 INTRODUCTION

Change of paradigms, in terms of new functionalities, architectures, and performances, are foreseen with graphene. These prospects are urging the development of efficient production methods [132]. Preparation by chemical vapor deposition (CVD), in this respect, has reached such maturity that graphene now appears as an alternative to indium tin oxide as a transparent conductive electrode [1] or to Si and III-V semiconductors in high-frequency electronics [133]. Intercalation of species between the metallic substrate needed for CVD and graphene, a method known since the 1980's [8], is an efficient and versatile way to achieve quasi freestanding graphene [104] and to engineer the properties of graphene, for instance to induce electronic bandgaps [134], magnetic moments [135], and strains [136]. Dual intercalation, of Si and O, even showed great promise for the transfer-free preparation of graphene-on-oxide field effect transistors [106].

Despite the numerous reports devoted to graphene/substrate intercalated systems, two key questions remain open. First, the surmised role of defects as pathways for intercalation has only been established, yet partially in some cases, for a few defects, namely graphene free edges [104] and point defects [137, 13]. Unveiling other interca-

lation pathways will help better envisioning the full potentialities of intercalation for building up advanced graphene-based hybrids. Second, all studies of intercalation reported thus far were performed under ultra-high vacuum (UHV). While this approach offers optimum control over the processes, it is a prohibitively costly one in the view of the production of graphene decoupled from its substrate. While atmospheric pressure intercalation would be desirable, intercalation may proceed differently due to the markedly different conditions.

In this framework, the present study consists in decoupling graphene from its metallic substrate. For this, we address two questions, by studying high quality graphene prepared by CVD on Ir(111) thin films. Iridium is one of those transition metals, like Cu, Pt, and Au, that weakly interact with graphene [9]. Unlike on the latter three metals however, most defects and notably grain boundaries can be avoided on Ir(111) [138, 139], so that their role in intercalation [137] can be ruled out. Correlating complementary microscopic analysis, we show that exposure to air leads to the formation of an ultrathin intercalated oxide modifying the weak graphene-Ir interaction and generating variations of the charge density in graphene. We find that a common kind of defect, local delaminations of graphene from its substrate, so-called wrinkles, forming during cool down to room temperature after CVD due to the mismatch of thermal expansion coefficient of graphene and its substrate, are pathways for a slow intercalation of oxygen species.

3.2 OXIDATION OF IRIDIUM ON GRAPHENE-FREE AND GRAPHENE-COVERED REGIONS

Samples studied in this chapter consist of graphene grown by CVD on top of Ir(111) thin films prepared on sapphire (see Section 2.9 and 2.10). Under UHV, prior to exposure to air the graphene-covered regions of the sample exhibit a typical flat topography, except for wrinkles and a periodic corrugation associated with the graphene/Ir(111) moiré [9] (Figure 43).

Figure 43 shows STM images of graphene on Ir taken under UHV, in the same system where the sample was grown. The left image reveals a wrinkle (bright linear protrusion) ending at a graphene edge (inclined line, the bottom right of the image is graphene-free). The right image is a smaller scale one revealing the triangular moiré between graphene and Ir(111).

The situation is markedly different after exposure to air, as shown by atomic force microscopy (AFM). Inspecting phase contrast AFM images (Figure 44) allows one to identify graphene-free and graphene-covered regions [140]. AFM phase imaging distinguishes regions with and without graphene, due to sensitivity to the mechanical response of the technique. Similar observations were performed for graphene on SiC [141].

Figure 45a reveals that (i) graphene-free regions (named A hereafter) protrude out of the surface, (ii) around graphene edges and along wrinkles, flat ribbons (named B hereafter) whose height is substantially larger (see below) than the Ir atomic step edges, are found. The moiré observed with scanning tunneling microscopy (STM) under UHV before air exposure is no more visible with STM [142]. While the height (typically 3 nm in average, relative to graphene) of type A-regions does not evolve with time, the height of type B-regions, as well as their lateral expansion, does (Figure 45a,b). After

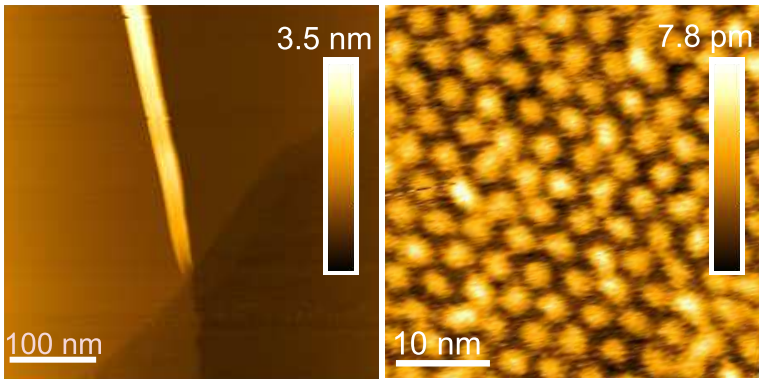

Figure 43: STM topographs under UHV of as-grown graphene on Ir(111) before exposure to air. Tunnel current: 1.7 nA (left) and 30 nA (right); bias voltage: 1.2 V (left) and 500 mV (right).

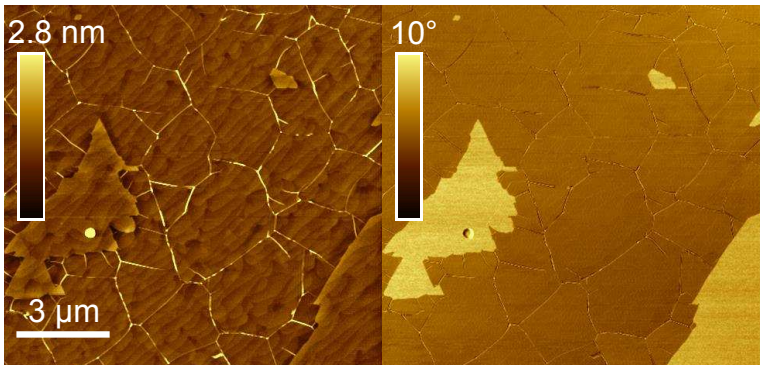

Figure 44: AFM image taken with tapping mode, showing the topography (left) of graphene/Ir with partial coverage, after exposure to air. Corresponding phase map (right) of the same region, the contrast phase allows one to readily identify graphene-free (lighter) and graphene-covered (darker) regions.

a few days the height and width of type B-regions do not increase much and reaches about 1.5 nm and a few 100 nm respectively. The surface of graphene appears rougher on type-B regions than on other graphene regions (Figure 45d). What is the nature of the height variations upon exposure to air ? Volume expansion of surfaces due to their oxidation is a well-known effect in AFM [143]. The presence of type A-regions is interpreted in this light: in the absence of a protecting layer hindering surface air oxidation, an Ir oxide rapidly forms [144, 145].

3.2.1 *Graphene on an ultrathin IrO_2 layer on Ir*

Figure 46a shows an AFM topograph acquired in air of the Ir(111) surface covered with graphene, at the location where three graphene wrinkles intersect. The inset in Figure 46a shows atomic resolution STM in air of the surface, which reveals the honeycomb lattice of graphene. Besides atomic step edges (0.22 nm high) from Ir(111) and small dots which are dusts presumably resulting from ambient condition exposure, terraces which are higher than the remaining of the surface (except for the wrinkles) are observed exclusively around the wrinkles. These terraces are typically 0.6 ± 0.1

nm high and exhibit linear patterns of a few nanometres periodicity (only revealed in AFM with the help of super-sharp tips, Figure 46b). Below we provide evidence that the whole surface in (Figure 46a,b) is covered with graphene. Most of the patterns (e.g. top of Figure 46b) have a 4.1 nm periodicity, some have a larger periodicity (e.g. 6.3 nm as in the bottom of Figure 46b). Such patterns cannot be interpreted as moirés between graphene and Ir(111), which have triangular lattices with 2.5 nm period.

Superimposing ball-models of the lattices of graphene and of a rutile $IrO_2(100)$ surface, with $\langle 1\bar{1}00\rangle$ directions in graphene and $\langle 010\rangle$ directions in $IrO_2(100)$ aligned to $\langle 112\rangle$ directions of Ir, yields a moiré pattern which perfectly matches the AFM observation (Figure 46c). These orientations are those expected for the most stable orientation variant in graphene/Ir(111) and that observed for IrO_2 on Ir(111) by surface X-ray diffraction under UHV [145] respectively. The step height of the oxidized regions ($\sim$ 0.6 nm) corresponds to four Ir planes. Oxygen termination is thermodynamically preferred for bare $IrO_2(100)$ [145].

The larger periodicity patterns (e.g. 6.3 nm) cannot be interpreted without invoking strain in either graphene and/or the intercalated oxide and other iridium oxide phases (other than those discussed in [145], none of which is compatible with our AFM observation). Strains of the order of a percent could account for the observed large periodicities. Note that we do not expect isotropic strain in the oxide or graphene, due to the presence of the wrinkles, and due to the different symmetries of the Ir(111) and iridium oxide, respectively.

The IrO_2 terraces forming between graphene and Ir(111) are all found along the graphene wrinkles. This suggests that wrinkles are diffusion channels for oxygen molecules and that they accordingly become oxygen reservoirs for the oxidation of the topmost Ir(111) layers. IrO_2 regions develop up to several microns away from the entrance of the diffusion channel, which is, as we shall see later, located at the edges of graphene domains. The formation of these intercalated regions, named type B-regions, is interpreted as the result of the reactive intercalation of oxygen between graphene and Ir(111).

3.2.2 *Low conductivity of iridium oxide*

The oxide type A-regions has a low conductivity, compared to the rest of the sample (Figure 47). Figure 47 shows STM and AFM images recorded with the same tip at room temperature at the same location. The comparison reveals that the graphene-free regions, which are capped with an oxide after exposure to air and protrude out of the surface as seen in AFM, are less conductive (seen as depressions in STM) than graphene covered regions. Note that the intercalated oxide ribbon are not easily observed in STM. This is due to the fact that although higher, they have a lower conductivity for the bias voltage used here, which yields an apparent height not much different from regions which are not intercalated.

3.3 SURFACE ELECTRONICS AND ELEMENTAL COMPOSITION

In order to confirm our interpretations, we performed spatially-resolved measurements of the work-function (WF) [146]. PEEM spectroscopic images at the photoemission

threshold exhibit a contrast inversion as a function of the secondary electron energy, indicative of a strong WF contrast across the surface (Figure 48a and Figure 49). WF maps reveal two kinds of regions (Figure 48b,c): one with a 4-4.1 eV WF, the other with a mean 4.5 eV WF and variations of approximately 0.1 eV about this values across micrometer distances. The first value is close to the 4.2 eV one reported for IrO_2 [144], and thus presumably corresponds to type A-regions in Figure 45. The second value is similar to that reported for graphene/Ir(111) [147] and thus signals graphene-covered regions, the spatial fluctuations in their WF seemingly corresponding to surface inhomogeneities, with length-scale compatible with the distance between intercalated (type B) ribbons.

The picture sketched above is further supported by chemical analysis of the regions with different WF, thanks to area-selected X-ray photoemission performed with the same PEEM set-up operated in the micro-spectroscopic mode [146]. We find that the intensity ratio between C 1s and Ir 4d peaks (Figure 48d,f) is 12 % in the high WF regions, and about twice as low on regions with prominently low WF. We note that due to the size of the iris aperture for area selection (sketched in Figure 48a), low WF regions also comprise a contribution ($\sim$ 30% here) of high WF regions. We deduce that low WF regions are graphene-free. An O 1s peak is detected in all regions (Figure 48e,g). Though the statistics of our measurement does not allow to map out spatial inhomogeneities of this species, combining the information, gained from the WF and chemical analysis, we can conclude that low WF regions are graphene-free, type A-regions (IrO_2), and that high WF regions are graphene-covered and comprise oxygen species. The latter are inhomogeneously distributed over the surface, type B-regions (oxide ribbons intercalated along wrinkles), and possibly also, between these regions, a disordered layer of small oxygen-containing molecules (e.g. water, dioxygen) intercalated below graphene.

A series of PEEM images have been recorded across the photoemission threshold (energy step: 0.02 eV from 3.7 to 5.2 eV electron energy), some of which are shown in Figure 49, to determine the local work function [148]. A work function map, leading to such figures as Figure 48b, is generated from the image series by a fit, performed on the pixel-to-pixel secondary electron spectra, of the low-energy cut-off equivalent to the work function (see [149] and references therein).

At this point we summarize (Figure 48e) the effect of exposure to atmospheric environment at room temperature. Without holes in the graphene sheet, no oxidation of the Ir surface occurs. Graphene-free regions are rapidly oxidized, on a time scale below 1 h. Graphene-covered regions are also oxidized, but on a much larger timescale, upon the slow intercalation of oxygen species at graphene edges entering wrinkles at their free end, which act as a tunnel for the transport of species across at least few micrometer distances [150]. We note that the intercalation does not occur in case of high quality graphene fully covering the Ir(111) surface (as also noticed in Ref [105]), i.e. when wrinkles do not have an open end.

3.4 CHANGE OF THE PROPERTIES OF GRAPHENE UPON OXIDE INTERCALATION

In the remaining we focus on the type B-regions, more precisely on the influence of the intercalated oxide on the properties of graphene. Spatially-resolved Raman scattering measurements were performed at the exact location where AFM (Figure 50a) was also

performed. No defect-allowed D mode is observed (Figure 50b and Figure 51), which confirms the uniform high quality of the graphene-covered regions. In the vicinity of the wrinkles, graphene's G and 2D modes are found at 1594 ± 3 and 2691 ± 3 cm^{-1} respectively; they are located at 1588 ± 3 and 2679 ± 3 cm^{-1} far from the wrinkles (Figure 50b). Though the G and 2D mode red-shifts, about 6 and 10 cm^{-1}, correlate with the position of the wrinkles (Figure 50c and Figure 51), they are actually not a direct manifestation of graphene's deformation or decoupling from its support in the wrinkles. The G and 2D modes indeed have single-lorentzian profiles, in other words, they do not comprise two spectral components, which would each arise from "flat" and wrinkled graphene. A significant contribution from the wrinkles is actually not expected, given that the number of the atoms which they encompass is typically 100 times smaller than that illuminated by the laser spot (300 nm diameter). The observed red-shifts are thus ascribed to the presence of the intercalated oxide ribbon. Strain and changes in electronic density can both be invoked in principle to explain G and 2D mode shifts. Rough estimates based on reports addressing specifically each effect yield order of magnitudes, 0.1 % and $10^{12} cm^{-2}$ for strains [121] and electronic density change [120] respectively. The former could result from the stretching of graphene upon intercalation [136]; the latter could be associated with variations of the charge density in graphene set by the variation of the distance between graphene and the metal substrate due to the presence of the intercalated oxide [142].

The position of the 2D and G peaks (Figure 51a,d) strongly varies in a way closely related to the position of the oxide ribbon intercalated between graphene and Ir(111). The area below those peaks (Figure 51b,e) also exhibits noticeable variations, which are ascribed to local fluctuations of charge transfers. The variations of area below the 2D band (Figure 51b) seem to correlate with the position of the wrinkles, which we interpret as the manifestation of a change in the graphene-support interaction at the wrinkles (expected weaker due to the larger graphene-support distance). No measurable intensity below noise level is observed in the wavenumber region where one expects a D band (Figure 51c).

Scanning tunneling spectroscopy was employed to test which effect (strain or charge transfer) actually prevails. The local density of state (LDOS, which is proportional to the local conductance measured with the STM tip) is markedly different on graphene regions with and without an intercalated oxide ribbon (Figure 50d). Concluding from the shape of the LDOS whether the graphene/support interaction is stronger or weaker is in our opinion daring, given the different shapes reported by different groups on identical graphene systems [151, 152]. We shall only mention that the graphene/Ir interaction, which is known to be weak [9] can reasonably be expected to be even weaker in the presence of an interaction oxide, as is the case in graphene/Ru(0001) [106]. Assuming that the LDOS minimum tracks the neutrality point in graphene [153, 154], we first observe that the Dirac point for graphene on Ir(111) is located closer to zero than in *in situ* UHV experiment [9]. The difference is ascribed to a transfer of electrons from below and above graphene. The latter may include the effect of adsorbates on graphene. The former includes the effect of a disordered layer of molecules possibly intercalated between graphene and Ir, the presence of which would explain both the occurrence of a strong Raman signal absent in as-grown graphene/Ir(111) [155], and the absence of the moiré pattern. Changes in the position of the Dirac point, of a few 100 meV, are observed between graphene with and without an oxide below it. This

translates into variations of charge densities of the order of $10^{12} cm^{-2}$, which account for the observed Raman shift changes. We deduce that the latter originate prominently from charge density effects induced by intercalation [150].

3.5 CHANGE OF GRAPHENE'S MECHANICAL PROPERTIES DUE TO INTERCALATION OF AN OXIDE

Significant phase difference is observed between graphene flake and Ir metal (Figure 52) reflecting the difference in surface properties [156]. In contrast, the same phase on graphene surface shows a contrast, which indicate that AFM tip is interacting with the same surface. The phase shifts are observed for regions along wrinkles in which some molecules trapped between graphene and iridium. This particular feature observed in the phase image is the formation of an oxide Ir embedded in the graphene flake which revealed that a trapped adsorbate piled up at the edges or along wrinkles.

Several contributions have investigated the potential of phase imaging to detect variations in materials properties such as adhesion, elasticity in addition to topographic information [157]. Topography phase imaging records the phase shift ($\Delta\varphi$) and the amplitude (A) of the cantilever's periodic oscillations relative to the cantilever drive signal. The $\Delta\varphi$ is a result of the energy dissipation that occurs when the probe makes contact to the sample. This latter is directly related to the changes in mechanical (a convolution of adhesion, composition, friction and viscoelasticity) and electrical properties. However, still we could not understand the origin of the contrast in phase imaging related to dissipative processes at the tip-surface interface and how to interpret height and phase contrast images in terms of the sample properties.

3.6 CONCLUSION

In conclusion, we discovered that wrinkles play a central role in the diffusion of oxygen species in between graphene and its Ir(111) substrate under atmospheric conditions, by letting species penetrating below graphene from their open end. These diffusing species react with Ir and slowly form oxide ribbons, the thickness of which reaches 1.5 nm, expanding across a self-limited width of a few 100 nm. The effect was also observed recently in our laboratory on another related system, graphene on Cu foils, and is thus of general importance in CVD-produced graphene. We found strong evidence that the intercalation of the oxide ribbons yields modulation of few $10^{12} cm^{-2}$ of the charge density in graphene and strongly modifies the graphene-support interaction. Same effect has been demonstrated to occur in the case of carbon monoxide CO intercalated in between graphene and Pt foils for developing a new transfer strategy which is free from etching metal substrates and therefore without contaminants [158]. Their study shows that moreover its island boundary, the graphene wrinkle may serve also as another initial place for CO intercalation.

Our findings highlight a cheap and easy way of intercalating thin oxides between graphene and its substrate, and on the contrary, the crucial need for eliminating holes in graphene on metals with which it weakly interacts, in the view of any application taking benefit of graphene as a barrier coating to oxidation. More advanced structures, with in-plane variations of the nature of the intercalants across 100 nm distances, could

be designed by further processing. This opens the way to the bottom-up fabrication of high quality charge-modulated graphene, for instance in the view of smart devices exploiting the principles of optics for guiding charge carriers ([159, 160]).

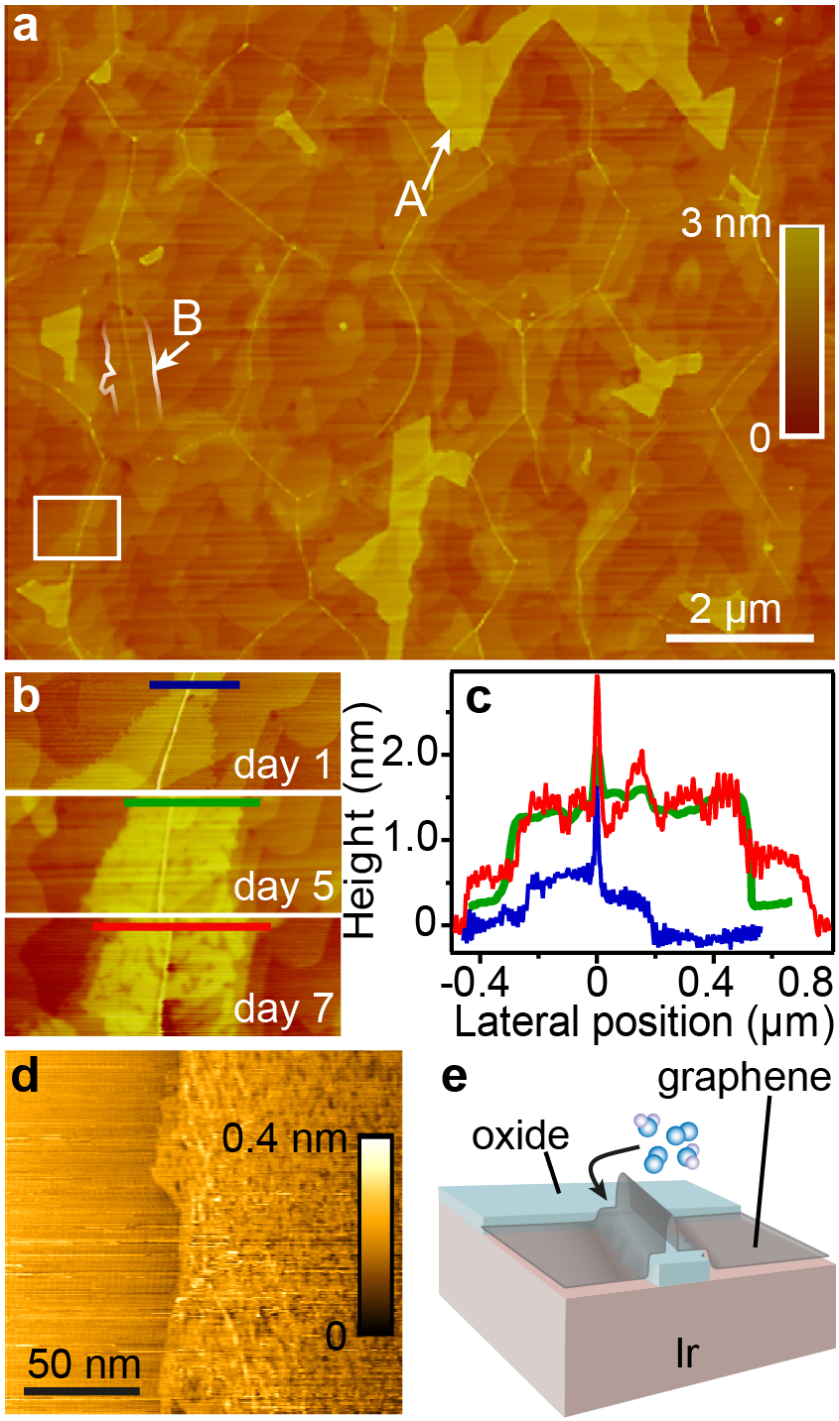

Figure 45: a) AFM image of graphene/Ir(111) after exposure to air, exhibiting Ir oxide on graphene-free regions (labeled "A") and intercalated between graphene and Ir, in the form of ribbons along the wrinkles in graphene (labeled "B"). b) Close-up of the region framed in a), as a function of time. c) Height profiles along the lines marked in b). (o) marks the position of the wrinkle. d) STM topograph of a graphene-covered region comprising a type-B region (right part). e) Cartoon summarizing the effect of atmospheric molecules (sketched with balls) which intercalated between graphene and its substrate (Ir) at the open end of a wrinkle. Image taken with tapping mode, showing the topography of graphene/Ir with partial coverage.

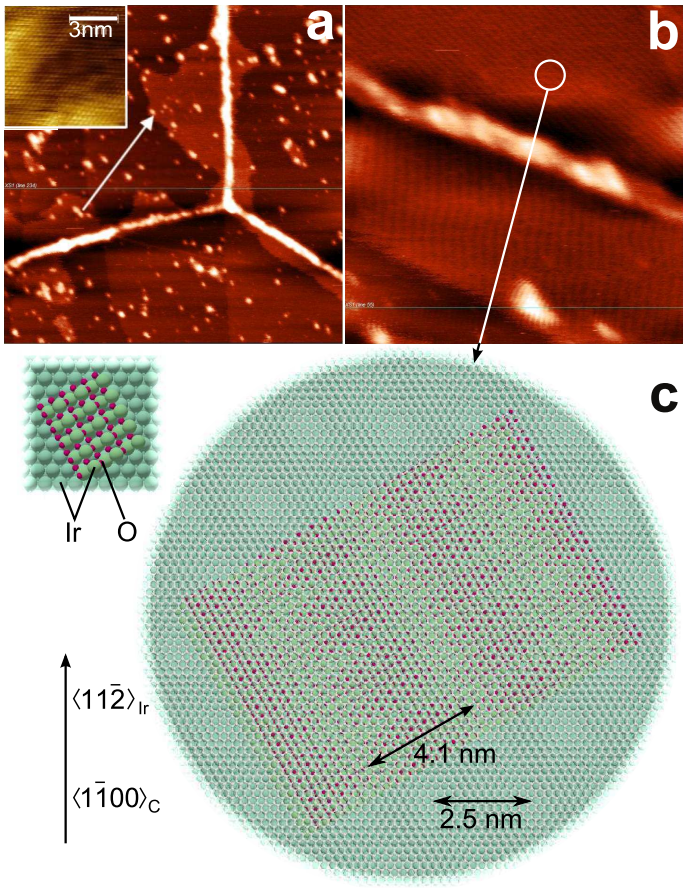

Figure 46: a) AFM topograph of graphene showing three wrinkles, and revealing substrate step edges of the Ir substrate (black arrows) and of IrO_2 (white arrows) underneath graphene. The inset shows an atomic resolution STM topograph of graphene on Ir, performed after air exposure. b) High resolution AFM topograph of two graphene/IrO_2/Ir regions at the sides of a wrinkle, displaying linear periodic patterns with two distinct periodicities. c) ball model of graphene/IrO_2/Ir exhibiting a 4.1 nm moiré pattern.

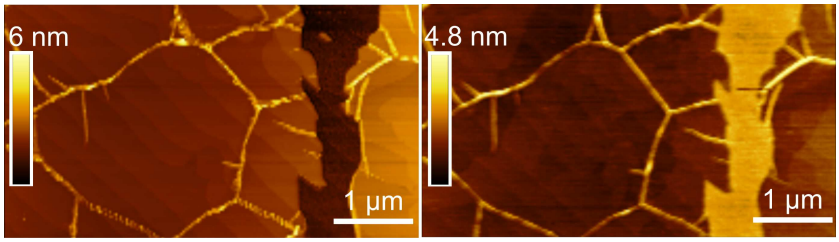

Figure 47: STM topograph (left) of graphene on Ir(111) after exposure to air (tunnel current: 100 pA, bias voltage: 200 mV). AFM topograph (right) measured with the same tip of the same region, in frequency modulation mode (collaboration with C. Winkelmann at Néel Institute).

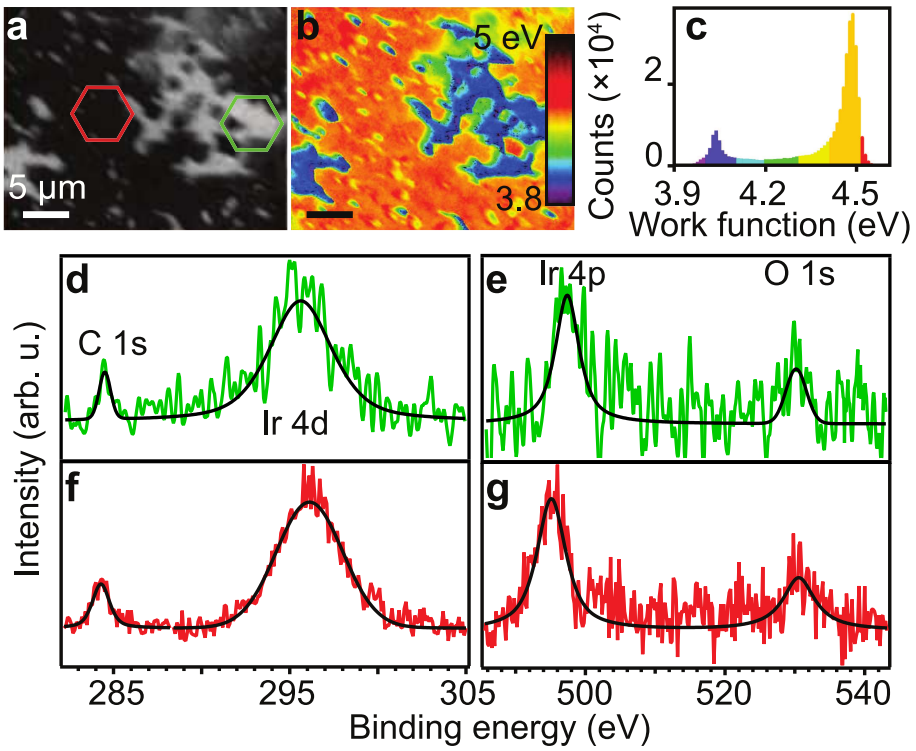

Figure 48: Surface electronics and elemental composition. a) UV-excited PEEM spectroscopic image (4.4 eV secondary electrons) of a surface area comprising graphene-free (type A-regions) and graphene-covered regions, including type B-regions (oxide ribbon intercalated below graphene). b, Corresponding WF mapping of the region in a). c) WF distribution of b). d-g) Background-subtracted XPS micro-spectra of Ir, C, and O core levels over two areas of interest marked in a) (coloured spectra are data obtained from the hexagonal frames of the same colour; black curves are fits to the data).

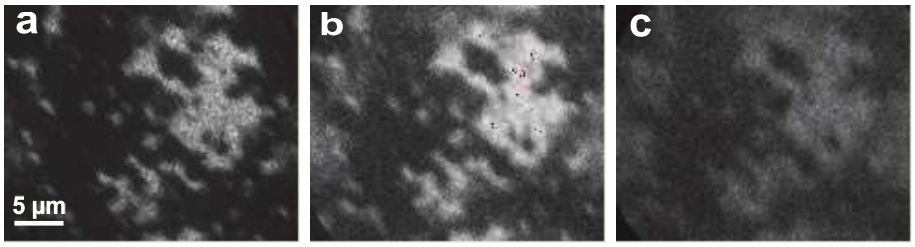

Figure 49: Series of PEEM images of graphene on Ir(111) after exposure to air recorded at a; 4.4, b; 4.6, and c; 4.8 eV photoelectron energy. Note the contrast inversion.

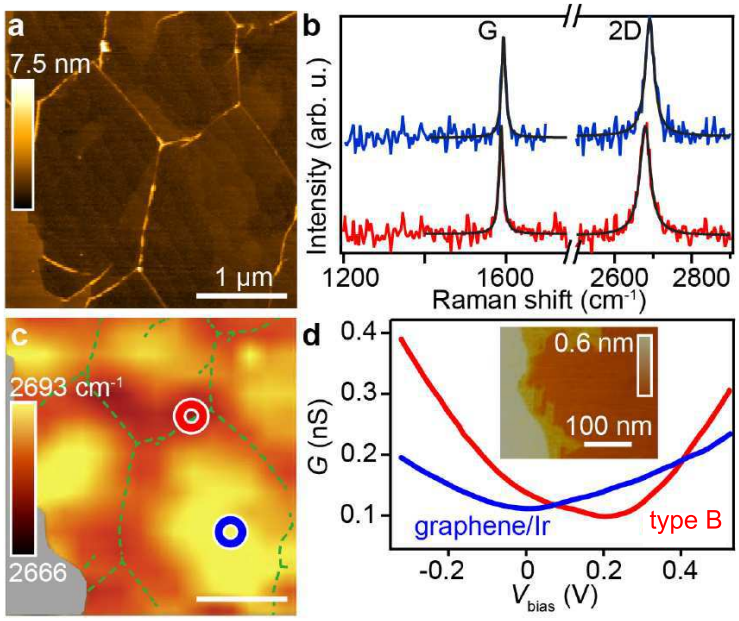

Figure 50: Change of the properties of graphene upon oxide intercalation. a) AFM image of graphene/Ir. b) Raman spectra acquired on the two spots marked in c. c) Map of the position of graphene's 2D band Raman shift, in the same area as a). The grey region is graphene-free, doted lines are guides for the eyes showing the position of the wrinkles apparent in a). d) Local conductance (G) as a function of tip-sample bias (V_{bias}) averaged on the left region (red, type-A) region, and on the right (blue, graphene on Ir(111) without intercalated ribbon) of the STM image shown in inset.

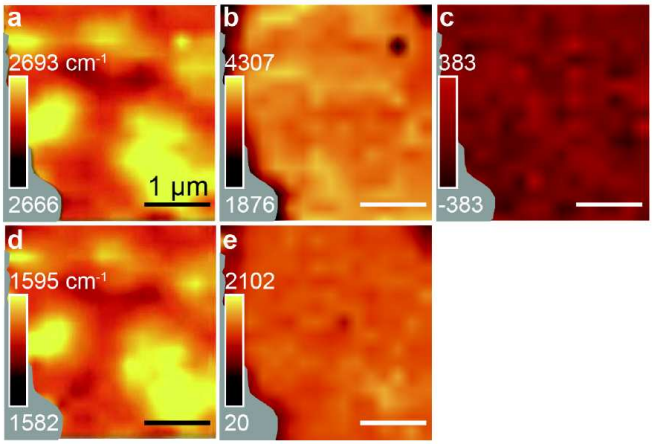

Figure 51: Maps of the a) the position of the 2D band, b) the area below the 2D band, c) the fluctuations of area around zero in a region expected for the D band, d) the position of the G band, and e) the area below the G band, of Raman spectra. The maps were extracted from the same area as in Figure 3b of the main text. The labels in the colour bars of b), c), and e) have been normalized one with respect to the other, which allows a comparison between the various areas.

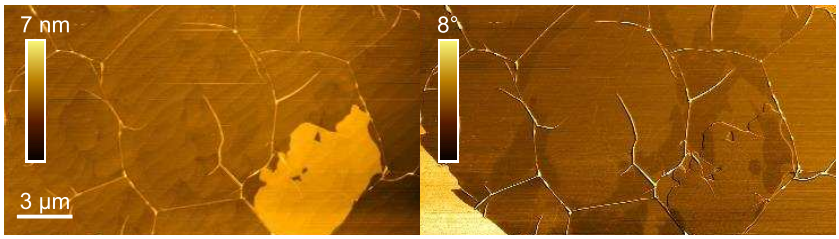

Figure 52: (left) topoography and (right) phase AFM image of graphene/Ir with partial coverage showing an intercalated region in between graphene and iridium.

4

COBALT INTERCALATION AT THE GRAPHENE/IRIDIUM INTERFACE: INFLUENCE OF ROTATIONAL DOMAINS, WRINKLES AND SUBSTRATE ATOMIC STEPS

In this chapter I will describe the intercalation of the equivalent of one atomic layer or less of Co between graphene and Ir(111). Compared to the previous study, both the nature of the intercalant and the pressure conditions are changed, here UHV. Our initial motivation was to better understand the preparation of graphene/ferromagnet/substrate hybrid systems, which have been studied in the recent years by different groups [161, 13, 108, 109, 162], including ours. In these systems, all prepared by intercalation of a ferromagnet, magnetic moments were found in graphene [163], surprisingly strong magnetic anisotropy perpendicular to the surface in ultrathin Co films with a graphene topmost interface were revealed [13, 108], and graphene/Ni [162] and graphene/Co [109] moirés were found, owing to which a nanoscale modulation of magnetism induced in carbon could develop [109]. However, none of these studies address the processes by which intercalation takes places.

We performed an *in situ* study of thermally-activated intercalation with the help of real time, *in operando* LEEM measurements. We found that the efficiency of intercalation depends on the interaction between graphene and the metal, more precisely that it is more efficient on those graphene domains which are less coupled to the substrate. Such domains have their carbon zigzag rows misaligned with respect to the dense-packed Ir rows. We also found that the intercalation is occurring through well-defined entry points, which are curved regions of graphene, wrinkles and graphene covering substrate step edges, and found that different kinds of curved regions are relevant depending on the relative orientation of graphene and its substrate.

4.1 INTRODUCTION

Several microscopic mechanisms have been proposed to describe how a foreign species intercalates below graphene. While oxygen intercalates from the edges of graphene flakes grown on Ru(0001) [104, 155] and on Ir(111) [105], alkali metals instead may intercalate at atomic step edges or at boundaries between different rotational domains in graphene/Ni(111) [164] and in graphite [165]. Regarding transition metals, the intercalation mechanism remains elusive. While it has been demonstrated that pre-existing defects in graphene, such as vacancies or pentagon-heptagon pairs, reduce the required energy to trigger intercalation [13, 137], several recent experimental works have shown that other mechanisms could be at work. In particular, atomic defect formation, induced by the transition metal cluster on the graphene sheet, with subsequent restoring of the carbon-carbon bonds, has been suggested as a possible way for metal intercalation [137, 166, 167].

4.2 SAMPLE PREPARATION

Ir(111) bulk single crystals were used as substrates. Their preparation is described in section 2.11. Graphene growth was conducted by CVD at 1000°C with 5×10^{-8} mbar ethylene (see section 2.10). In all experiments presented here, graphene covers about 80% of the Ir surface. Co was subsequently deposited at room temperature from an electron-beam evaporation source at a rate of about 0.3 monolayer (ML) per minute [168].

The onset of intercalation was then followed by imaging the surface while annealing. The LEEM measurements were performed at the Nanospectroscopy beamline of the Elettra synchrotron radiation facility [169].

The LEEM image in Figure 53 illustrates the typical aspect of the graphene/Ir(111) surface, prior to Co deposition. In this image, bare Ir appears as the darkest regions. Consistent with previous literature [53, 170], we observe several rotational domains across the graphene layer with different LEEM contrasts (see different shades of grey in Figure 53(a). Mirco-LEED measurements are used to identify the local crystallographic orientation of these rotational domains, as shown in Figure 53(b)-(d). Beside R0, these orientations correspond to rotation of 14 and 19° of the carbon zigzag rows with respect to the Ir dense-packed atomic rows. In the following, we refer to R14 and R19 when describing these rotational domains. In other places of the surface, we also observe R30 domains (not shown here). Thin lines on the surface are the substrate atomic steps, while thick lines are wrinkles.

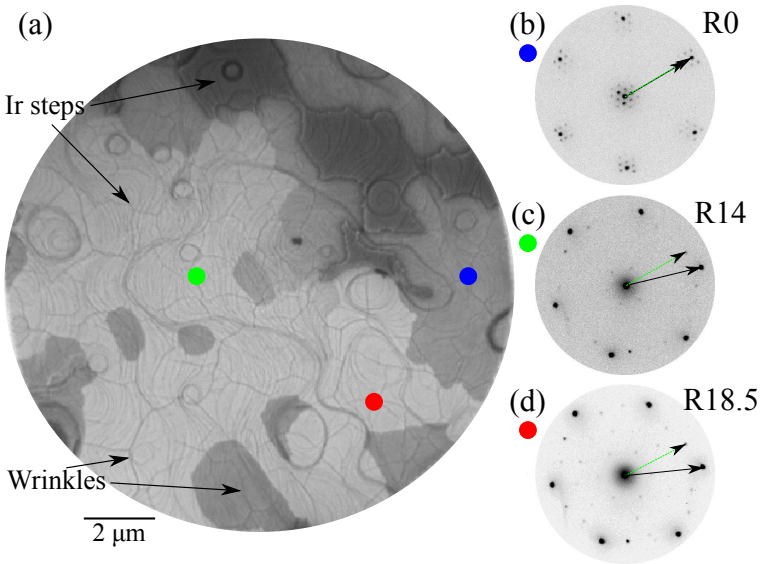

Figure 53: (a) LEEM image (V_{start}= 15 V, 15 µm field of view) of the graphene/Ir(111) surface, showing bare Ir (darkest regions) and three graphene rotational domains. Thin lines all over the surface are Ir atomic steps, while thick lines on the graphene-covered surface are wrinkles. (b-d) 2 µm-diameter selected area of the LEEM image where low-energy electron diffraction has been performed to identify the three graphene rotational domains. In these patterns (V_{start}= 40 V), the black dash arrows indicate the Ir diffraction peaks, while the blue, green and red arrows indicate the carbon peaks for R0, R14 and R19 domains, respectively.

In agreement with other works [12], deposition of 1 ML of Co at room temperature leads to the formation of randomly distributed clusters all over the graphene surface (see black dots in Figure 54(a)).

4.3 ROTATIONAL DOMAIN-DEPENDENT INTERCALATION

Annealing of the Co ML at about 125°C strongly modifies the surface morphology, as shown in Figure 54(b). We observe large dark areas on R14 and R19 where Co accumulates, while, surprisingly, the surface morphology on Ro remains essentially unchanged, although Co starts decorating the Ir atomic steps (the LEEM contrast becomes darker along step edges in Ro domains). In the following, we show that these dark regions on the different rotational domains correspond to intercalated Co.

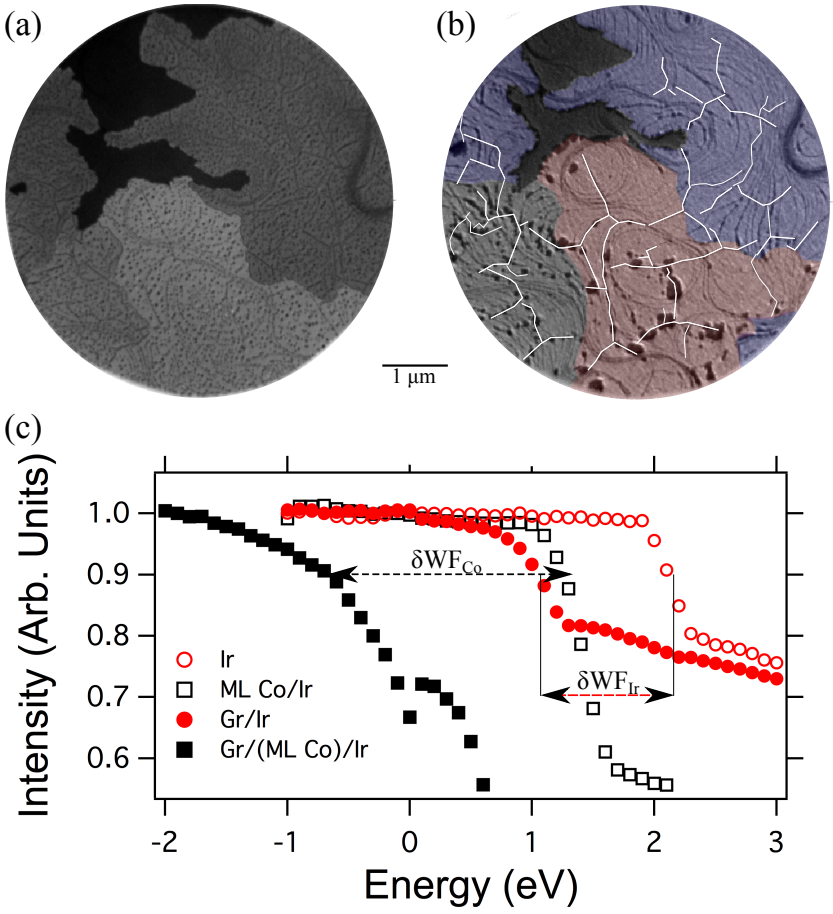

Figure 54: (a) LEEM image of the graphene/Ir(111) surface after deposition at room temperature of a 1 ML thick Co layer, which results in randomly distributed clusters (dark dots) atop the graphene sheet. (b) LEEM image (V_{start}= 4 V) of the same region of the surface after annealing at 125°C. In (b), the different rotational domains have been colored for clarity. Ro, R14 and R19 appear blue, grey and red, respectively. Wrinkles are highlighted by white lines. (c) Work function measurement of clean Ir (taken as a reference) and graphene/Ir surfaces (empty and full red circles, respectively). The same comparison between 1 ML of Co on Ir (empty squares) and the dark regions observed on the R14 and R19 variants (filled squares) demonstrates Co intercalation.

To do so, we use low-energy electron reflectivity, close to the mirror mode conditions[130], to measure the relative changes of the surface work function at different steps of the sample preparation. Here, we define the relative work function (WF) as the energy for which electron reflectivity drops by 10% from total reflectance [171]. To demonstrate Co intercalation, we take advantage of the fact that the WF of graphene-terminated metal surfaces is often lower than the WF of the corresponding clean metal surfaces [78]. This is particularly true for Co and Ir: $\delta WF_{Co} = WF_{Co} - WF_{Gr/Co} \sim +1.7$ eV [78] and δWF_{Ir}=WF_{Ir}-$WF_{Gr/Ir}$ ~+1 eV [172, 171].

We thus compare the surface WF of clean Ir with the one of graphene/Ir and the WF of 1 ML of Co on Ir with the one measured on the dark regions in Figure 54(b). The results, reported in Figure 54(c) show that δWF_{Ir} ~1 eV, in agreement with previous experimental works [172, 171], and that δWF_{Co} ~1.8 eV, demonstrating that the dark regions in Figure 54(b) are indeed intercalated Co. Interestingly, the amount of intercalated Co is significantly different for the three rotational domains. Note for example that, while intercalated Co make relatively large flakes below the R14 and R19 domains, it is hardly detectable on Ro (see Figure 54(b)). These results show that the intercalation efficiency depends on the graphene rotational domain on which Co has been deposited, suggesting that the strength of the graphene/Ir interaction plays a role in the process. In fact, a lower graphene/Ir interaction energy has been recently reported for the R30 domain compared to the one found for the Ro domain [171]. A similar variation of the interaction energy is also expected for the R14 and R19 rotational domains [172].

4.4 INTERCALATION STARTING FROM CURVED GRAPHENE REGIONS

The LEEM image shown in Figure 54(b) reveals another intriguing aspect: while Co intercalation preferentially takes place at Ir step edges on Ro, the intercalation regions on R14 and R19 often appear on/close to graphene wrinkles. The intercalation mechanism itself, at the microscopic level, is thus variant-dependent. A closer look at the LEEM images, acquired while annealing, reveal that once intercalated, Co diffuses along the Ir atomic steps on the Ro domain and wets isotropically the Ir surface on the R19 domain (see Figure 55). Part of these results are consistent with recent STM measurements in which Co [109] and Ni [162] islands intercalated at the graphene/Ir(111) interface have been found mostly at the Ir step edges under the Ro rotational domain. However, to the best of our knowledge, the role of graphene wrinkles in the intercalation process of a transition metal has not been anticipated in these earlier studies.

It is unlikely that the intercalation is induced by pre-existing defects in the graphene layer, as there is no reason to have defects only close to atomic steps on Ro and only close to wrinkles on the other rotational domains. Intercalation has not been observed either at domain grain boundaries, where pentagon-heptagon defects are located [14]. These different observations indicate that curved regions of the graphene sheet facilitate Co intercalation in the temperature window we probe in this work. Also, in all our experiments, we observe negligible Co intercalation at the edges of the graphene flakes. This suggests that the energy barriers for intercalation are lower when Co is on top of graphene and close to a wrinkle or an atomic step than on the Ir surface, where graphene binding is strong [53, 173]

Although an atomic description of the intercalation process is not possible with LEEM, a few speculations can be made to explain why curvature is a key parameter.

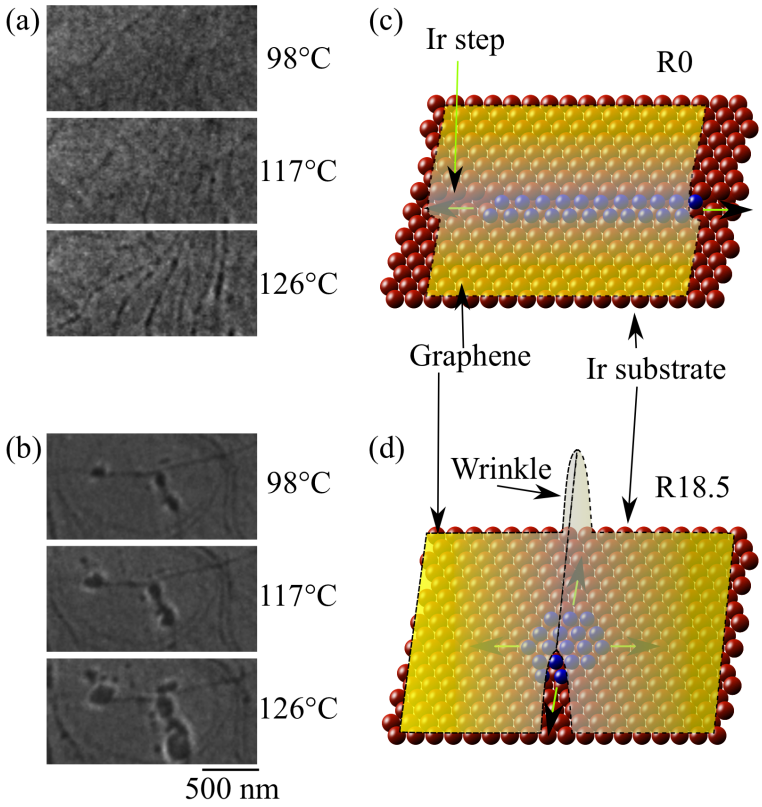

Figure 55: LEEM images (V_{start}=10 V) showing the intercalation of Co at different annealing temperatures on Ro (a) and on R18 (b). (c-d) Schematic representation of the proposed intercalation mechanism. On Ro domains, Co intercalates at atomic step edges and diffuses along the steps (c), while on R19, Co intercalates at wrinkles and wets isotropically the Ir surface (d).

For flat and free standing graphene, the formation of a vacancy requires high energy, about 7 eV [174], but this value drops to 1.5 eV in the presence of Co clusters [175]. In addition, previous works on carbon nanotubes showed that the vacancy formation energy decreases with increasing curvature [176]. In particular, for a nanotube diameter of 5 Å, corresponding approximately to the graphene curvature at the Ir step edges [14], the vacancy formation energy is reduced by 2 eV with respect to the free standing graphene [176]. The di-vacancy formation energy is even smaller both in presence of Co clusters and for curved graphene sheets. It is then reasonable to believe that defects form in the graphene sheet when a Co cluster has nucleated at a graphene wrinkle or at an Ir atomic step, without the need of pre-existing point defects.

4.5 CONCLUSION

Using low-energy electron microscopy, we have study Co intercalation under high-quality graphene grown on Ir(111). We have found that the efficiency of Co intercalation at the graphene/Ir(111) interface depends on the rotational orientation of the graphene domain on which Co is deposited: Upon annealing at about 125°C, Co intercalation is much faster on R14 and R19 domains than on Ro domains. However, intercalation does not occur everywhere. Instead, depending on the rotational ori-

entation of the graphene domains, Co finds specific regions of the surface, such as atomic steps and wrinkles where curvature of the graphene sheet is high, to reach the Ir substrate: on R0 domains, Co preferentially intercalates at Ir step edges, while it mostly intercalates at wrinkles on the R14 and R19 domains. These results suggest that the strength of the graphene/Ir interaction determines which pathway is energetically more favourable. Our work opens new opportunities to grow systems where the intercalation mechanism could be controlled at the nanoscale. Moreover, these pathways that facilitate intercalation offer the advantage of working at moderate annealing temperature, thus limiting possible intermixing between the intercalated metal and the substrate.

5

GROWTH AND STRUCTURE OF A STRONGLY BONDED SYSTEM, GRAPHENE ON RE(0001)

One route towards inducing novel properties into graphene is to prepare it onto a material both serving a substrate for growth and exhibiting desirable properties to be induced by a proximity effect in graphene. As concerns superconductivity, rhenium as an interesting candidate in this respect, given its catalytic activity with respect to the cracking of carbon containing molecules, which is requested for CVD of graphene, and its high critical temperature of 1.7 K until which it sustains a superconducting state. We have developed the growth of graphene on Re(0001) substrates of two kinds, bulk single crystals and thin films on sapphires. The growth processes are different in the two systems: while a surface-confined growth, only active in a narrow temperature window, was found the only way to achieve graphene rather than a surface carbide in the first case, in the second case a temperature-induced surface segregation was found to be an easy-to-implement approach. We find that graphene on Re(0001) exhibits features which are typical of a strong interaction between graphene and its substrate, and identify localized defects in graphene.

Our analysis is based on *in situ* monitoring of the growth with the help of LEEM and LEED, performed at the Nanospectroscopy beamline at ELETTRA, STM performed both *in situ*, in the same system where the samples were grown in our laboratory, and *ex situ*, with a low temperature STM with our collaborators at CEA, Raman spectroscopy, and DFT calculations.

5.1 RHENIUM AS A SUBSTRATE FOR GRAPHENE

The Re-C system is actually more complex than as expected from "classical" phase diagrams (Figure 56). Several carbide phases are documented [177, 178, 179], among which the rhenium carbide Re_2C. This phase has been synthesised at high temperature and high pressure [177]. This phase also studied by surface science technique and it forms upon thermal decomposition of hydrocarbons at low temperatures 500 K [180]. The carbon solubility in Re is high as compared to that in Ir and Pt for instance, and amounts 8×10^{-2} atomic percent (.at%) at 1275 K while 5×10^{-3} .at% at 975 K. It is similar to that in Rh or Ru. How graphene grows on these two metals is a guide for foreseeing possible growth processes on Re.

On Ru(0001), a process based on the high temperature (e.g. 1320 K) decomposition of carbon precursors accompanied by a dissolution of carbon inside the bulk, and cool down yielding a strong decay of the carbon solubility, leading to surface segregation of carbon and graphene growth, is often employed [182, 42, 77]. Another process has also been reported, in which carbon is deposited onto Ru(0001) at a temperature for which the carbon solubility in Ru is low enough to prevent carbon diffusion inside the bulk. In such conditions graphene grows in a surface-confined manner [66].

On Rh(111), the competition between carbide and graphene formation, makes it difficult to achieve solely graphene [183]. It was shown that the nucleation of graphene

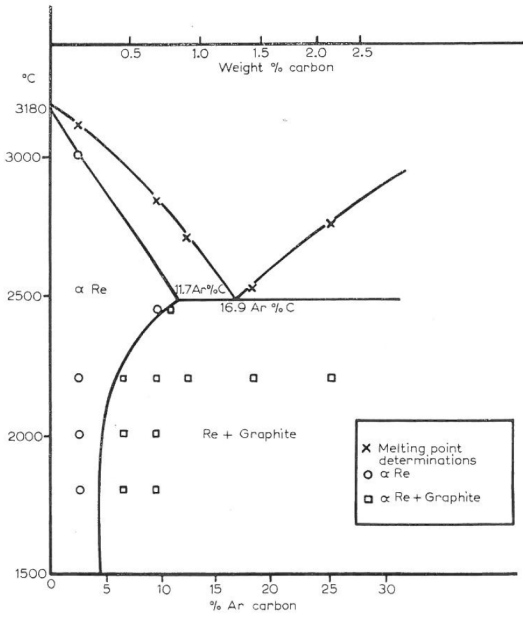

Figure 56: Phase diagram of a Re-C system [181].

requires a higher surface concentration of carbon adatoms than the nucleation of the surface carbide. On the contrary, once nucleated, graphene islands were found to grow faster than carbide once. In order to prepare a full layer of graphene, growth was started with a high carbon precursor concentration at the surface, achieved by adsorbing a full precursor layer at room temperature. This is a so-called temperature programmed growth (TPG). Growth was continued with a standard CVD step during which the pre-formed islands were found to grow until coalescence.

Re(0001) as a substrate for graphene growth was used in two forms:

High purity bulk single crystals were employed. Their preparation consisted in sputtering cycles with argon ions at room temperature for 10 min and an Ar pressure in the chamber of about 10^{-5} mbar, followed by annealing to a temperature of 1000 K for about 10 min. The sample is kept at 400 K and the chamber is backfilled with 2×10^{-7} mbar of oxygen for 30 min. A final quick flash annealing to 1900 K finished sample preparation. Figure Figure 57a shows the resulting smooth surface, as observed by LEEM: except for defects in the channel plate, the only visible features are Re(0001) atomic steps, which separate micrometer-wide terraces. The LEED pattern (Figure 57b) is characteristic of a single crystalline orientation surface.

A second kind of samples, few 50 nm-thick Re thin films on C-plane sapphire, were also employed. These were prepared by Bruno Gilles and Benjamin Delsol at the SIMAP laboratory in Grenoble, by molecular beam epitaxy (see experimental part).

The epitaxy of the films was checked by RHEED and the topography by STM Figure 58. STM images display atomically flat terraces with mounds on top. These islands have a size of about 300 nm. The formation of these mounds is due to the spiral growth method in which the growth starts in a three dimensional mode but transforms into two dimensional mode as the film gets thicker. Coalescence of larger number of initial growth islands may lead to screw dislocations Figure 58b due to the layer structure resulting in spiral-island growth mode, with the screw dislocation as the growth flow axis. The dislocations are generated by the accommodation of small translational or rotational displacements as adjacent islands agglomerate. This is referred to as the

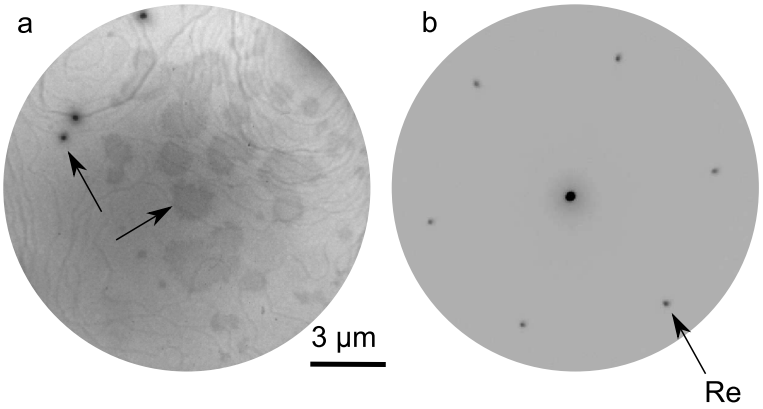

Figure 57: a) Structure of a clean Re single crystal: a) Bare Re surface imaged by LEEM, b) corresponding LEED pattern at 33 eV of Re(0001) crystal. The black arrows show some defects in the channel plate.

Screw-island or Spiral-island growth mode. Another interesting feature is that multiple steps merge together to form steep edges.

The surface quality of the Re(0001)after treatment shows a streaky RHEED patterns, suggesting that the Re is atomically smooth. Kikuchi lines are further evidences for the quality of the surface. This indicate a chemically clean and crystallographic well-ordered substrate surface with a single crystallographic orientation.

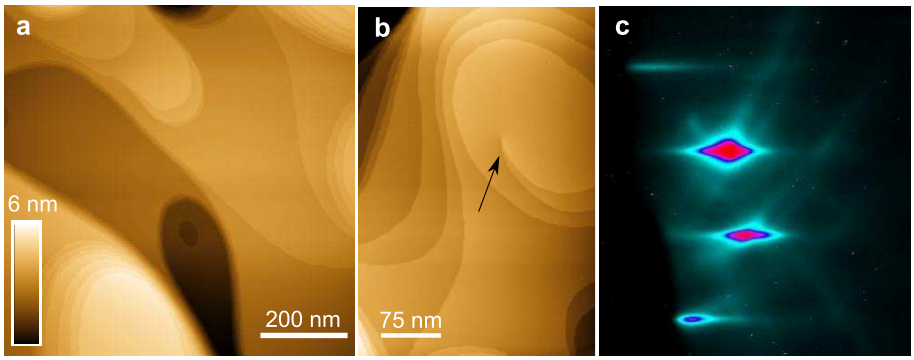

Figure 58: a) STM topographs 600 nm^2 under UHV of Re(0001)/Al_2O_3(0001). b) STM image 400 nm×550 nm shows a multiple steps merging together with a mound having a dislocation as indicated by black arrow. c) RHEED (20 keV) pattern of Re layer showing the orientation of the streaky pattern.

5.2 GRAPHENE ON BULK SINGLE CRYSTALS: SURFACE-CONFINED GROWTH

5.2.1 *Carbon dissolution in the bulk*

Inspired by the method reported by Sutter et *al.* for growing graphene on Ru(0001) [42], we have exposed the Re(0001) single crystal to a 4×10^{-7} mbar partial pressure of ethylene for 15 min at 1175 K. Cooling down however did not lead to any surface segregation induced by a decay of the carbon solubility in Re. We ascribe this disappointing result to the fact that our Re single crystal are extremely pure and are thus an infinite

reservoir for carbon storage. At the temperature which are relevant (see next paragraph) for carbon surface segregation, the diffusion length of C atoms inside the bulk of Re is presumably very large, such that it is not possible to establish a sufficiently abrupt carbon concentration gradient versus depth in the crystal: neither in the bulk in average, nor close to the surface, can a sufficiently high carbon bulk concentration (i.e., close to a few 10^{-2} atomic percent) be achieved which would exceed the carbon solubility upon cool down. Since we did not wish to enrich (and thus, permanently pollute) the costly Re crystal with a large amount of carbon by prolonged exposure to ethylene at high temperature, an alternative growth method was needed.

5.2.2 *Direct deposition of ethylene at elevated temperature*

Growing high quality graphene requires high temperatures in order to promote efficient surface diffusion of carbon adatoms and mobility of small graphene nuclei. However, in the present case this requirement is problematic: at temperatures above 800-850 K a surface carbide phase starts to form and to the expense of graphene. Carbide formation is illustrated in Figure 59: the Re(0001) surface was exposed to 4×10^{-7} mbar of ethylene. At 875 K we observe a mixture of graphene and phase having a complex diffraction pattern. Recent works support the idea that this phase corresponds to a surface carbide, but do not conclude on the exact nature of this complex structure. The former preferentially formed at the Re(0001) step edge. At 905 K, the carbide phase forms exclusively. The micro diffraction pattern (Figure 59b) reveals the characteristic signature of the carbide, which is much different from the graphene one (see below).

We note that below 800 K, graphene forms with a low structure quality, as expected for such low temperatures.

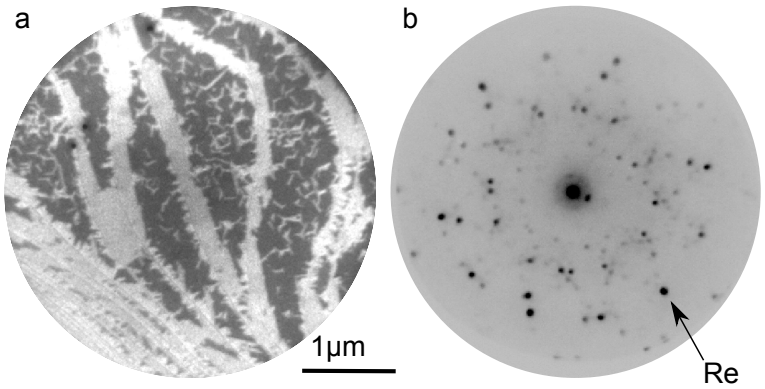

Figure 59: a) LEEM image of the Carbide growth on Re at 905 K. b) LEED pattern at 45 eV electron energy of the carbide formed.

5.2.3 *Avoiding the formation of the surface carbide*

We tested three approaches, all intended to favour the growth of graphene to the expense of that of the surface carbide.

The first approach (Figure 60a) relied on the recipe developed by Dong et *al.* for graphene growth on Rh(111) [183] (see above). It was indeed possible to grow graphene by increasing the carbon concentration, in a TPG process, conducted by heating up to

805 K a substrate whose surface has been covered with a layer of ethylene at room temperature. This suggests that the carbon surface concentration needed for nucleating graphene is higher than for nucleating the carbide, and that graphene, at this carbon surface concentration, forms preferentially. TPG only yields a partial coverage. The graphene is not stable beyond the temperature 875 K.

The second step in the recipe from Dong *et al*, exposure of the hot surface with preformed graphene islands to ethylene (CVD), does not have the desired effect, of increasing the graphene coverage. Instead, the surface carbide forms rapidly, and the whole surface is converted to a carbide (Figure 60a). This implies that unlike on Rh(111), on Re(0001), the carbide phase forms more rapidly at the carbon adatom concentrations accessible during the second step (this concentration is substantially smaller than that in the TPG step).

The second approach (Figure 60b) intended to exploit the expected different chemical reactivity of the carbide and graphene. It was shown for instance that on Ir(111), different graphene variants have different stability versus high temperature oxygen etching [138]. With this in mind we studied the relative stability of the carbide and of graphene versus high temperature (845 K) oxygen (2×10^{-7}mbar) exposure. Unfortunately we found that graphene is less stable than the carbide.

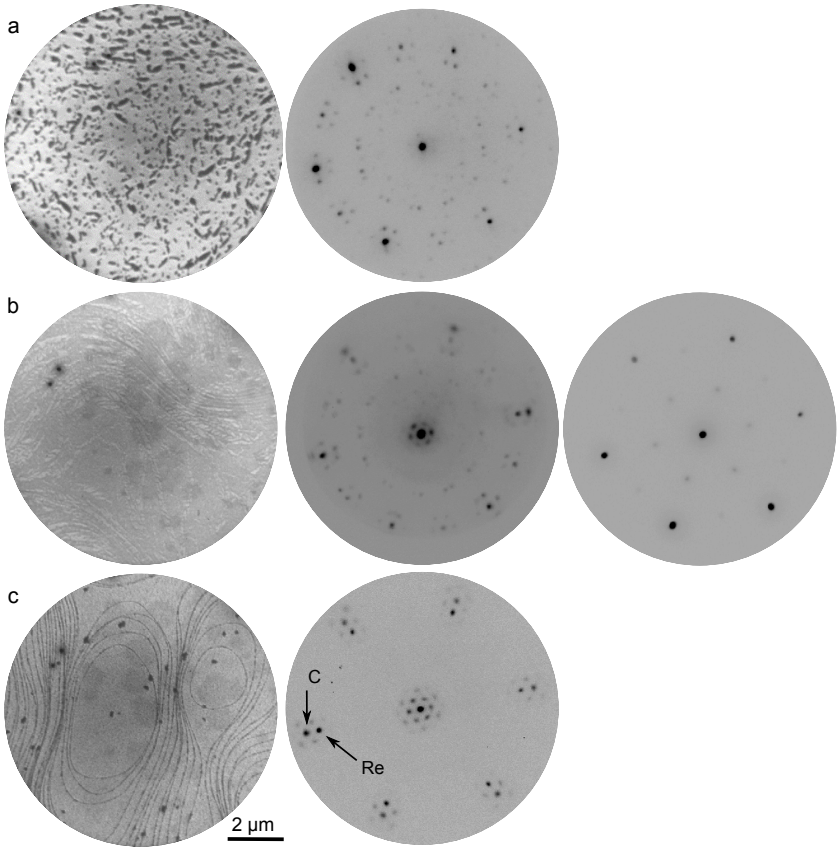

Figure 60: LEEM images left with LEED pattern (E= 55 eV) right of (a) CVD at high temperature yielding carbide; (b) middle is for one TPG cycle showing graphene with carbide, right oxidation of the surface after oxygen exposure; (c) 3 cycles of TPG growth showing high quality graphene. The Re inner spot with graphene spot are surrounded by smaller satellite spots reflecting the periodicity of the moiré. The centre spot is also surrounded by moiré induced spots.

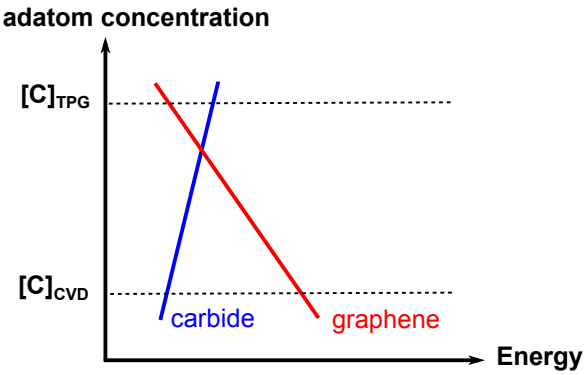

Figure 61: Cartoon schematizing the total energy of the graphene and carbide phases as a function of the carbon adatom concentration on the Re(0001) surface in equilibrium with graphene/carbide phases during growth.

The third approach consisted in repeated TPG cycles (Figure 60c). Given that ethylene only sticks on graphene-free regions upon heating, and that a full layer of ethylene adsorbed at room temperature onto transition metals (e.g. Pt(111) [184], Ir(111) [14]) encloses an amount of carbon atoms equivalent to 25 % of a graphene layer, one expects that the coverage of the Re(0001) surface with graphene, θ_n, will asymptotically reach 100 % as a function of the number n of TPG cycles, according to $\theta_n = 1 - (1 - 0.25)^n$. With 3 cycles (room temperature adsorption of ethylene and 933 K annealing), one achieves about 50 % coverage, as expected, of graphene with a well-defined epitaxial relationship with respect to Re(0001) (carbon zigzag rows aligning Re dense-packed ones), as seen in (Figure 60c). No carbide phase is formed in this process if the temperature does not exceed 995 K, and the onset of graphene formation, from a carbidic phase (non fully de-hydrogenated ethylene), is observed from 625 K.

These observations show that (i) the critical carbon adatom concentration for graphene nucleation is higher than for carbide growth, (ii) the energy of carbon in the graphene phase is higher than in the carbide phase when growth is performed for a low carbon adatom concentration on Re(0001) such as encountered under CVD conditions, a situation which is inverted at high carbon adatom concentrations such as encountered under TPG conditions; the relative energy of the carbide and graphene phases dictates which phase will grow preferentially (Figure 61). A schematic view of the three approaches used is highlighted in Figure 62.

5.3 GRAPHENE ON THIN FILMS: SURFACE SEGREGATION

5.3.1 *Graphene formation*

As we have seen in the previous section, surface segregation upon cool down, of carbon stored in the bulk of Re, is not possible with a high purity bulk crystal, because it is a too large reservoir to be filled with carbon. In order to take benefit of this simple mechanism, we have employed a second kind of substrates, Re thin films (see section 2.8), which, due to their limited thickness (few 50 nm), are sufficiently small reservoirs that a substantial carbon concentration can be induced in them by exposure at high temperature (typically 1265 K) to ethylene doses easily accessible in a UHV system.

Considering the carbon solubility in Re at 1175 K, 5×10^{-2} atomic fraction, one expects indeed that 20 min exposure to 10^{-8} mbar pressure of ethylene (about 15 langmuirs, symbol L) at this temperature will saturate a 50 nm-thick metal film with carbon.

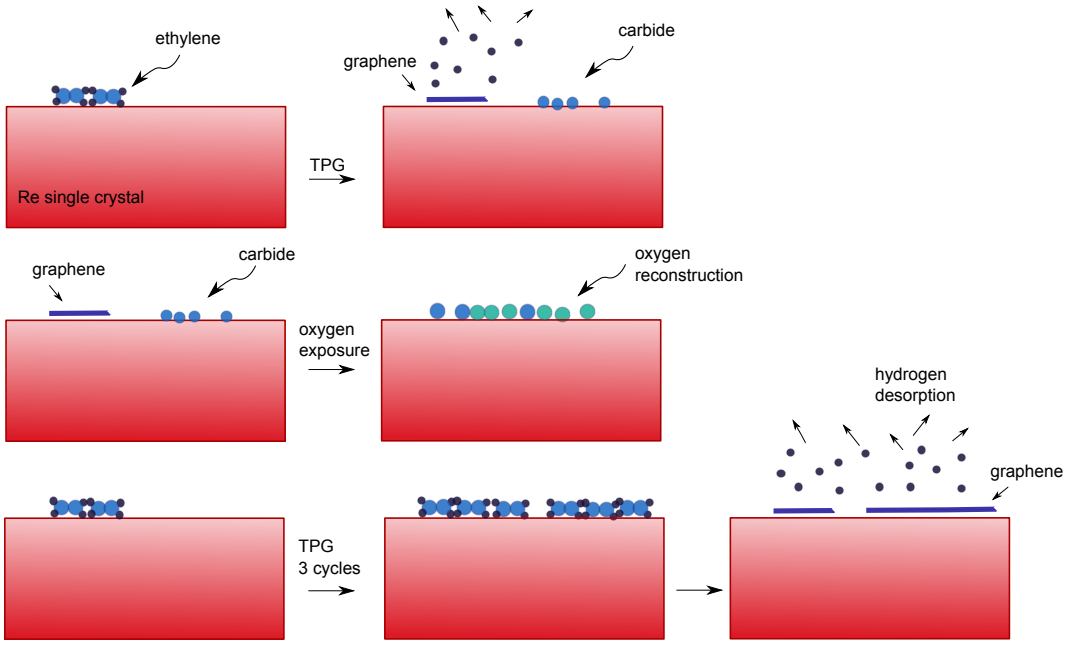

Figure 62: Schematic of the three approaches used to attempt the growth of graphene on high purity bulk single-crystal Re(0001). The carbon precursor is depicted in blue. a) Hydrocarbons are adsorbed on the metal surface. Upon annealing hydrogen desorbs and graphene island forms (TPG). Annealing under an ethylene pressure does not increase the coverage of graphene but rather carbide formation. b) Exposure of a Re(0001) surface covered with graphene and carbide leads to the preferential etching of graphene and to the formation of an O-reconstructed (2×2) Re(0001) surface. c) 3 TPG cycles allow preferential growth of graphene.

The segregation of this whole amount of carbon to the surface of the metal would correspond to about 4 monolayers of graphene.

This thermodynamic consideration is of course not the only ones to be taken into account: kinetics may also play a crucial role here, as shown by the influence of the cooling rate. Whatever the amount of carbon dissolved into bulk Re, which we have varied between a few 1 L and a few 10 L in our experiments, we believe that when graphene formed, we systematically observed prominently single layer on the surface.

When rapidly crossing the temperature at which the carbon concentration in the bulk exceeds the bulk solubility, typically 875 K, with a 100 K/s rate, no graphene is observed on the surface (Figure 63a). For a moderate cooling rate (20 K/min) on the contrary, one observes a nanometre scale triangular pattern on the surface with STM (Figure 63b), which is typical of a moiré between single layer graphene and a transition metal surface (this superstructure will be described more into details in the next section).

5.3.2 *Different phases on Re(0001)*

Besides the graphene phase, we observe the formation of two other phases at the surface, which tend to form when large, few 10 L, ethylene doses are employed. Altogether, they can cover about 18 % of the sample surface for a 12 L dose of ethylene. These phases are disordered as seen on the STM images (Figure 64) by our collabora-

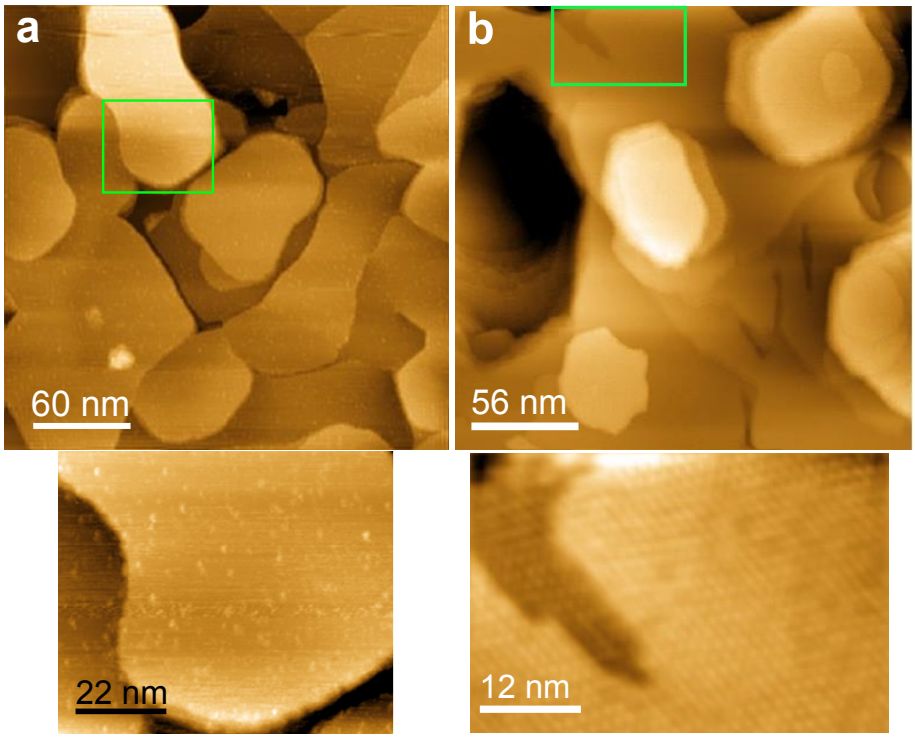

Figure 63: STM topographs of graphene on Re prepared with different cooling rate, (a)100 K/s, (b) 19.5 K/min, with 6L. Bottom: corresponding zoomed-in images.

tors at CEA, and as confirmed by the absence of any measurable diffraction pattern in RHEED experiments. Given the disorder of these phases, only speculations can be given at this point regarding their nature. One of the two phases seems a non-dense one which exhibits no particular feature (Figure 64a). We surmise that this phase is a carbide. The second one seems flatter and exhibits features resembling some moiré sites, though with a high disorder (Figure 64b). We tentatively identify this phase as bilayer graphene [185] or ill-crystallized graphene [186].

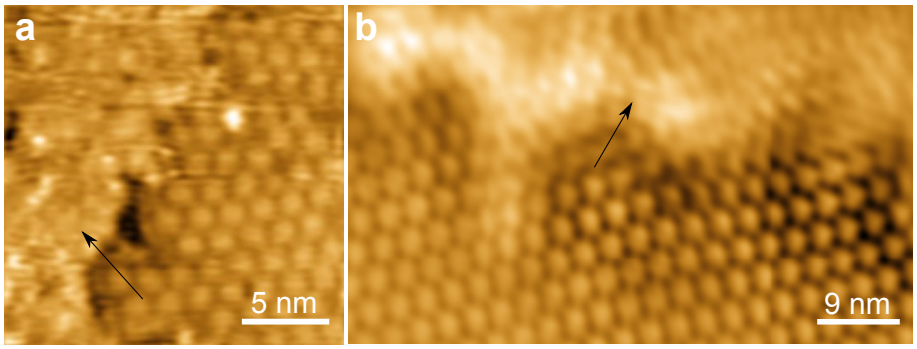

Figure 64: STM topographs of graphene on Re showing different phases indicated by black arrows, (a) showing carbide phase. Image courtesy of C. Tonnoir and C. Chapellier from CEA-INAC, (b) 25 nm^2 showing bilayer graphene.

Despite our repeated efforts, we could not achieve atomic resolution STM imaging on neither of these two phases, which would provide valuable information as to their nature. However we performed *ex situ* AFM measurements in order to obtain com-

plementary characterization. One observes that some regions have a markedly larger phase signal (Figure 65). The corresponding surface fraction roughly matches with that estimated from STM for one of the disorder phase discussed above (surmised to be a carbide). The position of these regions is only partially correlated with the location of the highest mounds of the substrate. The occurrence of regions with difference phases points to locally different force dissipations. This could signal the occurrence of regions (e.g. a carbide) having different interactions with the substrate, thus adsorbing atmospheric molecules in a different manner, in turn modifying the interaction between AFM tip and surface (Figure 65). Such a mechanism was invoked for understanding different AFM phase contrasts in graphene/SiC samples [126].

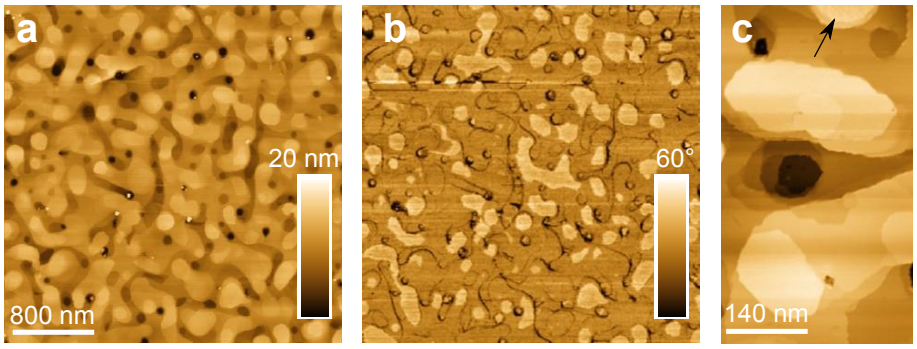

Figure 65: (a,b) AFM (topography, phase) of graphene/Re(0001) exposed to 12L with a cooling rate 13 K/min. (c) STM image showing the presence of a carbide phase on top mound indicated by a black arrow.

5.3.3 *Defects in graphene*

We observe large vacancies on graphene-covered terraces. Graphene uniformly covers the terrace, including at the location of the vacancies, as shown by the presence of a moiré spreading all across the surface (Figure 66a,b). The size of the vacancies was found to increase with ethylene dose during the carbon enrichment phase of the growth. Besides these defects, we also observe smaller ones, dark spots in the moiré at locations where one would expect a bright spot in STM images (Figure 66c). The density of these defects also increases with ethylene dose. Further work is needed to elucidate the origin of these defects. In the (Figure 66a), a contrast inversion marked by the arrows, is observed from one terrace to the neighbour one. The origin of this effect is still unclear, but points to a distinctive interaction between graphene and Re(0001) from one terrace with the other. Further investigation with scanning tunnelling spectroscopy is currently undertaken to study these defects more in a depth manner.

5.4 GRAPHENE-RE(0001) INTERACTION

5.4.1 *Moiré periodicity and orientation*

STM images routinely reveal the moiré between graphene and Re(0001) which was already mentioned several times in this chapter. The moiré shows a preferential orientation, reflecting a preferred graphene/Re relative orientation, in which the zigzag

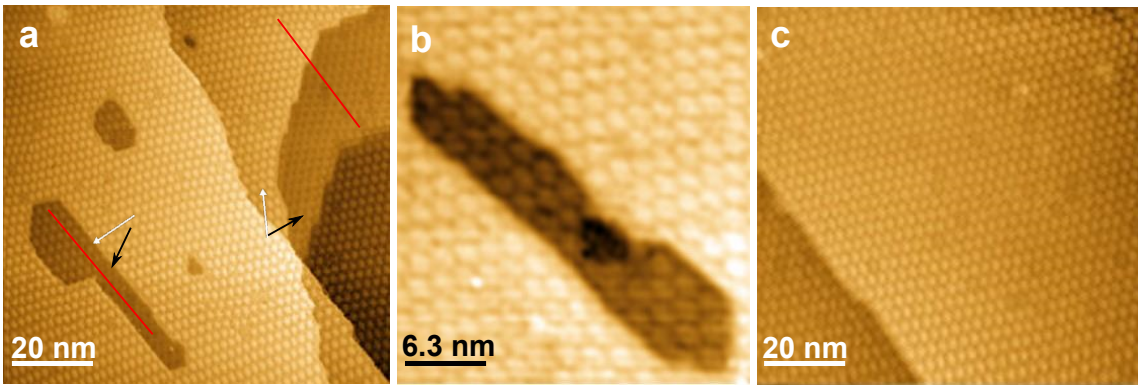

Figure 66: (a), (b) STM topographs of graphene/Re(0001) showing large defects. The white and dark arrows indicate a bright and a dark atop contrast in the moiré, respectively. The red lines illustrate the continuity of the rows of moiré across the contrast reversal. (c) STM image showing the presence of a defects in the moiré.

carbon rows align the Re dense-packed ones. However, deviations from this ideal situations are sometimes observed, with rotations as much as 2°, [14] corresponding to a 1° rotation between the graphene and Re lattices.

The moiré has different sizes depending on the preparation conditions. Analysing LEED patterns such as in Figure 60, we find that preparation on a bulk single crystal (section 1.2) yields a moiré with 2.3 nm periodicity, corresponding to 9 carbon rings matching 8 Re atoms. On a thin Re film, analysing STM images (Figure 68) and RHEED patterns (Figure 67), we find 1.9 nm and 2.4 nm periodicities corresponding to 8 carbon rings matching 7 Re atoms, and 10 matching 9, for different preparation conditions. For bulk single crystals and thin films, graphene growth sets in at different temperatures. Assuming that graphene locks on its substrate at its growth temperature, the structure of graphene is set by the lattice parameter of the substrate at the growth temperature, which differs in the two cases. The different commensurabilities for graphene on thin films could point to a slightly different lattice parameter of the substrate due to a different carbon bulk concentrations, and to a different segregation temperature upon cool down also due to different carbon bulk concentrations.

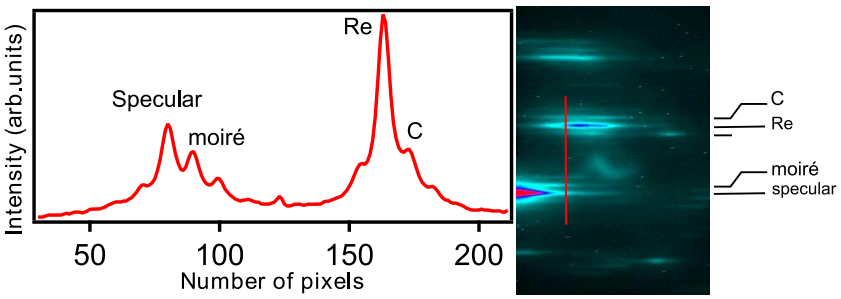

Figure 67: right, RHEED pattern of graphene/Re(0001) 20 kV, [100] azimuth. First order Re, graphene and zero streaks are highlighted as well as one second order moiré streak for a superstructure (9:10). Left: Line profile across the streaks.

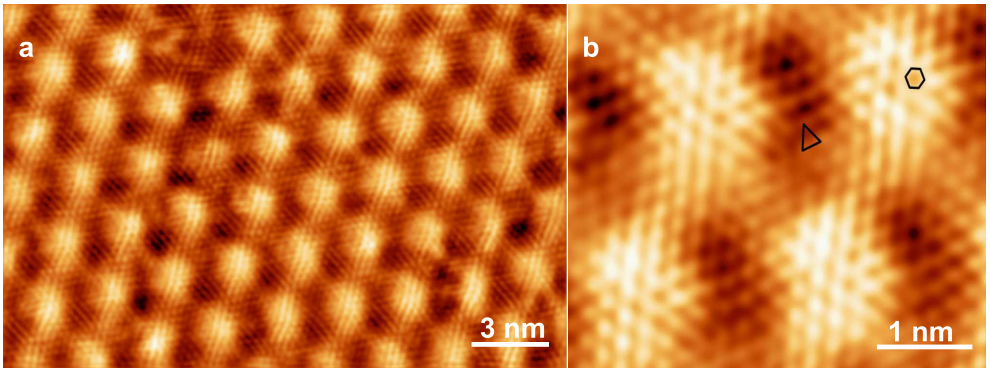

Figure 68: a) STM image showing the moiré pattern, measured with a bias voltage V_{bias}= 224 mV and a tunnelling current I = 31 nA. b) STM image exhibiting an atomic periodicity of order six on the hills of the moiré and three in the valleys, measured for V_{bias}= 10 mV and I = 10 nA. b) Image courtesy of C. Tonnoir and C. Chapelier from CEA-INAC.

5.4.2 *Moiré corrugation and nature of the graphene-Re interaction*

This moiré has a strong corrugation, typically 1 Å, comparable to that in graphene/Ru(0001) and substantially larger than that in graphene/Ir(111). Further analysing the geometrical properties is important as it informs about the graphene-Re interaction. However STM is not a suitable tool for this purpose, due to its mixed sensitivity to both the structure and the local density of state, which is expected to vary within a single moiré unit cell.

For this reason we switch to a density functional theory analysis which was performed in our laboratory by Laurence Magaud. *Ab initio* calculations have been carried out with the code VASP [187]. PAW approach [188], PBE functional [189] and Grimme corrections to van der Waals (vdW) interactions [190] have been used. The slab used to describe the system contained five Re layers, one graphene layer and a 10 Å-thick vacuum space on top. The Re plane in the middle (third plane) of the slab was fixed while all the other atoms were allowed to relax (more details will be explained elsewhere, (see Figure 69). The lateral size of the supercell has been fixed to the geometry observed experimentally and corresponds to a (7:8) superstructure. Calculations were performed with one K-point, the supercell K point to get a precise description of the graphene low energy states. After convergence, residual forces were lower than 0.025 eV/Å.

Calculations show that the graphene layer is buckled with regions where the C atoms are close to Re ones and regions where they lay much higher (Figure 69a). The amplitude of the buckling is found to be 1.6 Å. The smallest C-Re are 2.24 Å, which corresponds to a covalent C-metal bond, while the larger distances are 3.97 Å, i.e. larger than between two graphene planes in graphite. The first regions correspond to strong graphene-Re interaction (so-called top hcp and top fcc) with the formation of covalent bonds and an electron transfer from Re to C atoms (Figure 69b). The second regions correspond to a much weaker interaction (so-called hcp and fcc), presumably vdW. The Re layer below graphene is also slightly buckled, with corrugation height 0.15 Åin the Re layer just below and 0.13 Åin the second Re layer. The higher Re atoms lie below the higher C atoms. The C-Re pairs distribution (Figure 69e) shows some

variations with the ones of Miniussi *et al.* [191], which can be due to the (7:8) geometry and the vdW corrections. A calculation in a (9:10) cell with vdW interactions already shows variations in the Re-C pair distribution with a smaller proportion of large distances. This is expected since vdW interactions have been shown to reduce the height of the graphene ripples in the region of weaker interaction, like in graphene/Ru for instance [6]. Overall the calculation provide good agreement with our STM images (Figure 69c,d). Calculations show the square modulus of the wave function integrated between the Fermi level (E_F) and E_F+0.5 eV. This cross section is taken just above the highest graphene atom. It shows bright protuberances that correspond to hcp-fcc stacking regions and lines. Carbon related states (at Γ point) are found at an energy lower than in graphene indicating an electron transfer from Re to C. Because C hybridization is modified, it is not possible to give a quantitative value of this charge transfer.

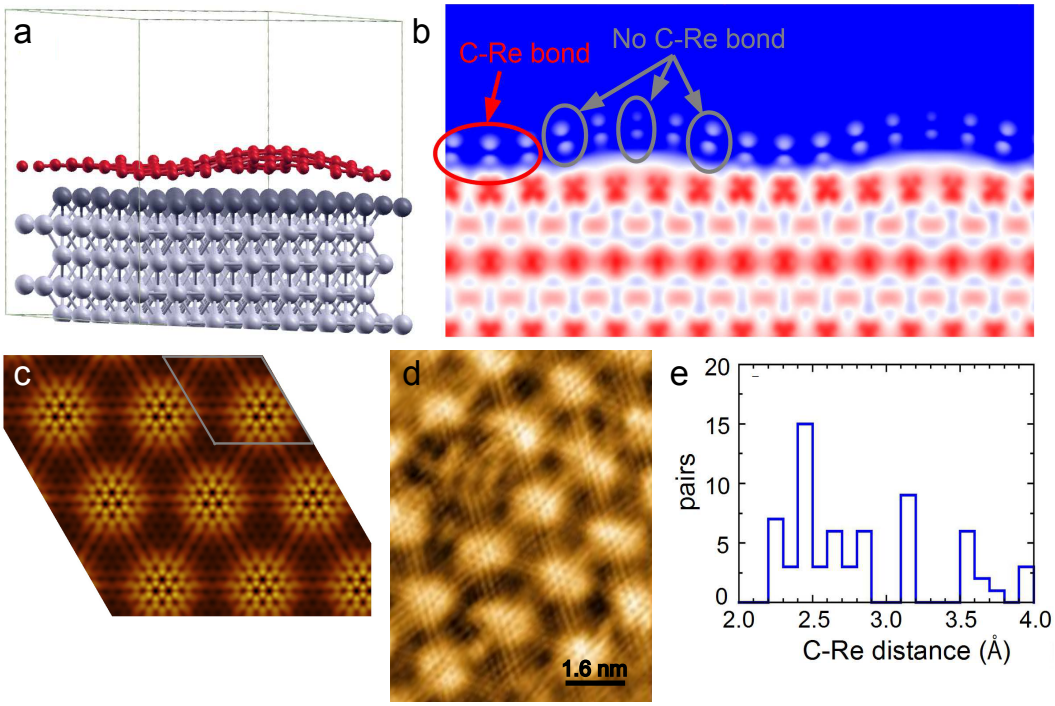

Figure 69: a) Schematic view of the supercell from the side to show the graphene buckling. b) Cross section of $|\Psi|^2$ integrated between -0.5 and 0 eV. The cross section line is parallel to the x supercell axis and goes through the hcp fcc site. Colour scale: blue: low, white: intermediate, red: strong intensity. c) Ab initio calculation results for the (7:8) superstructure. Cross section of the square modulus of the wave function integrated between E_F and E_F+ 0.5 eV. d) High resolution STM topograph of graphene/Re. e) Number of C-Re pairs as a function of distance.

Band structure calculations (not given) show that the valence band of Re is broad. The fact that it dominates the states in the vicinity of the Fermi level complicates the interpretation of the results. To search for graphene Dirac cones, we selected the eigenstates with the strongest carbon character but we found no trace of graphene linear dispersion which is another evidence of the strong graphene-Re interaction. Carbon related states (at Γ point) are found at an energy lower than in graphene indicating an electron transfer from Re to C. Because C hybridization is modified, it is not possible to give a quantitative value of this charge transfer.

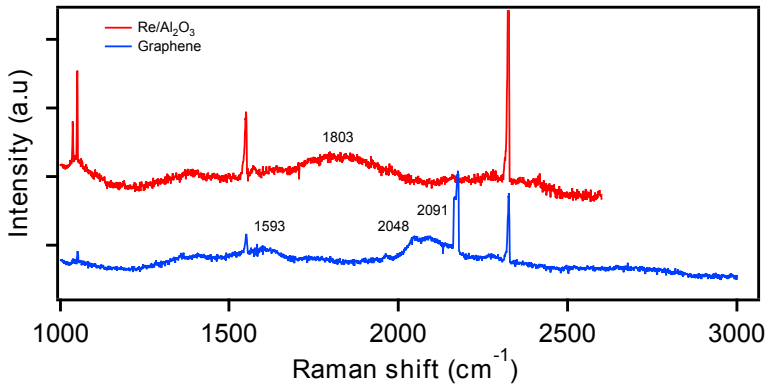

Figure 70: (Raman spectra taken at the surface compared to Re substrate.

5.4.3 *Suppression of graphene Raman modes due to the interaction with Re*

Ex situ Raman spectroscopy reveals a strong luminescence from the Re thin film, and vibration modes which are typical of Re [192] (Figure 70). However, none of the graphene signature, the G and 2D vibration modes, could be observed. This was carefully checked with high measurement times and for two different wavelength of the excitation laser. We cannot rule out that the graphene signals, of they indeed exist, are overwhelmed by the strong luminescence background from the Re.

Our observations is unlike the situation (see dedicated chapter in this thesis) of a weak interaction between graphene and a substrate, like Ir(111), but similar to those obtained on a strongly coupled system, graphene on Ru(0001) [185]. In this system it was proposed that the Kohn anomaly in graphene was suppressed due to the strong interaction with Ru(0001). Such a suppression was argued to make the graphene G and 2D modes forbidden [193]. Here we demonstrate a similar effect in graphene in Re(0001), which is unlike the situation of a weak interaction between graphene and a substrate like Ir(111).

5.5 CONCLUSION

We have established two growth methods for graphene on Re(0001):

> on high purity bulk Re single crystals, only several TPG cycles allow forming high quality graphene without carbide, thanks to the different carbon adatom concentrations needed for nucleating and for equilibrium between graphene/carbide islands and the carbon adatom.
>
> on thin Re films, a surface segregation process induced by cooling down the sample after it has been enriched by carbon in its bulk, yields prominently graphene, but also other phases which we tentatively identify as carbide, bilayer graphene, and disordered graphene phases.

The interaction between graphene and Re(0001) is strong, giving rise to a moiré with a strong buckling and presumably a deep modification of graphene's electronic properties, as suggested by the DFT calculations and as shown by the absence of Raman modes.

Graphene on Re(0001) thin films reported here have been employed at CEA Grenoble by C. Chapelier and C. Tonnoir to study superconductivity induced in graphene by the

proximity of Re. A very high transparency for the Cooper pairs of the C/Re barrier was found in this system, allowing for the observation of a superconducting gap much similar to that in bare Re. This observation is a direct consequence of the strong interaction between a single layer of graphene and Re(0001) [194].

6 CONCLUSION AND PERSPECTIVES

6.1 GENERAL CONCLUSION

In this thesis, we have studied epitaxial graphene grown on different metal substrates, which may be used as platforms for developing new hybrid systems. Three systems have been studied: (i) graphene decoupled from an Ir(111) substrate by intercalated oxide ribbons, (ii) graphene on Ir(111) intercalated by (sub-) atomic layer Co, (iii) graphene on Re(0001). These three systems exhibit desirable features in the prospect of functional hybrid systems, with advanced electronic, magnetic, and superconducting properties respectively, as we will describe below.

As we have seen in the first chapter of this manuscript, depending on the nature of the metal, the strength of the graphene-metal interaction may vary, and the properties of graphene and of the metal may vary accordingly. This provided us with a turning knob for tuning the properties of graphene, and with this in mind we addressed weak interaction systems, graphene/Ir(111) a graphene/Ir(111) intercalated by an oxide, as well as stronger interaction systems, graphene/Ir(111) intercalated by Co, and graphene/Re(0001). Our review of the literature in chapter 1 also was an occasion to describe the types of defects which are encountered in typical graphene/metal systems (these defects are also found in other systems). In this work we decided to exploit these defects in order to control new intercalation pathways, which allowed us for instance to control the intercalation at local scale.

We have used a surface science approach to address the preparation and properties of graphene/metal systems, intercalated or not. First an *in situ* one relying on STM and RHEED; second a mixed *ex situ*/*in situ* one, combining STM, RHEED, AFM, Raman spectroscopy, and XPEEM. Whenever possible, we exploited the power of *in situ*, *in operando* microscopy (LEEM). This microscopy is quite versatile (suitable for imaging during Co deposition or under 10^{-7} mbar of a carbon precursor, at temperatures as high as 1475 K).

In chapter 3, we found that the interaction of oxygen with epitaxial graphene on iridium leads to the formation of an ultrathin oxide layer upon air exposure, extending between graphene and the metallic substrate via the graphene wrinkle. These wrinkles were shown to play a role as efficient diffusion channels for oxygen-containing species. The intercalated oxide is in the form of ribbons, whose thickness, length and width are typically 1.5 nm, several microns, and few 100 nm, respectively. The oxide ribbons were found to strongly modify the inelastic light scattering of graphene, which we showed is an evidence for a $10^{-12}\mathrm{cm}^{-2}$ change of charge carrier density in graphene, corresponding to a shift of about 200 meV of its Fermi level.

Chapter 4 described the intercalation process of Co thin layer between graphene and Ir. Upon mild annealing (400 K) of Co pre-deposited on graphene at room temperature, we found that Co intercalates more efficiently below those graphene domains having lower interactions with Ir(111), namely domains whose carbon zigzag rows do not align with the dense packed ones of the substrate. On all kind of graphene domains,

intercalation was moreover found to start at curved graphene regions, but surprisingly, distinctive types of curved graphene were found relevant depending on the kind of graphene domain. On graphene domains whose carbon zigzag rows aligning the Ir dense packed ones, Co intercalates on top of the substrate step edges, which are covered like a carpet by graphene, while on other kinds of graphene domains, wrinkles are the locations from where intercalation occurs.

Chapter 5 was devoted to another class of system based on strongly coupled graphene on Re(0001). We first studied bulk single crystals as substrates and found that none of the processes developed by other groups for growing graphene on metals with which it strongly interact (Ru, Rh) apply on Re(0001). We have thus employed a new growth method confined to the surface, which exploits the distinctive C adatom concentrations for carbide and graphene nucleation, and for equilibrium growth of carbide and graphene. This method consists in nucleating graphene with the help of high C adatom concentration, and to grow it far from equilibrium with still a high concentration. In practice, this consists in cycling low temperature adsorption of ethylene and high temperature flashes. Rhenium thin films on sapphire provided us with an alternative growth substrate, for which we found that a simple temperature-induced surface segregation of C dissolved into the thin film at high temperature, yielded prominently graphene on the surface. Besides the graphene phase we also identified other carbon phases, possibly a carbide and/or graphene bilayer, whose surface fraction increase with the C precursor dose. We finally found that the Raman signature of graphene is absent on Re(0001), as revealed by DFT calculations by looking for graphene Dirac cones, no trace of graphene linear dispersion was detected, which is another evidence of the strong interaction between graphene and Re(0001), .

6.2 PERSPECTIVES AND OPEN QUESTIONS

Further understanding graphene growth

While the growth of graphene single layers is relatively well-known, the growth of graphene multilayers still holds many of its secrets. How and where graphene layer beyond the first one grow is for instance only partially known. The same applies for the relative crystallographic orientation of successive graphene layers. With this in mind we have started the study of the growth of multilayer graphene on Re and Co foils. Once understood and controlled, these systems may allow to provide graphene with controlled and uniform number of layers, which would be transferred to any support after chemical etching of the metallic support. This approach, especially relevant in the case of Co foils (easily etched by chemicals), would provide a valuable alternative to the multi-transfer processes needed to prepare multilayers from Cu substrates.

Manipulation graphene's properties by intercalation

As we have seen a spontaneous intercalation of an oxide happens when graphene/Ir(111) with open wrinkle ends is exposed to air. On the one hand one may consider further promoting the intercalation in order to achieve thicker and full-layer oxides. On the other hand one may exploit the self-limitation of the width of the oxide ribbons in order to construct charge carrier density-modulated graphene structures, which have been

predicted to exhibit rich electronic spectrum, with electronic band gaps and anisotropic electronic band structures [160].

Further understanding Co intercalation, and new magnetic properties in graphene/Co/Ir

We have recently found that intercalation of Co, not from curved graphene regions as discussed in this manuscript, but from the edges of graphene islands, produces interesting effects in graphene. More work is needed to understand the energetics and kinetics of intercalation in this case, and to determine the role of strains and graphene-metal interaction in the intercalation process.

There have been interesting observation a magnetism induced in graphene by contact with Ni and Fe [10], and exciting proposals that such magnetism could be modulated at the nanoscale, inside the moiré [109]. Controlled intercalation, in high quality systems such as the ones we have developed, are well-suited for high sensitivity, maybe even local-scale, studies of magnetism in carbon. X-ray magnetic circular dichroism, combined or not with PEEM, and spin-polarized angle-resolved photoemission spectroscopy, are techniques of choice for addressing these issues.

Making graphene superconducting and probing the interface

Graphene is expected to be superconducting by proximity effect. Graphene/Re(0001) is a strongly coupled system and it was shown by our collaborators at CEA-INAC that this is valuable for achieving a highly transparent interface for Cooper pairs from Re to graphene, which makes graphene superconducting. However, as such, graphene/Re(0001) has its electronic properties deeply altered by the extended graphene-Re contact. In order to achieve both good contacts and free-standing contact, we envisage two solutions. The first one would consist in locally intercalating graphene/Re(0001), with oxygen species for instance. The second one would consist in addressing graphene samples on Re with a mixture of bilayer and monolayer regions: the topmost layer in bilayers is expected, as on Ru(0001) [88] to be quasi-free standing, but since growth by segregation is expected to proceed from below [53], this topmost layer should be in direct contact with the Re substrate in monolayer regions.

REFERENCE

[1] S. Bae, H. Kim, Y. Lee, X. Xu, J. S. Park, Y. Zheng, J. Balakrishnan, T. Lei, H. Ri Kim, Y. I. Song, Y. J. Kim, K. S. Kim, B. Özyilmaz, J. H. Ahn, B. H. Hong, and S. Iijima, "Roll-to-roll production of 30-inch graphene films for transparent electrodes," *Nature Nanotech.*, vol. 5, no. 8, pp. 574–578, 2010.

[2] Y. M. Lin, C. Dimitrakopoulos, K. A. Jenkins, D. B. Farmer, H. Y. Chiu, A. Grill, and P. Avouris, "100-ghz transistors from wafer-scale epitaxial graphene," *Science*, vol. 327, p. 662.

[3] C. Chen, S. Rosenblatt, K. I. Bolotin, W. Kalb, P. Kim, I. Kymissis, H. L. Stormer, T. F. Heinz, and J. Hone, "Performance of monolayer graphene nanomechanical resonators with electrical readout," *Nature Nano.*, vol. 4, p. 861, 2009.

[4] Z. Wu, W. Ren, L.Wen, L. Gao, J. Zhao, Z. Chen, G. Zhou, F. Li, and H. Cheng, "Graphene Anchored with Co_3O_4 Nanoparticles as Anode of Lithium Ion Batteries with Enhanced Reversible Capacity and Cyclic Performance," *ACS Nano.*, vol. 4, no. 6, pp. 3187–3194, 2010.

[5] C. Oshima and A. Nagashima, "Ultra-thin epitaxial films of graphite and hexagonal boron nitride on solid surfaces," *J. Phys.: Condens. Matter.*, vol. 9, no. 1, p. 1, 1997.

[6] A. T. N'Diaye, S. Bleikamp, P. J. Feibelman, and T. Michely, "Two-Dimensional Ir Cluster Lattice on a Graphene Moir on Ir(111)," *Phys. Rev. Lett.*, vol. 97, no. 21, p. 215501, 2006.

[7] J. Hwang, D. H. Lee, J. Y. Kim, T. H. Han, B. H. Kim, M. Park, K. Noa, and S. O. Kim, "Vertical zno nanowires/graphene hybrids for transparent and flexible field emission," *ACS Nano.*, vol. 21, no. 10, pp. 3432–3437, 2011.

[8] A. Tontegode, "Carbon on transition metal surfaces," *Prog. Surf. Sci*, vol. 38, no. 3-4, pp. 201–429, 1991.

[9] I. Pletikosić, M. Kralj, P. Pervan, R. Brako, J. Coraux, A. T. N'Diaye, C. Busse, and T. Michely, "Dirac Cones and Minigaps for Graphene on Ir(111)," *Phys. Rev. Lett.*, vol. 102, no. 5, p. 056808, 2009.

[10] Y. S. Dedkov, M. Fonin, and C. Laubschat, "A possible source of spin-polarized electrons: The inert graphene/Ni(111) system," *Appl. Phys. Lett.*, vol. 92, no. 5, pp. 052506–052509, 2008.

[11] A. Varykhalov, J. Sanchez-Barriga, A. M. Shikin, C. Biswas, E. Vescovo, A. Rybkin, D. Marchenko, and O. Rader, "Electronic and magnetic properties of quasifree-standing graphene on Ni," *Phys. Rev. Lett.*, vol. 101, no. 15, p. 157601, 2008.

[12] C. Vo-Van, S. Schumacher, J. Coraux, V. Sessi, O. Fruchart, N. B. Brookes, P. Ohresser, and T. Michely, "Magnetism of cobalt nanoclusters on graphene on iridium," *Appl. Phys. Lett.*, vol. 99, no. 14, pp. 142504–142504–3, 2011.

[13] J. Coraux, A. T. N'Diaye, N. Rougemaille, C. Vo-Van, A. Kimouche, H. X. Yang, M. Chshiev, N. Bendiab, O. Fruchart, and A. K. Schmid, "Air-protected epitaxial Graphene/Ferromagnet hybrids prepared by chemical vapor deposition and intercalation," *J. Phys. Chem. Lett.*, vol. 3, no. 15, pp. 2059–2063, 2012.

[14] J. Coraux, A. T. N'Diaye, C. Busse, and T. Michely, "Structural coherency of graphene on ir(111)," *Nano Lett.*, vol. 8, no. 2, pp. 565–570, 2008.

[15] C. Vo-Van, A. Kimouche, A. Reserbat-Plantey, O. Fruchart, P. Bayle-Guillemaud, N. Bendia, and J. Coraux, "Epitaxial graphene prepared by chemical vapor deposition on single crystal thin iridium films on sapphire," *Appl. Phys. Lett.*, vol. 98, no. 18, p. 181903, 2011.

[16] N. M. R. Peres, "Graphene, new physics in two dimensions," *Europhys. News*, vol. 40, no. 3, pp. 17–20, 2009.

[17] H. P. Boehm, A. Clauss, G. Fischer, and H. U, "Surface properties of extremelly thin graphite lamellae," *Proceedings of the fifth Conference on Carbon*, vol. 192, no. 4801, pp. 73–80, 1962.

[18] A. K. Geim and K. S. Novoselov, "The rise of graphene," *Nature Mater.*, vol. 6, no. 3, pp. 183–191, 2007.

[19] K. Novoselov, A. K. Geim, S. V. Morozov, D. Jiang, Y. Zhang, S. V. Dubonos, I. V. Grigorieva, and A. A. Firsov, "Electric field effect in atomically thin carbon films," *Science.*, vol. 306, no. 5696, pp. 666–669, 2004.

[20] A. H. C. Neto, F. Guinea, N. M. R. Peres, K. S. Novoselov, and A. K. Geim, "The electronic properties of graphene," *Rev. Mod. Phys.*, vol. 81, no. 1, pp. 109–162, 2009.

[21] K. S. Novoselov, A. K. Geim, S. V. Morozov, D. Jiang, M. I. Katsnelson, I. V. Grigorieva, S. V. Dubonos, and A. A. Firsov, "Two-dimensional gas of massless dirac fermions in graphene," *Nature*, vol. 438, no. 7065, pp. 197–200, 2005.

[22] Y. Zhang, Y. W. Tan, H. L. Stormer, and P. Kim, "Experimental observation of the quantum hall effect and Berry's phase in graphene," *Nature.*, vol. 438, no. 7065, pp. 201–204, 2005.

[23] A. Koma, "Van der Waals epitaxy-a new epitaxial growth method for a highly lattice-mismatched system," *Thin Solid Films*, vol. 216, no. 1, pp. 72–76, 2005.

[24] A. K. Geim, "Graphene: Status and prospects," *Science*, vol. 324, no. 5934, pp. 1530–1534, 2009.

[25] M. O. Goerbig, "Electronic properties of graphene in a strong magnetic field," *Rev. Mod. Phys.*, vol. 83, no. 4, pp. 1193–1243, 2011.

[26] P. R. Wallace, "The band theory of graphite," *Phys. Rev.*, vol. 71, no. 9, pp. 622–634, 1947.

[27] J. C. Slonczewski and P. R. Weiss, "Band structure of graphite," *Phys. Rev.*, vol. 109, no. 2, pp. 272–279, 1958.

[28] S. Reich, J. Maultzsch, and P. O. C. Thomsen, "Tight-binding description of graphene," *Phys. Rev. B*, vol. 66, no. 3, p. 035412, 2002.

[29] C. Bena and G. Montambaux, "Remarks on the tight-binding model of graphene," *New J. Phys.*, vol. 11, no. 9, p. 095003, 2009.

[30] L. Song, L. Ci, H. Lu, P. B. Sorokin, C. Jin, J. Ni, A. G. Kvashnin, D. G. Kvashnin, J. Lou, B. I. Yakobson, and P. M. Ajayan, "Large scale growth and characterization of atomic hexagonal boron nitride layers," *Nano Lett.*, vol. 10, no. 8, pp. 3209–3215, 2010.

[31] G. Eda, H. Yamaguchi, D. Voiry, T. Fujita, M. Chen, and M. Chhowalla, "Photoluminescence from chemically exfoliated MoS_2," *Nano Lett.*, vol. 11, no. 12, pp. 5111–5116, 2011.

[32] E. Y. Andrei, G. Li, and X. Du, "Electronic properties of graphene: a perspective from scanning tunneling microscopy and magnetotransport," *Rep. Prog. Phys.*, vol. 75, no. 5, p. 056501, 2012.

[33] G. Bertoni, L. Calmels, A. Altibelli, and V. Serin, "First-principles calculation of the electronic structure and EELS spectra at the graphene/Ni(111) interface," *Phys. Rev. B.*, vol. 71, no. 7, p. 075402, 2005.

[34] V. M. Karpan, G. Giovannetti, P. A. Khomyakov, M. Talanana, A. A. Starikov, M. Zwierzycki, J. van den Brink, G. Brocks, and P. J. Kelly, "Graphite and graphene as perfect spin filters," *Phys. Rev. Lett.*, vol. 99, no. 17, p. 176602, 2007.

[35] Y. Gamo, A. Nagashima, M. Wakabayashi, M. Terai, and C. Oshima, "Atomic structure of monolayer graphite formed on Ni(111)," *Surf. Sci.*, vol. 374, no. 1-3, pp. 61–64, 1997.

[36] R. Bistritzer and A. H. MacDonald, "Moir bands in twisted double-layer graphene," *PNAS.*, vol. 108, no. 30, 2011.

[37] T. A. Land, T. Michely, R. J. Behm, J. C. Hemminger, and G. Comsa, "STM investigation of single layer graphite structures produced on Pt(111) by hydrocarbon decomposition," *Surf. Sci.*, vol. 264, no. 3, pp. 261–270, 1992.

[38] G. T. Grant and T. W. Haas, "A study of Ru(0001) and Rh(111) surfaces using LEED and Auger electron spectroscopy," *Surf. Sci.*, vol. 21, no. 1, pp. 76–85, 1997.

[39] N. A. Vinogradov, A. A. Zakharov, V. Kocevski, J. Rusz, K. A. Simonov, O. Eriksson, A. Mikkelsen, E. Lundgren, A. S. Vinogradov, N. Martensson, and A. B. Preobrajenski, "Formation and Structure of Graphene Waves on Fe(110)," *Phys. Rev. Lett.*, vol. 109, no. 2, p. 026101, 2012.

[40] A. T. N'Diaye, J. Coraux, T. Plasa, C. Busse, and T. Michely, "Structure of epitaxial graphene on Ir(111)," *New J. Phys.*, vol. 10, no. 4, p. 043033, 2008.

[41] L. Gao, J. R. Guest, and N. P. Guisinger, "Epitaxial Graphene on Cu(111)," *Nano Lett.*, vol. 10, no. 9, pp. 3512–3516, 2010.

[42] P. W. Sutter, J. I. Flege, and E. A. Sutter, "Epitaxial graphene on ruthenium," *Nature Mater.*, vol. 7, no. 5, pp. 406–411, 2008.

[43] C. Busse, P. Lazić, R. Djemour, J. Coraux, T. Gerber, N. Atodiresei, V. Caciuc, R. Brako, A. T. N'Diaye, S. B. gel, J. Zegenhagen, and T. Michely, "Graphene on Ir(111): Physisorption with Chemical Modulation," *Phys. Rev. Lett.*, vol. 107, no. 3, p. 036101, 2011.

[44] N. Levy, and S. A. Burke, and K. L. Meaker, and M. Panlasigui, and A. Zettl, and F. Guinea, and A. H. Castro Neto, and M.F. Crommie, "Strain-Induced Pseudo-Magnetic Fields Greater Than 300 Tesla in Graphene Nanobubbles," *Science*, vol. 329, no. 5991, pp. 544–547, 2010.

[45] H. Yan, Y. Sun, L. He, J. C. Nie, and M. H. W. Chan, "Observation of landau-level-like quantization at 77 k along a strained-induced graphene ridge," *Phys. Rev. B*, vol. 85, no. 3, p. 035422, 2012.

[46] J. Lahiri, Y. Lin, P. Bozkurt, I. I. Oleynik, and M. Batzill, "An extended defect in graphene as a metallic wire," *Nature Nano.*, vol. 5, no. 5, pp. 326–329, 2010.

[47] H. Terrones, R. Lv, M. Terrones, and M. S. Dresselhaus, "The role of defects and doping in 2D graphene sheets and 1D nanoribbons," *Rep. Prog. Phys.*, vol. 75, no. 6, p. 062501, 2012.

[48] J. Kotakoski, J. C. Meyer, S. Kurasch, D. Santos-Cottin, U. Kaiser, and A. V. Krasheninnikov, "Stone-wales-type transformations in carbon nanostructures driven by electron irradiation," *Phys. Rev. B.*, vol. 83, no. 24, p. 245420, 2011.

[49] G. Lee, C. Z. Wang, E. Yoon, N. M. Hwang, D. Y. Kim, and K. M. Ho, "Diffusion, coalescence, and reconstruction of vacancy defects in graphene layers," *Phys. Rev. Lett.*, vol. 95, no. 20, p. 205501, 2005.

[50] V. A. Coleman, R. Knut, O. Karis, H. Grennberg, U. Jansson, R. Quinlan, B. C. Holloway, B. Sanyal, and O. Eriksson, "Defect formation in graphene nanosheets by acid treatment: an x-ray absorption spectroscopy and density functional theory study," *J. Phys. D: Appl. Phys.*, vol. 41, no. 6, p. 062001, 2008.

[51] J. J. Palacios, J. Fernández-Rossier, and L. Brey, "Vacancy-induced magnetism in graphene and graphene ribbons," *Phys. Rev. B.*, vol. 77, no. 19, p. 195428, 2008.

[52] J. Ma, D. Alfe, A. Michaelides, and E. Wang, "Stone-wales defects in graphene and other planar sp^2-bonded materials," *Phys. Rev. B.*, vol. 80, no. 3, p. 033407, 2009.

[53] E. Loginova, N. C. Bartelt, P. J. Feibelman, and K. F. McCarty, "Factors influencing graphene growth on metal surfaces," *New J. Phys.*, vol. 11, no. 6, p. 063046, 2009.

[54] J. Coraux, A. T. N'Diaye, M. Engler, C. Busse, D. Wall, N. Buckanie, F. J. M. zu Heringdorf, R. van Gastel, B. Poelsema, and T. Michely, "Growth of graphene on Ir(111)," *New J. Phys.*, vol. 11, no. 2, p. 023006, 2009.

[55] V. Derycke, R. Martel, M. Radosavljević, F. M. Ross, and P. Avouris, "Catalyst-Free Growth of Ordered Single-Walled Carbon Nanotube Networks," *Nano Lett.*, vol. 2, no. 10, pp. 143–146, 2002.

[56] V. Derycke, R. Martel, M. Radosavljević, F. M. Ross, and P. Avouris, "Structure and electronic transport in graphene wrinkles," *Nano Lett.*, vol. 12, no. 7, pp. 3431–3436, 2012.

[57] A. T. N'Diaye, R. van Gastel, A. G. Martinez-Galera, J. Coraux, H. Hattab, D. Wll, F. J. M. zu Heringdorf, M. H. von Hoegen, B. Poelsema, C. Busse, and T. Michely, "*In situ* observation of stress relaxation in epitaxial graphene," *New J. Phys.*, vol. 11, no. 10, p. 113056, 2009.

[58] G. Eda, G. Fanchini, and M. Chhowalla., "Large-area ultrathin films of reduced graphene oxide as a transparent and flexible electronic material," *Nature Nanotech.*, vol. 3, no. 5, pp. 270–274, 2008.

[59] Z. Yin, S. Sun, T. Salim, S. Wu, X. Huang, Q. He, Y. M. Lam, and H. Zhang, "Organic photovoltaic devices using highly flexible reduced graphene oxide films as transparent electrodes," *ACS Nano.*, vol. 4, no. 9, pp. 5263–5268, 2010.

[60] K. V. Emtsev, A. Bostwick, K. Horn, J. Jobst, G. L. Kellogg, L. Ley, J. L. McChesney, T. Ohta, S. A. Reshanov, J. Röhrl1, E. Rotenberg, A. K. Schmid, D. Waldmann, H. B. Weber, and T. Seyller, "Towards wafer-size graphene layers by atmospheric pressure graphitization of silicon carbide," *Nature Nanotech.*, vol. 8, no. 3, pp. 203–207, 2009.

[61] A. Reina, X. Jia, J. Ho, D. Nezich, H. Son, V. Bulovic, M. S. Dresselhaus, and J. Kong, "Structure and electronic transport in graphene wrinkles," *Nano Lett.*, vol. 9, no. 1, pp. 30–35, 2009.

[62] K. S. Kim, Y. Zhao, H. Jang, S. Y. Lee, J. M. Kim, K. S. Kim, J. H. Ahn, P. Kim, J. Y. Choi, and B. H. Hong, "Large-scale pattern growth of graphene films for stretchable transparent electrodes," *Nature.*, vol. 457, no. 7230, pp. 706–710, 2009.

[63] X. Li, W. Cai, J. An, S. Kim, J. Nah, D. Yang, R. Piner, A. Velamakanni, I. Jung, E. Tutuc, S. K. Banerjee, L. Colombo, and R. S. Ruoff, "Large-area synthesis of high-quality and uniform graphene films on copper foils," *Science.*, vol. 324, no. 5932, pp. 1312–1314, 2009.

[64] W. J. Arnoult and R. B. McLellan, "The solubility of carbon in rhodium ruthenium, iridium and rhenium," *Scr. Metall.*, vol. 6, no. 10, pp. 1013–1018, 1972.

[65] B. C. Banarjee, "Pyrolytic carbon formation from carbon suboxide," *Nature.*, vol. 192, no. 4801, pp. 450–451, 1961.

[66] E. Loginova, N. C. Bartelt, P. J. Feibelman, and K. F. McCarty, "Evidence for graphene growth by c cluster attachment," *New J. Phys.*, vol. 10, no. 9, p. 093026, 2008.

[67] P. Sutter, J. T. Sadowski, and E. Sutter, "Graphene on Pt(111): Growth and substrate interaction," *Phys. Rev. B*, vol. 80, no. 24, p. 245411, 2009.

[68] F. Abild-Pedersen, J. K. Norskov, J. Rostrup-Nielsen, J. Sehested, and S. Helveg, "Mechanisms for catalytic carbon nanofiber growth studied by ab initio density functional theory calculations," *Phys. Rev. B.*, vol. 73, no. 11, p. 115419, 2006.

[69] H. Chen, W. Zhu, and Z. Zhang, "Contrasting behavior of carbon nucleation in the initial stages of graphene epitaxial growth on stepped metal surfaces," *Phys. Rev. Lett.*, vol. 104, no. 18, p. 186101, 2010.

[70] S. Saadi, F. Abild-Pedersen, S. Helveg, J. Sehested, B. Hinnemann, C. C. Appel, and J. K. Norskov, "On the role of metal step-edges in graphene growth," *J. Phys. Chem. C.*, vol. 114, no. 25, pp. 11221–11227, 2010.

[71] J. Gao, J. Yip, J. Zhao, B. I. Yakobson, and F. Ding, "Graphene nucleation on transition metal surface: Structure transformation and role of the metal step edge," *J. Am. Chem. Soc.*, vol. 133, pp. 5009–5015, Apr. 2011.

[72] J. M. Wofford, S. Nie, K. F. McCarty, N. C. Bartelt, and O. D. Dubon, "Graphene islands on cu foils: The interplay between shape, orientation, and defects," *Nano Lett.*, vol. 10, no. 12, pp. 4890–4896, 2010.

[73] M. Massicotte, V. Yu, E. Whiteway, D. Vatnik, and M. Hilke, "Quantum hall effect in fractal graphene: growth and properties of graphlocons," *New. J. Phys.*, vol. 24, no. 32, p. 325601, 2013.

[74] S. Nie, W. Wu, S. Xing, Q. Yu, J. Bao, S. Pei, and K. F. McCarty, "Growth from below: bilayer graphene on copper by chemical vapor deposition," *New. J. Phys.*, vol. 14, no. 9, pp. 093028–093036, 2009.

[75] Z. Han, A. Kimouche, D.Kalita, A. Allain, H. Arjmandi-Tash, A. Reserbat-Plantey, L. Marty, S. Pairis, V. Raita, N. Bendiab, J. Coraux, and V. Bouchiat, "Homogeneous optical and electronic properties of graphene due to the suppression of multilayer patches during cvd on copper foils." 2013.

[76] J. C. Shelton, H. R. Patil, and J. M. Blakely, "Equilibrium segregation of carbon to a nickel (111) surface: A surface phase transition," *Surf. Sci.*, vol. 43, no. 2, pp. 493–520, 1974.

[77] K. F. McCarty, P. J. Feibelman, E. Loginova, and N. C. Bartelt, "Kinetics and thermodynamics of carbon segregation and graphene growth on Ru(0001)," *Carbon.*, vol. 47, no. 7, pp. 1806–1813, 2009.

[78] G. Giovannetti, P. A. Khomyakov, G. Brocks, V. M. Karpan, J. van den Brink, and P. J. Kelly, "Doping graphene with metal contacts," *Phys. Rev. Lett.*, vol. 101, no. 2, p. 026803, 2008.

[79] B. Hammer and J. K. Norskov, "Theoretical Surface Science and Catalysis. Calculations and Concepts," *Adv Catal.*, vol. 45, pp. 71–129, 2000.

[80] M. Batzill, "The surface science of graphene: Metal interfaces, cvd synthesis, nanoribbons, chemical modifications, and defects," *Surf. Sci. Rep.*, vol. 67, no. 3–4, pp. 83–115, 2012.

[81] B. Wang, M. L. Bocquet, S. Marchini, S. Günther, and J. Wintterlin, "Chemical origin of a graphene moir overlayer on Ru(0001)," *Phys. Chem. Chem. Phys.*, vol. 10, no. 24, pp. 3530–3534, 2008.

[82] E. N. Voloshina, E. Fertitta, A. Garhofer, F. Mittendorfer, M. Fonin, A. Thissen, and Y. S. Dedkov, "Electronic structure and imaging contrast of graphene moiré on metals," *Sci. Rep.*, vol. 3, no. 172, pp. 1–7, 2013.

[83] S. Marchini, S. Günther, and J. Wintterlin, "Scanning tunneling microscopy of graphene on Ru(0001)," *Phys. Rev. B*, vol. 76, no. 7, p. 075429, 2007.

[84] A. B. Preobrajenski, M. L. Ng, A. S. Vinogradov, and N. Mȧrtensson, "Controlling graphene corrugation on lattice-mismatched substrates," *Phys. Rev. B*, vol. 78, no. 7, p. 073401, 2008.

[85] D. Martoccia, P. R. Willmott, T. Brugger, M. Björck, S. Günther, C. M. Schlepütz, A. Cervellino, S. A. Pauli, B. D. Patterson, S. Marchini, J. Wintterlin, W. Moritz, and T. Greber, "Graphene on Ru(0001): A 25× 25 Supercell," *Phys. Rev. Lett.*, vol. 101, no. 12, p. 126102, 2008.

[86] S. Stradi, S. Barja, C. Diaz, M. Garnica, B. Borca, J. J. Hinarejos, D. Sanchez-Portal, M. Alcami, A. Arnau, A. L. V. de Parga, R. Miranda, and F. Martin, "Role of dispersion forces in the structure of graphene monolayers on ru surfaces," *Phys. Rev. Lett.*, vol. 106, no. 18, p. 186102, 2011.

[87] A. Grũneis and D. F. Vyalikh, "Tunable hybridization between electronic states of graphene and a metal surface," *Phys. Rev. B.*, vol. 77, no. 19, p. 193401, 2009.

[88] P. Sutter, M. S. Hybertsen, J. T. Sadowski, and E. Sutter, "Electronic Structure of Few-Layer Epitaxial Graphene on Ru(0001)," *Nano Lett.*, vol. 9, no. 7, pp. 2654–2660, 2009.

[89] T. Ohta, A. Bostwick, T. Seyller, K. Horn, and E. Rotenberg, "Controlling the electronic structure of bilayer graphene," *Science.*, vol. 313, no. 5789, pp. 951–954, 2006.

[90] A. L. V. de Parga, F. Calleja, B. Borca, M. C. G. Passeggi, J. J. Hinarejos, F. Guinea, and R. Miranda, "Periodically rippled graphene: Growth and spatially resolved electronic structure," *Phys. Rev. Lett.*, vol. 100, no. 5, p. 056807, 2008.

[91] M. Lopes, A. Candini, M. Urdampilleta, A. Reserbat-Plantey, V. Bellini, S. Klyatskaya, L. Marty, M. Ruben, M. Affronte, W. Wernsdorfer, and N. Bendiab, "Surface-Enhanced Raman Signal for Terbium Single-Molecule Magnets Grafted on Graphene," *ACS Nano.*, vol. 4, no. 12, pp. 7531–7537, 2010.

[92] H. Zhang, C. Lazo, and Y. M. S. Blügel, Stefan. Heinze, "Electrically tunable quantum anomalous hall effect in graphene decorated by 5d transition-metal adatoms," *Phys. Rev. Lett.*, vol. 108, no. 5, p. 056802, 2012.

[93] C. Võ-Văn, Z. Kassir-Bodon, H. Yang, J. Coraux, J. Vogel, S. Pizzini, P. Bayle-Guillemaud, M. Chshiev, L. Ranno, V. Guisset, P. David, V. Salvador, and O. Fruchart, "Ultrathin epitaxial cobalt films on graphene for spintronic investigations and applications," *New J. Phys.*, vol. 12, no. 10, p. 103040, 2010.

[94] M. Sicot, S. Bouvron, O. Zander, U. Rüdiger, Y. S. Dedkov, and M. Fonin, "Nucleation and growth of nickel nanoclusters on graphene Moire on Rh(111)," *Appl. Phys. Lett.*, vol. 96, no. 9, p. 093115, 2010.

[95] K. Donner and P. Jakob, "Structural properties and site specific interactions of Pt with the graphene/Ru(0001) moir overlayer," *New. J. Phys.*, vol. 131, no. 16, pp. 164701–164711, 2009.

[96] P. J. Feibelman, "Pinning of graphene to Ir(111) by flat Ir dots," *Phys. Rev. B.*, vol. 77, no. 16, p. 165419, 2008.

[97] J. Knudsen, P. J. Feibelman, T. Gerber, E. Granäs, K. Schulte, P. Stratmann, J. N. Andersen, and T. Michely, "Clusters binding to the graphene moiré on Ir(111): X-ray photoemission compared to density functional calculations," *Phys. Rev. B*, vol. 85, no. 3, p. 035407, 2012.

[98] S. Rusponi, M. Papagno, P. Moras, S. Vlaic, M. Etzkorn, P. M. Sheverdyaeva, D. Pacilé, H. Brune, and C. Carbone, "Highly anisotropic dirac cones in epitaxial graphene modulated by an island superlattice," *Phys. Rev. Lett.*, vol. 105, no. 24, p. 246803, 2010.

[99] H. Chen, Q. Niu, Z. Zhang, and A. H. MacDonald, "Gate-tunable exchange coupling between cobalt clusters on graphene," *Phys. Rev. B.*, vol. 87, no. 14, p. 144410, 2013.

[100] A. J. Pollard, E. W. Perkins, N. A. Smith, A. Saywell, G. Goretzki, A. G. Phillips, S. P. Argent, H. Sachdev, F. Müller, S. Hüfner, S. Gsell, M. Fischer, M. Schreck, J. Osterwalder, T. Greber, S. Berner, N. R. Champness, and P. H. Beton, "Supramolecular assemblies formed on an epitaxial graphene superstructure," *Angew. Chem.*, vol. 49, no. 10, pp. 1794–1799, 2010.

[101] M. Garnica, D. Stradi, S. Barja, F. Calleja, C. Diaz, M. Alcami, N. Martin, A. L. V. de Parga, F. Martin, and R. Miranda, "Long-range magnetic order in a purely organic 2d layer adsorbed on epitaxial graphene," *Nature Phys.*, vol. 9, no. 6, pp. 368–374, 2013.

[102] R. Balog, B. Jrgensen, L. Nilsson, M. Andersen, E. Rienks, M. Bianchi, M. Fanetti, E. Lgsgaard, A. Baraldi, S. Lizzit, Z. Sljivancanin, F. Besenbacher, B. Hammer, T. G. Pedersen, P. Hofmann, and L. Hornekr, "Bandgap opening in graphene induced by patterned hydrogen adsorption," *Nature Mater.*, vol. 9, no. 4, pp. 315–319.

[103] M. S. Dresselhaus and G. Dresselhaus, "Intercalation compounds of graphite," *Adv. Phys.*, vol. 30, no. 2, pp. 1–186, 1981.

[104] P. Sutter, J. T. Sadowski, and E. A. Sutter, "Chemistry under cover: Tuning metal-graphene interaction by reactive intercalation," *J. Am. Chem. Soc.*, vol. 132, no. 23, pp. 8175–8179, 2010.

[105] E. Grnäs, J. Knudsen, U. A. Schräder, T. Gerber, C. Busse, a. S. M. A. Arman, J. N. Andersen, and T. Michely, "Oxygen Intercalation under Graphene on Ir(111): Energetics, Kinetics, and the Role of Graphene Edges," *ACS Nano.*, vol. 6, no. 11, pp. 9951–9963, 2012.

[106] S. Lizzit, R. Larciprete, P. Lacovig, M. Dalmiglio, F. Orlando, A. Baraldi, L. Gammelgaard, L. Barreto, M. Bianchi, E. Perkins, and P. Hofmann, "Transfer-free electrical insulation of epitaxial graphene from its metal substrate," *Nano Lett.*, vol. 12, no. 9, pp. 4503–4507, 2012.

[107] A. Varykhalov, D. Marchenko, M. R. Scholz, E. D. L. Rienks, T. K. Kim, G. Bihlmayer, J. Sánchez-Barriga, and O. Rader, "Ir(111) Surface State with Giant Rashba Splitting Persists under Graphene in Air," *Phys. Rev. Lett.*, vol. 108, no. 6, p. 066804, 2012.

[108] N. Rougemaille, A. T. N'Diaye, J. Coraux, C. Vo-Van, O. Fruchart, and A. K. Schmid, "Perpendicular magnetic anisotropy of cobalt films intercalated under graphene," *Appl. Phys. Lett*, vol. 101, no. 14, pp. 142403–142403–3, 2012.

[109] R. Decker, J. Brede, N. Atodiresei, V. Caciuc, S. Blügel, and R. Wiesendanger, "Atomic-scale magnetism of cobalt-intercalated graphene," *Phys. Rev. B.*, vol. 87, no. 4, p. 041403, 2013.

[110] M. S. Dresselhaus, "Fifty years in studying carbon-based materials," *Phys. Scr.*, vol. 2012, no. 146, p. 014002, 2012.

[111] M. A. Pimenta, G. Dresselhaus, M. S. Dresselhaus, L. G. Cancado, A. Jorio, and R. Saito, "Studying disorder in graphite-based systems by raman spectroscopy," *Phys. Chem. Chem. Phys.*, vol. 9, no. 11, pp. 1276–1290, 2007.

[112] L. Cancado, K. Takai, T. Enoki, M. Endo, Y. Kim, H. Mizusaki, N. Speziali, A. Jorio, and M. Pimenta, "Measuring the degree of stacking order in graphite by raman spectroscopy," *Carbon.*, vol. 46, no. 2, pp. 272–275, 2008.

[113] A. C. Ferrari, J. C. Meyer, V. Scardaci, C. Casiraghi, M. Lazzeri, F. Mauri, S. Piscanec, D. Jiang, K. S. Novoselov, S. Roth, and A. K. Geim, "Raman spectrum of graphene and graphene layers," *Phys. Rev. Lett.*, vol. 97, no. 18, p. 187401, 2006.

[114] C. H. Lui, Z. Li, Z. Chen, P. V. Klimov, L. E. Brus, and T. F. Heinz, "Imaging stacking order in few-layer graphene," *Nano Lett.*, vol. 11, no. 1, pp. 164–169, 2011.

[115] M. Huang, H. Yan, C. Chen, D. Song, T. F. Heinz, and J. Hone, "Phonon softening and crystallographic orientation of strained graphene studied by raman spectroscopy," *PNAS.*, vol. 106, no. 18, pp. 7304–7308, 2009.

[116] S. Pisana, M. Lazzeri, C. Casiraghi, K. S. Novoselov, A. K. Geim, A. C. Ferrari, and F. Mauri, "Breakdown of the adiabatic Born-Oppenheimer approximation in graphene," *Nat Mater.*, vol. 6, no. 3, pp. 198–201, 2007.

[117] L. Malard, M. Pimenta, G. Dresselhaus, and M. Dresselhaus, "Raman spectroscopy in graphene," *Phys. Rep.*, vol. 473, no. 5–6, pp. 51–87, 2009.

[118] A. Eckmann, A. Felten, I. Verzhbitskiy, R. Davey, and C. Casiraghi, "Raman study on defective graphene: Effect of the excitation energy, type, and amount of defects," *Phys. Rev. B.*, vol. 88, p. 035426, 2013.

[119] J. Yan, Y. Zhang, P. Kim, and A. Pinczuk, "Electric field effect tuning of electron-phonon coupling in graphene," *Phys. Rev. Lett.*, vol. 98, p. 166802, 2007.

[120] A. Das, S. Pisana, B. Chakraborty, S. Piscanec, S. K. Saha, U. V. Waghmare, K. S. Novoselov, H. R. Krishnamurthy, A. K. Geim, A. C. Ferrari, and A. K. Sood, "Monitoring dopants by Raman scattering in an electrochemically top-gated graphene transistor," *Nature Nanotech.*, vol. 3, no. 4, pp. 210–215, 2008.

[121] T. M. G. Mohiuddin, A. Lombardo, R. R. Nair, A. Bonetti, G. Savini, R. Jalil, N. Bonini, D. M. Basko, C. Galiotis, N. Marzari, K. S. Novoselov, A. K. Geim, and A. C. Ferrari, "Uniaxial strain in graphene by raman spectroscopy: g peak splitting, grüneisen parameters, and sample orientation," *Phys. Rev. B.*, vol. 79, p. 205433, 2009.

[122] G. Binnig, C. F. Quate, and C. Gerber, "Atomic force microscope," *Phys. Rev. Lett.*, vol. 56, no. 9, pp. 930–933, 1986.

[123] R. Garcia and R. Perez, "Dynamic atomic force microscopy methods," *Surf. Sci. Reports.*, vol. 47, no. 6–8, pp. 197–301, 2002.

[124] F. J. Giessibl, "Advances in atomic force microscopy," *Rev. Mod. Phys.*, vol. 75, no. 3, pp. 949–983, 2003.

[125] M. L. Bolen, S. E. Harrison, L. B. Biedermann, and M. A. Capano, "Graphene formation mechanisms on 4H-SiC(0001)," *Phys. Rev. B.*, vol. 80, no. 11, p. 115433, 2009.

[126] H. Hibino, H. Kageshima, and M. Nagase, "Epitaxial few-layer graphene: towards single crystal growth," *J. Phys. D: Appl. Phys.*, vol. 43, no. 37, p. 374005, 2010.

[127] G. Binnig, H. Rohrer, C. Gerber, and E. Weibel, "Theory of scanning tunneling spectroscopy," *Appl. Phys. Lett.*, vol. 40, no. 2, p. 178, 1982.

[128] C. J. Chen, "Theory of scanning tunneling spectroscopy," *J. Vac. Sci. Technol.*, vol. 6, no. 2, p. 319, 1988.

[129] F. Watanabe, S. Kodambaka, W. Swiech, J. Greene, and D. G. Cahill, "LEEM study of island decay on Si(110)," *Surf. Sci.*, vol. 572, no. 2–3, pp. 425–432, 2004.

[130] E. Bauer, "Low energy electron microscopy," *Rep. Prog. Phys.*, vol. 57, no. 9, p. 895, 1994.

[131] N. Rougemaille and A. K. Schmid, "Magnetic imaging with spin-polarized low-energy electron microscopy," *Eur Phys J-Appl Phys.*, vol. 50, no. 2, p. 20101, 2010.

[132] F. Bonaccorso, A. Lombardo, T. Hasan, Z. Sun, L. Colombo, and A. C. Ferrari, "Production and processing of graphene and 2d crystals," *Mater. Today.*, vol. 15, no. 12, pp. 564–589, 2012.

[133] Y. Wu, K. A. Jenkins, A. Valdes-Garcia, D. B. Farmer, Y. Zhu, A. A. Bol, C. Dimitrakopoulos, W. Zhu, F. Xia, P. Avouris, and Y. M. Lin, "State-of-the-art graphene high-frequency electronics," *Nano Lett.*, vol. 12, no. 6, pp. 3062–3067, 2012.

[134] A. Varykhalov, M. R. Scholz, T. K. Kim, and O. Rader, "Effect of noble-metal contacts on doping and band gap of graphene," *Phys. Rev. B.*, vol. 82, no. 12, p. 121101, 2010.

[135] Y. S. Dedkov and M. Fonin, "Electronic and magnetic properties of the graphene ferromagnet interface," *New J. Phys.*, vol. 12, no. 12, p. 125004, 2010.

[136] S. Schumacher, D. F. Förster, M. Rösner, T. O. Wehling, and T. Michely, "Strain in epitaxial graphene visualized by intercalation," *Phys. Rev. Lett.*, vol. 110, no. 8, p. 086111, 2013.

[137] M. Sicot, P. Leicht, A. Zusan, S. Bouvron, O. Zander, M. Weser, Y. S. Dedkov, K. Horn, and M. Fonin, "Size-Selected Epitaxial Nanoislands Underneath Graphene Moiré on Rh(111)," *ACS Nano.*, vol. 6, no. 1, pp. 151–158, 2012.

[138] R. van Gastel, A. T. N'Diaye, D. Wall, J. Coraux, C. Busse, N. M. Buckanie, F. J. Meyer zu Heringdorf, M. Horn von Hoegen, T. Michely, and B. Poelsema, "Selecting a single orientation for millimeter sized graphene sheets," *Appl. Phys. Lett.*, vol. 95, no. 12, pp. 121901–121901–3, 2009.

[139] H. Hattab, A. T. N'Diaye, D. Wall, G. Jnawali, J. Coraux, C. Busse, R. van Gastel, B. Poelsema, T. Michely, F. J. M. zu Heringdorf, and M. H. von Hoegen, "Growth temperature dependent graphene alignment on Ir(111)," *Appl. Phys. Lett.*, vol. 98, no. 14, pp. 141903–141907, 2011.

[140] J. Hofrichter, B. N. Szafranek, M. Otto, T. J. Echtermeyer, M. Baus, A. Majerus, V. Geringer, M. Ramsteiner, and H. Kurz, "Synthesis of graphene on silicon dioxide by a solid carbon source," *Nano Lett.*, vol. 10, no. 1, pp. 36–42, 2010.

[141] D. A. Schmidt, T. Ohta, and T. E. Beechem, "Strain and charge carrier coupling in epitaxial graphene," *Phys. Rev. B.*, vol. 84, no. 23, p. 235422, 2011.

[142] S. C. Martin, B. Sacépé, S. Samaddar, A. Kimouche, J. Coraux, H. Courtois, and C. B. Winkelmann, "Ripples and charge puddles in screened graphene," arXiv e-print 1304.1183, 2013.

[143] P. Avouris, T. Hertel, and R. Martel, "Atomic force microscope tip-induced local oxidation of silicon: kinetics, mechanism, and nanofabrication," *Appl. Phys. Lett.*, vol. 71, no. 2, pp. 285–287, 1997.

[144] B. R. Chalamala, Y. Wei, R. H. Reuss, S. Aggarwal, B. E. Gnade, R. Ramesh, J. M. Bernhard, E. D. Sosa, and D. E. Golden, "Effect of growth conditions on surface morphology and photoelectric work function characteristics of iridium oxide thin films," *Appl. Phys. Lett.*, vol. 74, no. 10, pp. 1394–1396, 1999.

[145] Y. B. He, A. Stierle, W. X. Li, A. Farkas, N. Kasper, and H. Over, "Oxidation of Ir(111): From O–Ir–O Trilayer to Bulk Oxide Formation," *J. Phys. Chem. C.*, vol. 112, no. 31, pp. 11946–11953, 2008.

[146] M. Escher, K. Winkler, O. Renault, and N. Barrett, "Applications of high lateral and energy resolution imaging XPS with a double hemispherical analyser based spectromicroscope," *J. Electron. Spectrosc. Relat. Phenom.*, vol. 178–179, pp. 303–316, 2010.

[147] E. V. Rut'kov and A. Tontegode, "A study of the carbon adlayer on iridium," *Surf. Sci.*, vol. 161, no. 2–3, pp. 373–389, 1985.

[148] O. Renault, R. Brochier, A. Roule, P. H. Haumesser, B. Krömker, and D. Funnemann, "Work-function imaging of oriented copper grains by photoemission," *Surf. Interface Anal.*, vol. 38, no. 4, p. 375, 2006.

[149] A. Bailly, O. Renault, N. Barrett, L. F. Zagonel, P. Gentile, N. Pauc, F. Dhalluin, T. Baron, A. Chabli, J. C. Cezar, and N. B. Brookes, "Direct Quantification of Gold along a Single Si Nanowire," *Nano Lett.*, vol. 8, no. 11, pp. 3709–3714, 2008.

[150] A. Kimouche, O. Renault, S. Samaddar, C. Winkelmann, H. Courtois, O. Fruchart, and J. Coraux, "Modulating charge density and inelastic optical response in graphene by atmospheric pressure localized intercalation through wrinkles," *Carbon. In press*, 2013.

[151] Y. Zhang, V. W. Brar, C. Girit, A. Zettl, and M. F. Crommie, "Origin of spatial charge inhomogeneity in graphene," *Nature Phys.*, vol. 5, no. 10, pp. 722–726, 2009.

[152] V. Geringer, M. Liebmann, T. Echtermeyer, S. Runte, M. Schmidt, R. Rückamp, M. C. Lemme, and M. Morgenstern, "Intrinsic and extrinsic corrugation of monolayer graphene deposited on SiO_2," *Phys. Rev. Lett.*, vol. 102, no. 7, p. 076102, 2009.

[153] M. M. Ugeda, D. Fernandez-Torre, I. Brihuega, P. Pou, A. J. Martinez-Galera, R. Perez, and J. M. Gomez-Rodriguez, "Point defects on graphene on metals," *Phys. Rev. Lett.*, vol. 107, no. 11, p. 116803, 2011.

[154] M. Gao, Y. Pan, L. Huang, H. Hu, L. Z. Zhang, H. M. Guo, S. X. Du, and H. J. Gao, "Epitaxial growth and structural property of graphene on Pt(111)," *Appl. Phys. Lett.*, vol. 98, no. 3, pp. 033101–033104, 2011.

[155] E. Starodub, N. C. Bartelt, and K. F. McCarty, "Oxidation of graphene on metals," *J. Phys. Chem. C.*, vol. 114, no. 11, pp. 5134–5140, 2010.

[156] I. Schmitz, M. Schreiner, G. Friedbacher, and M. Grasserbauer, "Phase imaging as an extension to tapping mode AFM for the identification of material properties on humidity-sensitive surfaces," *Appl. Surf. Sci.*, vol. 115, no. 2, pp. 190–198, 1997.

[157] J. Tamayo and R. Garcia, "Effects of elastic and inelastic interactions on phase contrast images in tapping-mode scanning force microscopy," *Appl. Phys. Lett.*, vol. 71, no. 16, pp. 2394–2396, 1997.

[158] D. Ma, Y. Zhang, M. Liu, Q. Ji, T. Gao, Y. Zhang, and Z. Liu, "Clean transfer of graphene on pt foils mediated by a carbon monoxide intercalation process," *Nano Res. Accepted*, pp. 1–8.

[159] V. V. Cheianov, V. Falko, and B. L. Altshuler, "The Focusing of Electron Flow and a Veselago Lens in Graphene p-n Junctions," *Science.*, vol. 315, no. 5816, pp. 1252–1255, 2007.

[160] C. H. Park, Y. W. Son, L. Yang, M. L. Cohen, and S. G. Louie, "Electron beam supercollimation in graphene superlattices," *Nano Lett.*, vol. 8, no. 9, pp. 2920–2924, 2008.

[161] Y. Dedkov, A. M. Shikin, V. K. Adamchuk, S. L. Molodtsov, C. Laubschat, A. Bauer, and G. Kaindl, "Intercalation of copper underneath a monolayer of graphite on Ni(111)," *Phys. Rev. B.*, vol. 64, p. 035405, 2001.

[162] D. Pacilé, P. Leicht, M. Papagno, P. M. Sheverdyaeva, P. Moras, C. Carbone, K. Krausert, L. Zielke, M. Fonin, Y. S. Dedkov, F. Mittendorfer, J. Doppler, A. Garhofer, and J. Redinger, "Artificially lattice-mismatched graphene/metal interface: Graphene/Ni/Ir(111)," *Phys. Rev. B.*, vol. 87, no. 3, p. 035420, 2013.

[163] M. Weser, E. N. Voloshina, K. Horn, and Y. S. Dedkov, "Electronic structure and magnetic properties of the graphene/Fe/Ni(111) intercalation-like system," *Phys. Chem. Chem. Phys.*, vol. 13, no. 16, pp. 7534–7539, 2011.

[164] A. Nagashima, N. Tejima, and C. Oshima, "Electronic states of the pristine and alkali-metal-intercalated monolayer graphite/Ni(111) systems," *Phys. Rev. B*, vol. 50, no. 23, pp. 17487–17495, 1994.

[165] N. J. Wu and A. Ignatiev, "Potassium absorption into the graphite (0001) surface: Intercalation," *Phys. Rev. B.*, vol. 28, p. 7288, 1983.

[166] L. Huang, Y. Pan, L. Pan, M. Gao, W. Xu, Y. Que, H. Zhou, Y. Wang, S. Du, and H. J. Gao, "Intercalation of metal islands and films at the interface of epitaxially grown graphene and Ru(0001) surfaces," *Appl. Phys. Lett.*, vol. 99, p. 163107, 2011.

[167] L. Jin, Q. Fu, Y. Yang, and X. Bao, "A comparative study of intercalation mechanism at graphene/Ru(0001) interface," *Surf. Sci.*, p. in press, 2013.

[168] A monolayer is defined as the first atomic layer of Co that grows pseudo- morphically on Ir(111).

[169] A. Locatelli, L. Aballe, T. O. Mentes, M. Kiskinova, and E. Bauer, "Photoemission electron microscopy with chemical sensitivity: Speleem methods and applications," *Surf. Interface. Anal.*, vol. 38, p. 1554, 2006.

[170] L. Meng, R. Wu, L. Zhang, L. Li, S. Du, Y. Wang, and H. J. Gao, "Multi-oriented moiré superstructures of graphene on Ir(111): experimental observations and theoretical models," *J. Phys.: Condens. Matter.*, vol. 24, no. 31, p. 314214, 2012.

[171] E. Starodub, A. Bostwick, L. Moreschini, S. Nie, F. ElGabaly, K. F. McCarty, and E. Rotenberg, "In-plane orientation effects on the electronic structure, stability,

and Raman scattering of monolayer graphene on Ir(111)," *Phys. Rev. B.*, vol. 83, p. 125428, 2011.

[172] E. Loginova, S. Nie, K. Thürmer, N. C. Bartelt, and K. F. McCarty, "Defects of graphene on Ir(111): Rotational domains and ridges," *Phys. Rev. B.*, vol. 80, no. 8, p. 085430, 2009.

[173] A. Locatelli, C. Wang, C. Africh, N. Stojić, T. O. Mentes, G. Comelli, and N. Binggeli, "Temperature-Driven Reversible Rippling and Bonding of a Graphene Superlattice," *ACS Nano.*, vol. 7, no. 8, pp. 6955–6963, 2013.

[174] P. A. Thrower and R. M. Mayer, "Point defects and self-diffusion in graphite," *Phys. Stat. Solidi (a).*, vol. 47, p. 11, 1978.

[175] D. W. Boukhvalov and M. I. Katsnelson, "Destruction of graphene by metal adatoms," *Appl. Phys. Lett.*, vol. 95, p. 023109, 2009.

[176] A. V. Krasheninnikov, P. O. Lehtinen, A. S. Foster, and R. M. Nieminen, "Bending the rules: Contrasting vacancy energetics and migration in graphite and carbon nanotubes," *Chem. Phys. Lett.*, vol. 418, p. 132., 2006.

[177] E. A. Juarez-Arellano, B. Winkler, A. Friedrich, L. Bayarjargal, V. Milman, J. Yan, and S. M. Clark, "Stability field of the high-(P,T) Re_2C phase and properties of an analogous osmium carbide phase," *J. Alloy. Compd.*, vol. 481, p. 577, 2009.

[178] Z. Zhao, L. Cui, L. M. Wang, B. Xu, Z. Liu, D. Yu, J. He, X. F. Zhou, H. T. Wang, and Y. Tian, "Bulk Re_2C: Crystal Structure, Hardness, and Ultraincompressibility," *Cryst. Growth. Des.*, vol. 10, p. 5024, 2010.

[179] N. Miao, B. Sa, J. Zhou, Z. Sun, and R. Ahuja, "Mechanical properties and electronic structure of the incompressible rhenium carbides and nitrides: A first-principles study," *Solid State Commun.*, vol. 151, no. 23, pp. 1842–1845, 2011.

[180] N. R. Gall, S. N. Mikhailov, E. V. Rut'kov, and A. Y. Tontegode, "Carbon interaction with the rhenium surface," *Surf. Sci.*, vol. 191, p. 185, 1987.

[181] J. E. Hughes, "A survey of the rhenium-carbon system," *J. Less-Common Met.*, vol. 1, no. 5, pp. 377–381, 1959.

[182] S. Marchini, S. Günther, and J. Wintterlin, "Scanning tunneling microscopy of graphene on Ru(0001)," *Phys. Rev. B.*, vol. 76, no. 7, pp. 075429–9, 2007.

[183] G. C. Dong, D. W. van Baarle, M. J. Rost, and J. W. M. Frenken, "Graphene formation on metal surfaces investigated by in-situ scanning tunneling microscopy," *New. J. Phys.*, vol. 14, no. 5, p. 053033, 2012.

[184] B. E. Nieuwenhuys, D. I. Hagen, G. Rovida, and G. A. Somorjai, "LEED, AES and thermal desorption studies of chemisorbed Hydrogen and hydrocarbons C_2H_2, C_2H_4, C_6H_6, C_6H_{12} on the (111) and stepped 6(111)×(100) iridium crystal surfaces; comparison with platinum," *Surf. Sci.*, vol. 59, no. 1, 1976.

[185] P. W. Sutter, P. M. Albrecht, and E. A. Sutter, "Graphene growth on epitaxial ru thin films on sapphire," *Appl. Phys. Lett.*, vol. 97, no. 21, p. 213101, 2010.

[186] S. Günther, S. Dänhardt, M. Ehrensperger, P. Zeller, S. Schmitt, and J. Wintterlin, "High-Temperature Scanning Tunneling Microscopy Study of the Ordering Transition of an Amorphous Carbon Layer into Graphene on Ruthenium(0001)," *ACS Nano.*, vol. 7, no. 1, pp. 154–164, 2013.

[187] G. Kresse and J. Hafner, "*Ab initio* molecular dynamics for liquid metals," *Phys. Rev. B.*, vol. 47, pp. 558–561, 1993.

[188] G. Kresse and D. Joubert, "From ultrasoft pseudopotentials to the projector augmented-wave method," *Phys. Rev. B.*, vol. 59, pp. 1758–1775, 1999.

[189] J. P. Perdew, K. Burke, and M. Ernzerhof, "Generalized gradient approximation made simple," *Phys. Rev. Lett.*, vol. 77, pp. 3865–3868, 1996.

[190] S. Grimme, "Semiempirical GGA-type density functional constructed with a long-range dispersion correction," *J Comput Chem.*, vol. 27, pp. 31787–1799, 2006.

[191] E. Miniussi, and M. Pozzo, and A. Baraldi, and E. Vesselli, and R. R. Zhan, and G. Comelli, and T. O. Mentes, and M. A. Niño, and A. Locatelli, and S. Lizzit, and D. Alfès, "Thermal Stability of Corrugated Epitaxial Graphene Grown on Re(0001)," *Phys. Rev. Lett.*, vol. 106, no. 21, p. 216101, 2011.

[192] G. A. B. Y. S. Ponosov, "Evidences of superstructure in rhenium from raman spectra," *Phys. Status Solidi B.*, vol. 215, no. 1, pp. 137–141, 1999.

[193] A. Allard and L. Wirtz, "Graphene on metallic substrates: Suppression of the kohn anomalies in the phonon dispersion," *Nano Lett.*, vol. 10, no. 11, pp. 4335–4340, 2010.

[194] C. Tonnoir, A. Kimouche, J. Coraux, L. Magaud, B. Delsol, B. Gilles, and C. Chapelier, "Induced superconductivity in graphene grown on rhenium," *Phys. Rev. Lett. Accepted*, 2013.

DECLARATION

....

Grenoble FRANCE, 2013

Amina KIMOUCHE, April 22, 2014